Technische Universität Braunschweig

Institute of Aerospace Systems

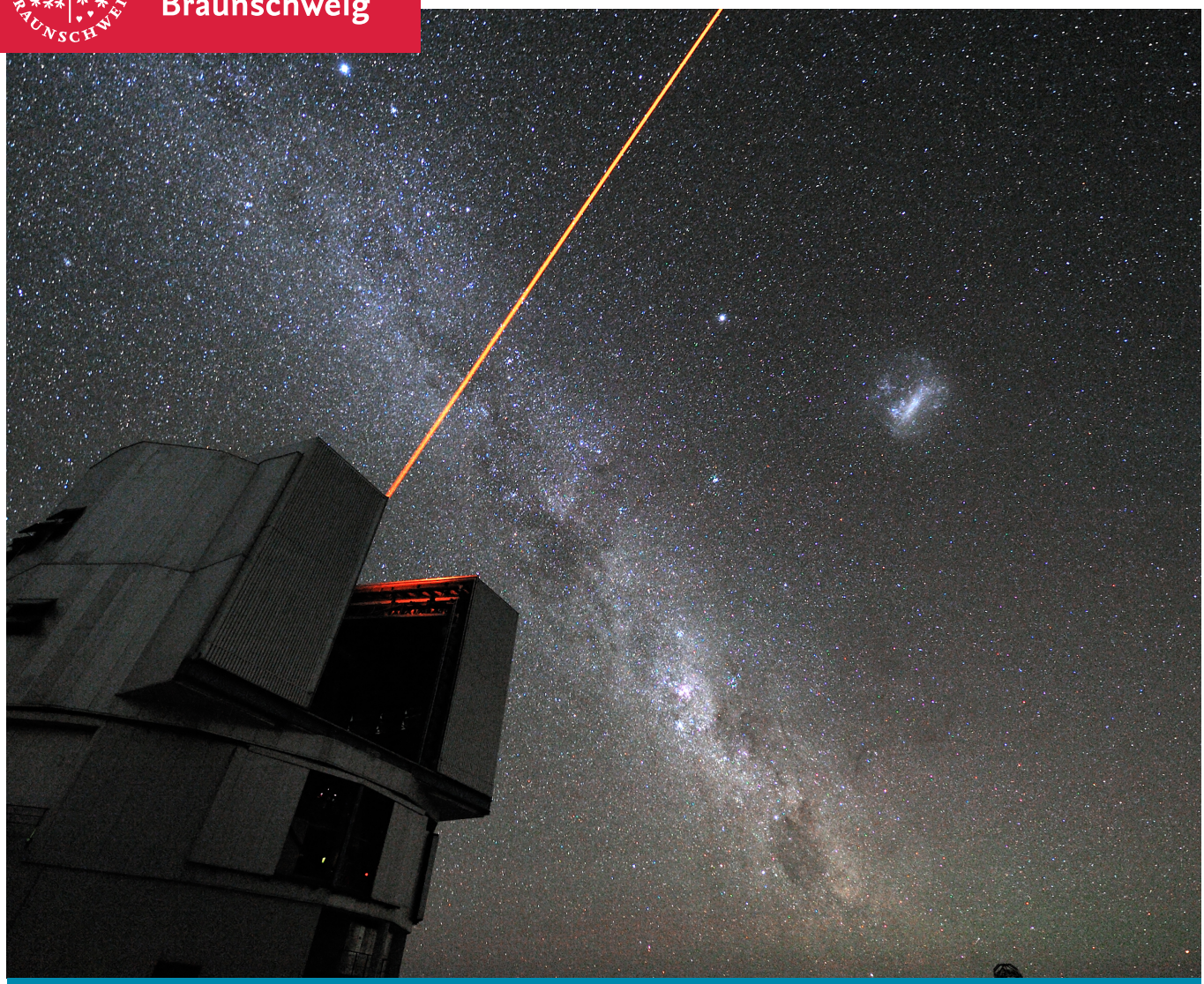

R 1429 M
Modelling of laser-based thrust generation for space debris removal

Institute of Aerospace Systems

Jascha Wilken

January 25, 2015

Credit for cover picture: G. Hüdepohl (atacamaphoto.com)

Aufgabenstellung

Die Originalaufgabenstellung ist bei Studienarbeiten dem ungebundenen Institutsexemplar beizufügen, bei Bachelor-, Master- und Diplomarbeiten dem gebundenen Exemplar zur Vorlage bei der Fakultät. Die Aufgabenstellung bei Bachelor-, Master- und Diplomarbeiten wird vom Fachbereich ausgegeben (bei CSE-Masterarbeit vom CSE Office), dieser registriert den Beginn und die Abgabe der Arbeit und stempelt diese Angaben auf das letzte Blatt der Original-Aufgabenstellung.

Eine Diplom-, Studien-, Bachelor- bzw. Masterarbeit soll zeigen, dass man in der Lage ist, in begrenzter Frist eine Aufgabe nach wissenschaftlichen Methoden selbständig zu bearbeiten.

Die Aufgabenstellung kann Literaturhinweise enthalten, die als Einstieg in die Aufgabe gedacht sind. Es wird erwartet, daß weitere Literatur selbständig gesammelt wird (Bibliotheken der TU, des Instituts, etc.).

Wichtig: Schriftverkehr mit Dritten bei Nennung des die Arbeit betreuenden Instituts bedarf der vorherigen Genehmigung.

In der Abgabeversion dann dieses Blatt entfernen und an dieser Stelle durch die Aufgabenstellung ersetzen!

Eidesstattliche Erklärung

Ich erkläre hiermit an Eides Statt, dass ich die nachfolgende Arbeit selbständig und nur unter Zuhilfenahme der angegebenen Literatur angefertigt habe.

_____

Datum, Unterschrift

Abstract

A possible method for the active removal of space debris is the irradiation of the debris with a pulsed laser system. With sufficient power the surface layer of the debris object is ablated and yields thrust, which will ideally lower the perigee of the debris object. The direction of the thrust is independent of the direction from which the debris object is irradiated, it is normal to the local surface.

This thesis investigates the effects caused by complex shapes and varying orientation of a debris object on the thrust vector. The tool EXPEDIT was written in C++ in order to calculate the impulse transferred by laser ablation, taking into account variation of the fluence, self-shadowing and complex geometries.

Parameter studies were undertaken in order to investigate the behavior of the laser-debris system. The figure of merit ζ was introduced as the ratio of radial to axial impulse components with respect to the laser beam propagation vector. In order to describe the axial component η_j was introduced, a variation of the η_c from [34]. η_j is the ratio of the actually achieved axial impulse to the maximum possible axial impulse. EXPEDIT was used to gain estimates for ζ and η_j for three exemplary cases for different fluences in order to include a varying coupling coefficient. It should be noted that these simulations yielded values for ζ and η_j that were more problematic than expected. For a plate-shaped debris object η_j ranged from 0.1 to 0.3 and ζ from 0.4 to values slightly above 1. Some possible methods to improve the efficiency of the laser-based de-orbit are proposed.

Contents

Contents **6**

1. Introduction **9**
1.1. Space Debris . . . 9
1.2. Debris removal strategies . . . 10
1.3. Thesis scope and concept . . . 11

2. Potential space debris targets **12**
2.1. Detection and tracking of space debris . . . 12
2.2. Boundary conditions . . . 12
2.2.1. Material . . . 12
2.2.2. Shape . . . 14
2.2.3. Orbit . . . 16
2.2.4. Initial rotation . . . 17
2.3. Summary . . . 17

3. Momentum generation by laser ablation **18**
3.1. Light Amplification by Stimulated Emission of Radiation (LASER) . . . 18
3.2. Laser ablation . . . 19
3.3. Laser ablation as a space technology . . . 19
3.4. Dependencies of the coupling coefficient . . . 20
3.4.1. Simulation of the coupling coefficient . . . 20
3.4.2. Material . . . 21
3.4.3. Polarization . . . 21
3.4.4. Temporal pulse length . . . 22
3.4.5. Wavelength . . . 22
3.4.6. Fluence . . . 22
3.4.7. Incidence angle . . . 23
3.5. The area matrix approach . . . 24
3.5.1. Assumptions and limitations . . . 25
3.5.2. Inverse numerics . . . 25

4. Numerical Modeling: EXPEDIT **27**
4.1. Coordinate systems and geometric parameters . . . 28
4.2. Input . . . 28
4.2.1. Control parameters . . . 28
4.2.2. Input parameters . . . 29

4.2.3. Solid body parameters . . . 29
4.2.4. Laser parameters . . . 29
4.2.5. Laser-matter interaction parameters . . . 30
4.2.6. Debris parameters . . . 30
4.2.7. Modes parameters . . . 30
4.2.8. Simple shapes . . . 30
4.2.9. Complex shapes . . . 31
4.2.10. Solid Bodies . . . 32
4.2.11. Inertia tensor . . . 32
4.2.12. Other information . . . 32
4.3. main() . . . 32
4.4. MainCore() . . . 33
4.4.1. Hit . . . 33
4.4.2. CheckForHits() . . . 35
4.4.3. CalculateLocalCouplingCoefficient() . . . 40
4.4.4. CalculateLocalImpulse() . . . 41
4.4.5. CalculateAngularMomentum() . . . 41
4.4.6. Kinetics . . . 42
4.4.7. Comparison . . . 44
4.5. Output . . . 44
4.5.1. Output of mode-calculations . . . 45
4.6. Verifcation and Validation . . . 45
4.6.1. Validation . . . 45
4.6.2. Verification . . . 46

5. Parameter studies **49**
5.1. Coupling coefficient . . . 49
5.2. Figures of merit . . . 50
5.2.1. Orbital effects . . . 51
5.3. Axial vs. radial impulse . . . 51
5.3.1. Circular orbit . . . 53
5.3.2. Elliptical orbit . . . 54
5.4. Shape considerations . . . 54
5.5. The modes . . . 55
5.5.1. Default Parameters . . . 55
5.5.2. Mode 1 . . . 55
5.5.3. Mode 2 . . . 59
5.5.4. Mode 3 . . . 59
5.5.5. Mode 4 . . . 60
5.5.6. Mode 5 . . . 60
5.5.7. Mode 6 | Random . . . 61
5.5.8. Mode 7 . . . 67
5.6. Conclusion . . . 67

6. Summary **69**

7. Future prospects **72**
7.1. Use of DebriSat data . . . 72
7.2. Experimental verification . . . 72
7.3. Optimization . . . 72

Bibliography **74**

List of Figures **77**

List of Tables **79**

Nomenclature **80**

A. German summary **83**

B. xml-files **86**
B.1. Control file . . . 86
B.2. Geometry file . . . 89

C. The verification cases **95**
C.1. The plate . . . 95
C.1.1. Plate1 . . . 95
C.1.2. Plate2 . . . 95
C.1.3. Plate3 . . . 95
C.2. Sphere . . . 95
C.2.1. Sphere mesh . . . 95
C.3. Wedge . . . 95
C.3.1. Wedge1 . . . 95
C.3.2. Wedge2 . . . 95
C.3.3. Wedge Oscillation . . . 96
C.3.4. Wedge mesh . . . 96
C.4. Cone . . . 96

D. Derivation of oscillation frequency for irradiated wedge **97**

E. Projektmanagement **99**
E.1. Work Package Description . . . 99
E.2. Work breakdown structure . . . 110
E.3. Gantt-Diagramm . . . 111

1 Introduction

1.1. Space Debris

As with every other location humanity has used and inhabited we have left our mark on space as well. Since SPUTNIK 1 was shot into an orbit around the earth in 1957, over 7000 payloads have been delivered to space. This number is based on the online Satellite Catalog [45] that contains all public objects tracked by the Space Surveillance Network (SSN) of the United States. The SSN mainly uses radars to detect and track objects in orbit, if they are large enough. Unfortunately, the catalog contains many objects that are not active payloads anymore. Of the 3966 payloads on orbit on the 16^{th} of September 2014 only 1345 remain active. The rest are inactive and are considered debris. In addition to old payloads the catalog contains 13161 objects categorized simply as debris. The SSN can only track objects down to about 10 cm diameter, so that these numbers do not contain any small debris object. Figure 1.1 shows the historical evolution of the number of catalogued objects.

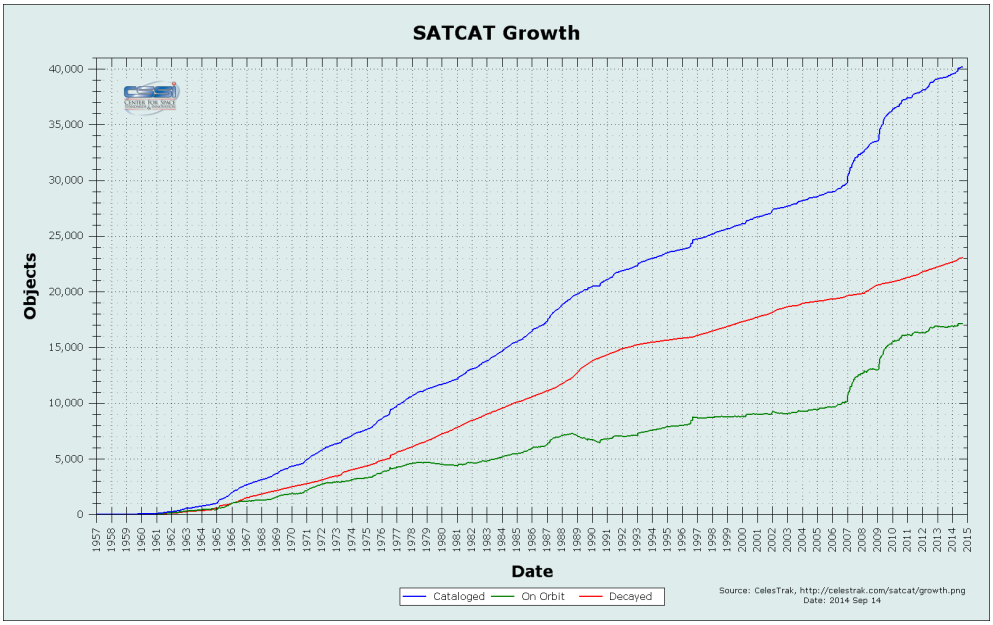

Figure 1.1.: Historical growth of catalogued objects, from [45]

The sources of the space debris are manifold. While many mission related objects (e.g. launch adapters or lens covers) and old inactive satellites play their role in the space debris population, the largest source are on orbit break-up events. Explosions of satellites and rocket stages are a major contributor. Some of these were caused intentionally while other were caused by the propulsion systems, where excess energy was not vented at the end of life [22].

A growing contributor to the debris population are on-orbit collisions. The most severe collision between two orbiting objects took place on the 10^{th} of February 2009. The satellites Iridium 33

and Cosmos 2251 collided above northern Russia [45]. The SSN has tracked 2200 objects associated with this collision. If a collision occurs as between Iridium 33 and Cosmos 2251 the fragments significantly increase the spatial debris density in the affected orbital region. The increase of debris population leads to higher collision risks in the future. More collisions lead to more debris and so forth. If the population growth through collisions is larger than the amount of debris falling into earth's atmosphere this leads to the Kessler-syndrome as described in [20]. This vicious cycle would make the affected orbits inhospitable to manned and unmanned missions.

While collisions with known objects can be avoided using the orbital data provided, debris with a diameter smaller than 10 cm is functionally invisible. Due to the high relative speeds possible in a collision (up to 15 km/s) even small debris fragments are a danger to humans and spacecraft in orbit. Whipple-Shields [22] can protect spacecraft from objects with a diameter up to 1 cm. Objects between 1 cm and 10 cm thus pose a significant threat to spacecraft, since they cannot be dodged and cannot be blocked by shields. Since the number of objects in that size regime is an order of magnitude larger than the amount of debris larger than 10 cm this poses a serious threat [22].

In order to reduce the number of debris objects on orbit, guidelines have been released by various space agencies [22]. They demand the passivation of spacecraft at the end of their mission, and satellites are supposed to be brought into a lower orbit at the end of their mission, so that they have a remaining orbital lifetime of less than 25 years.

But recently, especially after the collision of Iridium 33 and Cosmos 2251 in 2009 and the Anti-Satellite-Missile test conducted by the People's Republic of China in 2007 [19], see figure 1.1, there is doubt that passive measures are enough to avoid the Kessler syndrome. [21] shows that in order to prevent further growth of the debris population, passive measures will not be sufficient: the active removal of space debris will be necessary.

1.2. Debris removal strategies

Many concepts for the removal of space debris have been and still are being investigated. The ideas range from micro-satellites that capture large debris objects and extend an electrodynamic tether [31] to releasing an artificial dust ring around the earth in order to create artificial drag on debris fragments [7] and many more.

Another concept being evaluated for the removal of space debris is based on using laser irradiation to create thrust. There are many versions of this idea, but this thesis focuses on the version investigated during the CLEANSPACE studies [16].

The CLEANSPACE program was funded by the European Union and ran from 2011-2014. A consortium of international partners, including the DLR and ASTRIUM Space Transportation (today Airbus Defence and Space) investigated the possibility to detect, track and eventually remove medium sized debris (1 cm to 10 cm) with a ground-based laser system. The theory of debris removal by laser ablation will be discussed in depth in chapter 3, but basically the effects are caused by heating a thin surface layer to extreme temperatures, which causes particles of the target to move away from the target with extremely high velocities, causing thrust using the same principle as chemical rocket engines: conservation of linear momentum. If directed correctly this thrust causes the orbit to decrease or, if enough thrust is applied, it can cause the debris object to directly reenter the atmosphere.

The direction of the exhaust plume, and thus of the thrust, is independent of the incidence angle

of the laser beam and follows the local normal of the irradiated surface. For specific cases such as a spatially homogeneous irradiation of a cube, a sphere or a correctly aligned plate, this means the thrust vector generated by ablation shares the direction with the incoming laser beam. That is very convenient, when calculating the effects of the maneuver.

The concept has received some attention apart from the European CLEANSPACE project. The ORION program [4] investigated a similar concept and many researchers and institutions are investigating the concept at the moment. Another common version consists of deploying a satellite armed with a laser system and engaging targets from orbit to orbit [34, 46].

To the knowledge of the author, all concept studies and similar investigations share one common assumption: They neglect the effects caused by geometrically complex and randomly oriented targets, merely in [25] and [26] the geometric effects are investigated and the Area-Matrix concept is proposed, which is discussed in detail in section 3.5. Other works [36] introduce an efficiency factor $\eta \approx 0.3$ in order to approximate the thrust lost due to geometrical effects.

But even these concepts are analytical in nature and cannot take into account the multitude of effects that influence the impulse coupling coefficient c_m, which describes the efficiency of the ablation process and the impulse generated.

1.3. Thesis scope and concept

The main goal of this thesis is the creation of a simulation that allows the investigation of the thrust generation through laser ablation on a geometrically complex target and that allows a multitude of variable parameters during the investigation. This tool will then be used to conduct parameter studies in order to characterize the thrust vector and the involved uncertainties.

The theoretical foundations for this goal are laid in chapters 2 and 3 which respectively give information on possible space debris targets and laser ablation. Chapter 4 describes the numerical models used and the structure of the code developed for this purpose. That code is used to investigate the impact of multiple parameters and the results of these parameter studies are presented and discussed in chapter 5. Finally, after the summary in chapter 6, chapter 7 presents prospects and possibilities for future research.

2 Potential space debris targets

As already discussed in the introduction, the critical space debris objects with regard to the risk they pose to spacecraft, are the objects too large to be caught by shields but too small to be catalogued. With improvement in detection this margin is shrinking but remains a great risk. Depending on the coming developments the number of debris objects in the 1 to 10 cm size regime could grow dramatically and number millions of objects [22].

2.1. Detection and tracking of space debris

While this topic does not directly affect this thesis it does offer some insight into the information that will be discussed in the following sections. Additionally it offers synergy with some prospects that will be discussed in chapter 7.3.

Without going into detail it should suffice to say, that all detection methods used in this point of time use reflections caused by the space debris. Radar-based methods use the reflection of the radio waves sent out by the radar stations themselves. Optical detection depends on the reflection of sunlight from the debris target in question. Information regarding these two methods and the network of stations used to track space debris can be found in [22]. A variant of the optical detection is the combination with laser ranging, which uses a pulsed laser to measure the propagation time of the reflected light and thus can deliver range measurements which can be used to determine the orbits very accurately [50].

2.2. Boundary conditions

In order to accurately model debris objects the first step is to review the information available for individual debris objects. This includes data available at the moment as well as possibilities in the future.

The following sections primarily investigate the properties of LEO debris in the abovementioned size regime, which is the focus of the laser-based deorbit concept.

2.2.1. Material

Two questions have to be answered at this point: Which material types can be found on orbit and is it possible to detect from which material specific debris objects are made?

The first question can be answered by a variation of the familiar saying: “What goes up, must go down”: “What is up, must have gone up”. Apart from the natural meteoroid environment, every single piece of space debris has been brought into orbit by some space mission. Theoretically it would be possible to sum up the materials used in every mission, subtract the debris already deorbited and have an exact picture of the material composition. However, most mission related objects are highly individual so it is very difficult to get a generally valid estimation of the materials used. However, the main contributor to on orbit fragmentations are not the payloads as such, but the upper rocket stages used to transport the payloads into their final orbit [22]. These upper stages often share the

same design and different systems do not vary as extremely as payloads do. Generally, aluminum and steel are the main materials used for upper stages [33]. It is notable that, historically, steel dominated the upper stages, for example in the Delta 2, but for later upper stages, for example in the Delta 4 upper stage, aluminum has become the material most used. With the rise of composites it is to be expected that their share of orbital debris will increase and subsequently decrease the aluminum and steel share.

The analysis of payloads and upper stages in [33] yields four major material groups: steel, aluminum, plastics and composites.

Another source of information with regard to the materials generally found in space debris are exposed surfaces retrieved from space. This category contains experiments retrieved by the space shuttles, other objects retrieved by the shuttles, such as solar panels from the Hubble Space Telescope, and finally the windows from the Space Shuttles themselves. The particles retrieved from the space shuttle themselves consist mostly of paint, aluminum and a surprisingly high number of steel particles [33]. The relatively high amount of steel particles can be explained by the quasi-historical nature of the shuttle flights recorded in the study from 1992 until 2002. So the sampled debris population has since partially deorbited and been replaced by newer materials.

Unfortunately, with the end of the space shuttle era it has become impossible to retrieve large surfaces from space and thus no newer data is available.

An important experiment retrieved by the space shuttles was the Long Duration Exposure Facility, hereafter referred to as LDEF, which was a 10 ton satellite left in orbit for 2076 days, then retrieved and brought back to earth. This experiment took place from 1984 to 1990, so the data shares the same historical nature as the particles retrieved from the space shuttle windows. The objects that impacted on the LDEF were mostly aluminum, but stainless steel and paint flakes were also found [18].

While ground-based impact tests do not reveal new data regarding the materials in orbit, since the fragments are made of the same material the original target was made of, they do imply some interesting data regarding size distributions. The data from the SOCIT 4 impact test [24] reveals that most of the small fragments in the cm to mm regime consist of the medium-density materials [33]: aluminum, titanium and paint. The majority of the steel fragments were larger than the specified size scope and most polymer fragments were smaller.

The second question concerning the material of the specific debris object is trickier. Identification of the material of a specific debris object using the orbital data is nearly impossible. While the rate by which the orbit degrades can be used to estimate the area-to-mass ratio of the debris, this ratio is also influenced by the shape and orientation of the object and thus the ratio cannot be used to calculate a density.

However, another tool can identify the material of the target: spectroscopy. The same method used by astronomers to gain information about distant stars, planets and other deep space objects can be used to identify materials of debris objects [32]. This information is important, as chapter 3 will show that the laser ablation process is dependent on the material, which will be discussed in section 3.4.2.

The general information discussed above has shown that aluminum, steel, composites and to some degree polymers are the materials that have to be considered with regard to laser ablation modeling.

2.2.2. Shape

This section is vital for the thesis since knowledge of the shapes that are to be investigated is of course necessary, before these shapes can actually be investigated. The only measure actually available at this moment is the area to mass ratio used to categorize space debris objects. This ratio is especially important when calculating the effects of area-based forces, for example air drag or thrust caused by laser ablation.

There are methods to discern some information about the shape of a specific debris object. Radar systems can use the variation of the cross section [2, 41] or the Doppler shifts caused by the spinning of irregularly shaped debris [40] to estimate the shape of the space debris object. Similar possibilities also exist for optical methods using the variation in reflected light [52]. This point will beof interest during the discussion in chapter 7. But the sheer amount of small debris objects prevents the creation of a database with all debris shapes. So this information can only be used to determine shape estimates for specific objects.

However, the main source of information with regard to the general shape of debris fragments are ground based impact tests, such as the aforementioned SOCIT 4 tests. Since the majority of small debris objects originated from various fragmentation events [22], these demand special attention. The SOCIT 4 test was remarkable because the target was a flight-ready U.S. Transit navigation satellite. Up to the DebriSat tests conducted in 2014 [28], this was the only test that used an actual full-sized satellite.

In [24] the authors categorize the fragments from the SOCIT 4 test into various categories. For the sizes from 1 to 10 cm the following shapes, as defined in [24], are the most numerous:

Other: Irregularly shaped.

Flake: Thin and somewhat concave.

Plate: Flat and curved plates.

Another set of data comes from the more recent high velocity impact (HVI) tests conducted on micro satellites in 2005 and 2007 [17]. The satellites had a high percentage of CFRP (carbon fiber reinforced plastic) and GFRP (glass fiber reinforced plastic) materials and thus represent the fragmentation behavior of satellites with modern materials.

In order to understand the following, a short digression is made here to present NASA's orthogonal 'projection dimension' system: The characteristic length of an object is the average of the three lengths x, y and z. x is defined as the maximum extension within the debris object, y the maximum extension perpendicular to the vector of x, and the same applies to z in regard to the first two dimensions [24]. The dimensions are shown in figure 2.1.

In 2005 and 2007, the Kyushu University and the NASA Orbital Debris Program Office collaborated in performing a series of impact tests on multiple micro-satellites (20 cm by 20 cm by 20 cm). Carbon-fiber-reinforced polymers and aluminum where the main materials used in the construction of the satellites and thus most fragments are from those materials [17].

The fragments created by the three tests in 2007 are shown in figure 2.2. The fragment properties were documented using the 'projection Dimension' discussed above and can be seen in figure 2.3. The ratio of x to y is designated as aspect ratio and y to z is designated as thinness. In regard to

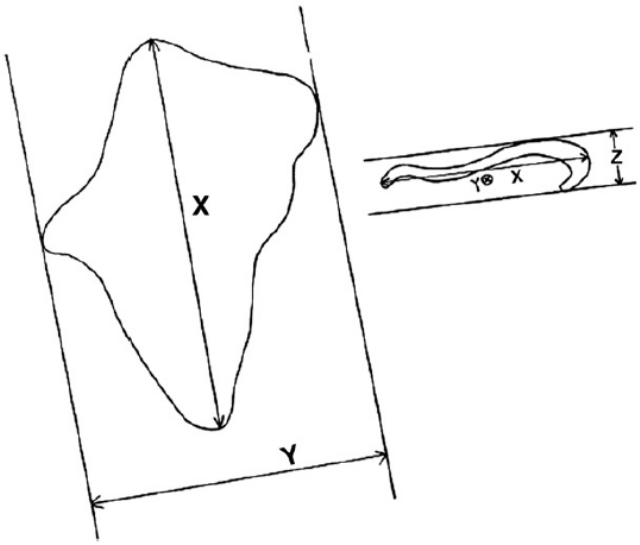

Figure 2.1.: Sketch of NASA orthogonal 'projection dimensions', from [24].

Figure 2.2.: Overview of fragments of HVI tests from [17]. The original satellite was a cube with an edge length of 20 cm, part of which can be seen in the top left corner of the middle picture.

the aspect ratio two groups can be identified: fragments with a high aspect ratio resemble needles, while fragments with a low aspect ratio are similar to plates. The fragments can have a variety of thinness values ranging from box-shaped fragments to thin-shaped fragments, or simply plates.

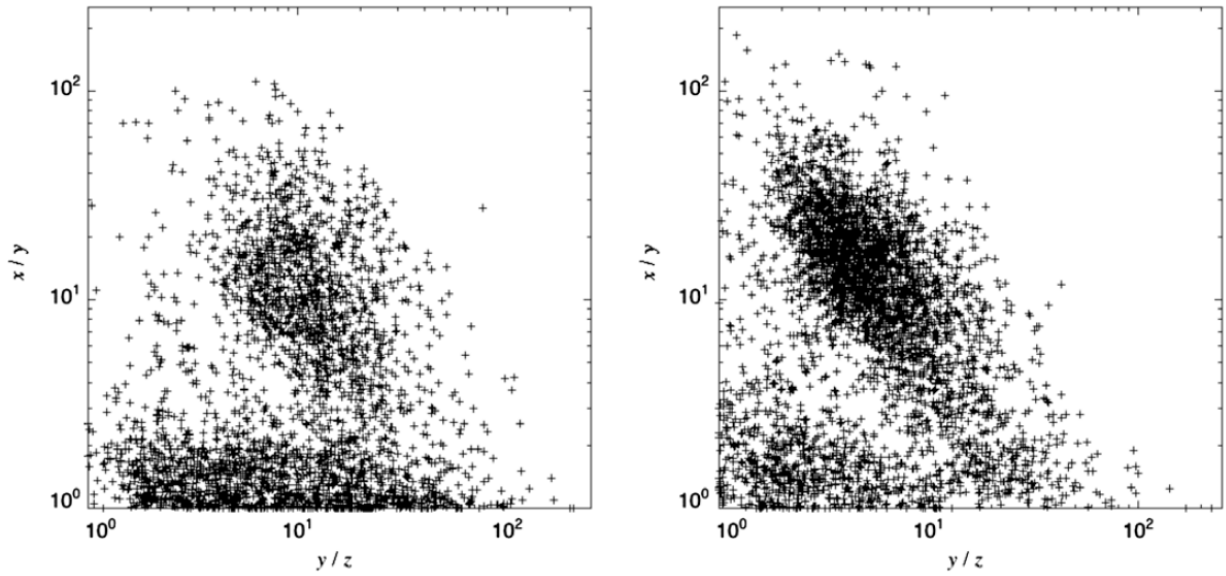

Figure 2.3.: Aspect ratio versus thinness distributions from two different HVI tests [17]. The aspect ratio is the x and y dimension of a fragment as defined in figure 2.1. Thinness is the ratio of y to z.

Finally, there is one type of debris of which the shape is known exactly: The NaK (sodium-potassium alloy) droplets expelled from the cooling system of the nuclear reactor powering the soviet RORSAT satellites are spherical [51].

DebriSat

The DebriSat impact tests offer the exciting opportunity to gain detailed information regarding fragmentation events. A representative 50 kg satellite was built for the express purpose of being destroyed during a HVI test in the first half of 2014. Modern materials were used in order to gain information about their fragmentation behavior. The goal is to individually analyze fragments down to a size of 2 mm. Additionally, 'representative' fragments shall be selected for 3D scanning and further investigations [28]. Especially the 3D data could offer interesting possibilities, which will be discussed in chapter 7. While the experiment was successful, the complete analysis of the data is a project that can take years and thus it will be some time before this data becomes available [27].

2.2.3. Orbit

The distribution of space debris is an object of much research activity and even though only large objects are tracked by the SSN, the models ORDEM 3.0 [23] and Master-2009 [11] contain information regarding the debris flux for any orbit. This thesis focuses on the same orbits the CLEANSPACE program was focused on: LEO orbits, specifically the heights usually associated with polar orbits, since those are among the most polluted areas [22]. However, the code of this thesis is written in order to produce valid results regardless of orbital configuration. Specifically, the main output value will be the transferred impulse, which can then be applied to specific orbital configurations.

2.2.4. Initial rotation

Taking into consideration the origin of most debris objects, fragmentation events, it is not surprising that many of them are spinning [2, 41]. While interaction with the earth's magnetic field can dampen the spin of debris, assuming it consists of an appropriate material [39], it has to be assumed that most objects will be rotating The spin of an individual object can be detected with the same method used to determine its shape, by analyzing the amplitude of the reflected light and seeking patterns. The possible uses for this information will be discussed in chapter 7.

2.3. Summary

In conclusion, it is possible to gather some information on the composition of a specific debris object and to estimate the parameter range of available shapes. However, this range is so extensive that the tool programmed in this thesis cannot focus on one type of shape, but has to be able to conduct the desired calculation for any type of shape. Additionally, while conducting parameter studies, it has to be taken into account that while some generalizations can be made, the range of possible shapes and materials is large and has to be considered.

3 Momentum generation by laser ablation

This chapter first presents an overview of laser systems and focuses on certain variants while neglecting a complete description and any details. For a complete overview over the function of laser systems, refer to [15], which is used as the main reference of the following sections.

3.1. Light Amplification by Stimulated Emission of Radiation (LASER)

The principle behind laser systems has been known since 1958 [43] and is based on a mechanism called "stimulated emission" that allows the amplification of light. The base principle of stimulated emission was, in theory, discovered by A. Einstein in 1917 [10]. Generally, each laser system consists of three components: The gain medium, the pump and the resonator [15]. The heart of the laser is the gain medium which is used to transform the energy delivered by the pump into a high energy light beam.

Optical elements, the 'resonator', ensure that the laser beam crosses the gain medium multiple times, amplifying the laser beam each time. This is achieved by manipulating the energy states within the gain medium. The gain medium can be seen as a group of systems that can only inhabit certain quantum mechanical states with differing energy levels. These states can consist of different rotational states of the molecules, as in CO_2 lasers, or of varying electronic excitation states.

The energy difference between these quantum states corresponds to photons of a specific wavelength. If such a photon encounters the system in the ground state, it can be absorbed and the system enters the excited energy level. Without external influence the excited system would randomly decay to the ground state and emit a photon of the corresponding wavelength.

However, if a photon with the same wavelength encounters an excited system, this photon can cause the system to decay to the ground level and emit the corresponding photon. This second photon has exactly the same direction, wavelength and phase as the original photon, which has now effectively been doubled.

Einstein showed in [10] that the probability of the photon being absorbed by a ground level system and the probability of it causing stimulated emission from an excited system are equal. Thus, if the laser medium contains more systems or molecules with higher energy levels, incoming photons of the correct wavelength will be amplified.

Within a laser system, the pump delivers the energy to raise as many atoms as possible into the excited states in order to keep the amplification process going. Since the additionally emitted photons share the direction phase and polarization of the original photons, they form a coherent group of photons: the laser beam.

Pulsed Lasers

In order to achieve laser ablation, which will be discussed in the following section 3.2, high laser fluences have to be applied. If a continuous laser beam would be used, the power demands would be excessive and a powerful pump would have to be used, which creates additional heat issues within the laser system. Simply lowering the fluence would be unacceptable to the procedure, since any fluence underneath the ablation threshold would only result in heating or melting and thus be wasted. For metals, the threshold fluence is typically 1-10$\frac{J}{cm^2}$ [3].

Pulsed lasers offer a way around this problem. There are multiple methods for creating a pulsed laser, one of them is "Q-Switching": certain mechanisms influence the resonator so that most photons are not reflected. Meanwhile the energy provided by the pump is used to bring a large number of atoms into higher energy levels. Without the influence of the reflected photons, they stay in the high energy state for some time. Once the medium is fully charged, the resonator is activated and the incoming photons find a large number of atoms in the higher energy level and start an intense chain reaction that leads to most the stored energy being released in one concentrated pulse. Another way of achieving a pulsed laser is the pulsed operation of the pump.

This technology allows mediocre pumps to power laser systems with high energy pulses and thus achieve ablation. All laser systems that are being considered for laser based debris removal are pulsed systems and thus the repetition rate ν and the pulse energy are two of the most important parameters of the laser system.

3.2. Laser ablation

Laser ablation is the process of removing material with the help of a laser. Typically a pulsed laser is used, they offer the advantage that since they dump their energy during short pulses, they can achieve ablation with relatively low average power.

During a pulse the laser beam delivers a large amount of energy to the surface layer of the target, much more energy than can be quickly distributed to the deeper layers by thermal conduction. This leads to extremely high temperatures in the surface layer (up to 10,000 K [30]) and consequently to the vaporization of the target surface. At higher fluences the ablated material is typically ionized and thus forms a plasma plume. The large pressures induced by the large temperature cause the ablated material to be accelerated away from the target. At this point it should be noted that the plume of ablated material is parallel to the surface normal, independent from the incidence angle of the laser beam.

For propulsion purposes the effectiveness of the ablation process is measured by the coupling coefficient c_m as defined in equation 3.2 [35]. The dependencies of the coupling coefficient are complex and will be discussed in detail in section 3.4.

3.3. Laser ablation as a space technology

The velocity of the ablated particles can be calculated with equation 3.1, from [35]:

$$v_E = \sqrt{\frac{2kT_i}{m_i}}, \tag{3.1}$$

Since temperatures up to 10,000 K can be caused by the laser irradiance, this leads to high escape

velocities and a high specific impulse. The velocity of the escaping plasma can reach 20 to 200 $\frac{km}{s}$ [16].

The thrust generation is very similar to the well-known principle all known spacecraft engines use: conservation of momentum. Some type of mass is accelerated in the opposite direction from the intended thrust vector. The acceleration can be provided by energy from a chemical reaction within the fuel or by electrical heating with power provided by solar cells or other electrical power sources such as a thermonuclear reactor or, as in this case, by a laser beam. While the laser can originate from the spacecraft itself, the laser offers the unique opportunity to transfer energy from a remote station to the object that shall be accelerated. A ground based station could beam the energy to cooperative targets (for station keeping or launching) or to uncooperative targets (debris removal). Thanks to the high exhaust velocities this propulsion method offers high specific impulses.

Various concepts have been evaluated for application of laser propulsion. Ranging from launching small spacecraft to LEO [42], as a propulsion option for satellites [9] and as a debris removal tool. For the debris removal using laser ablation two options exist: Ground based systems [13, 37] or systems based on a satellite [34, 46].

While in many aspects this thesis uses the groundwork laid by the CLEANSPACE project, the tool was written so that the results are applicable to ground and space based systems.

3.4. Dependencies of the coupling coefficient

The coupling coefficient c_m is formally defined as the ratio of the linear momentum change, Δp to the pulse energy E_p:

$$c_m = \frac{\text{impulse}}{\text{pulse energy}} = \frac{\Delta p}{E_p} = \frac{m_{jet} \cdot v_{jet}}{E_p} = \frac{\left(m_{deb} - m_{jet}\right) \cdot \Delta v_{deb}}{E_p} \approx \frac{m_{deb} \cdot \Delta v_{deb}}{E_p}. \tag{3.2}$$

As the central figure of merit for the whole laser ablation process the determination of the coupling coefficient is vital in order to accurately calculate the impulse created by laser irradiation. The coupling coefficient is dependent on many parameters:

- material
- incidence angle
- polarization
- pulse length
- wavelength
- fluence

In the following, each parameter and its effect on the laser-matter interaction will be discussed in a separate section.

3.4.1. Simulation of the coupling coefficient

In order to estimate the coupling coefficient without undertaking time-consuming experiments, the Virtual Laser Lab (VLL) online tool was used. It uses a hydrodynamic simulation code in order to calculate the effect of laser irradiation on a metallic target. This tool only allows one-dimensional

cases. The VLL includes the Two-Temperature-Model [1], employing different temperatures for atomic lattice and electron cloud. According to this model the laser pulse energy is stored in the electron cloud and is transferred with a material-specific delay to the atomic lattice. For further information on this tool refer to [38].

3.4.2. Material

The material has a significant effect on the ablation and thus the coupling coefficient. Figure 3.1 shows experimental data from [16] for different materials that can be found in debris objects. Figure 3.2 shows the simulation results for the coupling coefficient attained for gold and aluminum. While the exact values for each material are not of further importance for this thesis, it is clearly visible that the target material has an influence on the coupling coefficient. Especially in the simulated example the difference in ablation threshold and optimum fluence is obvious. With the use of the aforementioned spectroscopy, it would be possible to detect the material type of the target and change the fluence accordingly.

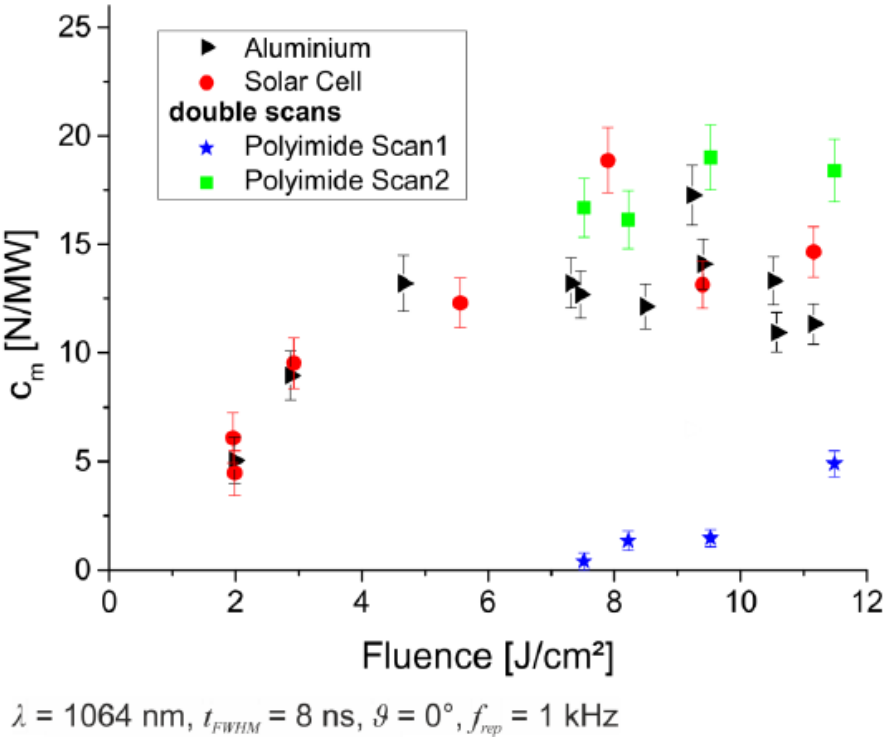

Figure 3.1.: Experimental results for coupling coefficient from [16] for aluminium, solar cells and a polyimide. The first scan of the polyimide was used to clean the surface of the target.

3.4.3. Polarization

The influence of polarization is also depicted in Figure 3.4 in section 3.4.7. Since polarization is closely coupled to the reflectivity and the angle of incidence, their effects will be discussed jointly in section 3.4.7.

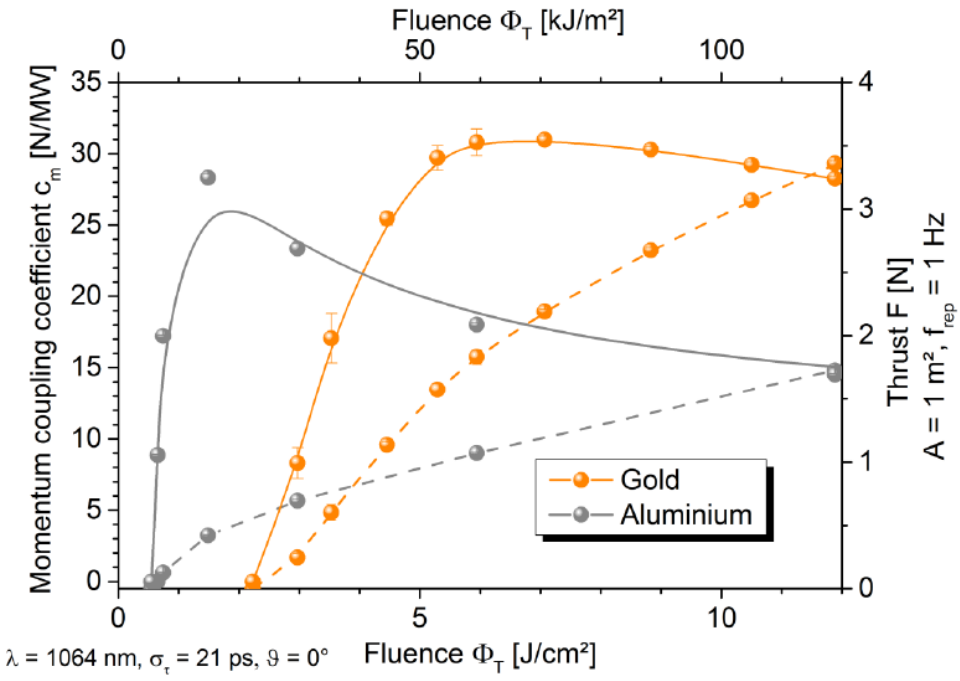

Figure 3.2.: Simulation results for the coupling coefficient and total thrust for gold and aluminium vs. fluence Φ_T [16]

3.4.4. Temporal pulse length

The physics behind the laser ablation process differs significantly between pulses in the nanosecond regime or much shorter pulses in the picosecond or femtosecond regime [3]. Special models are needed to simulate the phase transitions of the target surface for short pulses [35]. However, since the pulses considered for the CLEANSPACE project are all in the ns regime [16], this does not have any ignificant influence on the calculations. The method for implementing different pulse lengths will be discussed in section 4.4.3.

3.4.5. Wavelength

For targets of aluminum the wavelength has a negligible influence, while polymer targets have large fluctuations in regard to the wavelength. This is caused by specific absorption bands that allow a large energy intake at certain wavelengths; the exact wavelength differs depending on the type of polymer. Since it is difficult to detect the exact type of polymer from the ground and the fact that the possible wavelength is restricted due to the atmospheric absorption, variation of the wavelength seems problematic [16].

3.4.6. Fluence

The coupling coefficient is strongly dependent from the incident fluence of the laser beam. Figure 3.3 shows a typical course for coupling coefficient values of aluminum for different fluences. [35] includes a review of the dependency of the coupling coefficient to the fluence for different materials.

If the pulse energy is too low, no ablation takes place and the energy is spent heating and melting the debris object. Only if the threshold fluence is exceeded parts of the debris object are vaporized

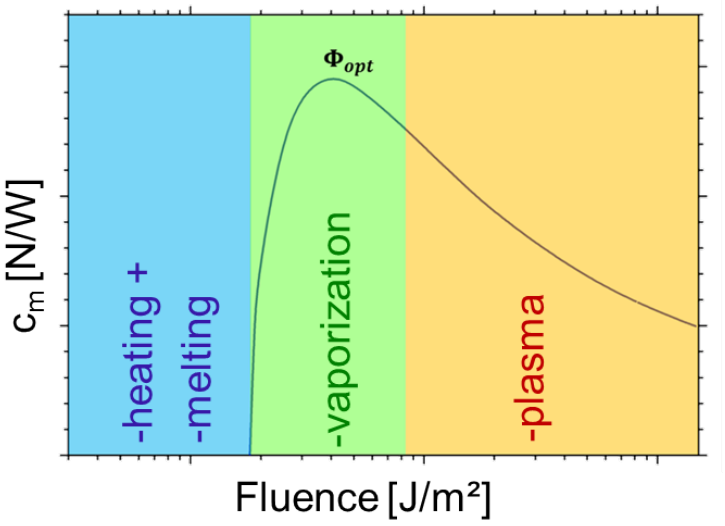

Figure 3.3.: Typical behavior of the coupling coefficient vs. fluence for aluminium [1]

and create impulse. At very high fluences, a plasma layer forms in front of the target, which reflects and absorbs part of the laser energy. This causes lower coupling coefficients. However, as can be seen in figure 3.2, the total impulse does steadily increase with higher fluences, even if c_m and thus the efficiency do not [35]. Since the optimum fluence Φ_{opt} is heavily dependent on the pulse length and target material, the exact values are not as important as the general consideration: Though the first idea would be the use a irradiation as close to Φ_{opt} as possible, this is not guaranteed to be optimal configuration.

3.4.7. Incidence angle

The first effect from an increased incidence angle stems from the geometrical effect that lowers the fluence that actually arrives at the surface, thus affecting the coupling coefficient as described in the previous section. But even if that is taken into account, there appears to be a secondary effect at work. Figure 3.4 shows the behavior of the coupling coefficient in regard to the incidence angle. It is important to note here that the fluence depicted in that figure is the actual fluence at the target surface. This means that the original pulse energy was increased for higher incidence angles in order to guarantee a constant fluence at the target.

This secondary effect is caused by the variation of the electromagnetic permeability on the surface layer of the target [38]. The permeability influences the reflection and absorption of the laser beam, which has an effect on the ablation process. The electromagnetic permeability itself is dependent on the local temperature and density of the debris object and thus varies during the ablation. While simulations such as the aforementioned VLL can account for this and calculate the appropriate reflectivity, no simple analytical models exist for this effect.

A possibility to approximate this effect would be the creation of a database for every laser configuration including as many polarizations and incidence angles as possible, in order to interpolate an approximate value. The effort and time needed to create and implement this database was deemed

[1] Used with kind permission of S. Scharring

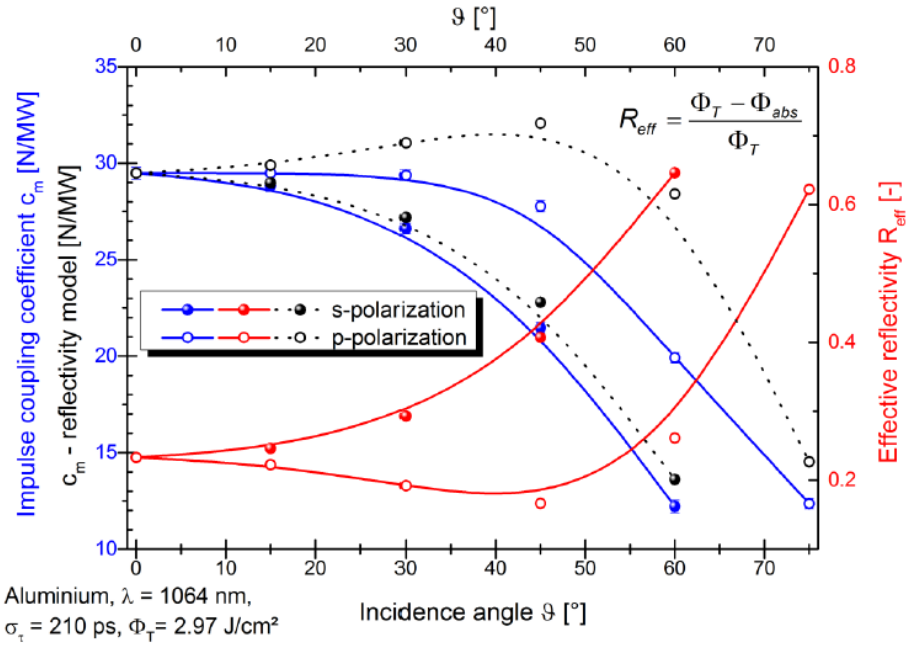

Figure 3.4.: Behavior of coupling coefficient and reflectivity vs. incidence angle from [16]. Any geometrical effects were corrected for, in order to keep the fluence Φ_T on the target constant.

too excessive for this thesis and thus these effects will not be considered in the simulation in the next chapter.

3.5. The area matrix approach

In [25] the effect of various geometries on the impulse vector areinvestigated. This chapter focuses on this analytical method: The area matrix approach.

The foundation of this method is equation 3.3 with the coupling coefficient c_m, the incident laser energy E_p and the normal $\boldsymbol{n}$ for a given element of the debris geometry.

$$m\frac{dv}{dt} = -c_m\frac{dE_p}{dt}\boldsymbol{n} \tag{3.3}$$

With the element surface A, and a laser beam with the intensity I and the direction $\boldsymbol{k}$ the energy can be defined by equation 3.4.

$$\frac{dE_p}{dt} = -AI\boldsymbol{k}\cdot\boldsymbol{n} \tag{3.4}$$

It is important to note here that I is assumed to be an average value. If the energy of an individual pulse E_{pulse} and the repetition rate ν are known, I can be calculated, as shown in equation 3.5:

$$I = E_p \cdot \nu \tag{3.5}$$

Another note in regard to equation 3.4: The scalar product of $\boldsymbol{k}$ and $\boldsymbol{n}$ describes the influence of the angle of incidence of the laser beam. Since both vectors have a length of 1 they are equivalent to $cos(\theta)$ and thus account for the lower incoming fluence that occurs when the angle of incidence increases.

The laser beam can only illuminate areas that are oriented towards the beam. This means that only those surfaces are illuminated for which the scalar product $\boldsymbol{k} \cdot \boldsymbol{n}$ is negative. The negative sign in equation 3.4 accounts for this. If $\boldsymbol{k} \cdot \boldsymbol{n} = 0$, the incoming rays propagate parallel to the surface and no illumination occurs.

If equation 3.4 is substituted into equation 3.3 the result is

$$m\frac{d\boldsymbol{v}}{dt} = C_m I A \boldsymbol{k} \cdot \boldsymbol{n}\boldsymbol{n} \tag{3.6}$$

Equation 3.7 defines the area matrix after which this method is named. It is formed from the sum of all exposed surfaces.

$$\boldsymbol{G} = \sum A_i \boldsymbol{n}_i \boldsymbol{n}_i \tag{3.7}$$

Substituting equation 3.7 into equation 3.6 results in equation 3.8.

$$m\frac{d\boldsymbol{v}}{dt} = c_m I \boldsymbol{k} \cdot \boldsymbol{G} \tag{3.8}$$

$\boldsymbol{G}$ is the area matrix after which the method is named. At this point the author makes the assumption that since the mass loss is small, the mass and the surface stay constant and that $\boldsymbol{G}$ is not time-dependent but constant. Additionally, it is assumed that the coupling coefficient is constant and does not vary as described in section 3.4.

For a more detailed description and examples, refer to the publications [26] and [25].

3.5.1. Assumptions and limitations

While the area matrix approach is a quick and handy way to estimate the momentum transfer it is based on some assumptions that limit the scope of effects that can be investigated with its usage.

- c_m is assumed to be constant.
- Constant spatial distribution of fluence.
- No self-shadowing.
- Constant mass.
- Constant laser intensity instead of pulsed laser radiation.

While the area matrix approach could, in theory, account for some of these effects, this quickly leads to lengthy and complex calculations that necessitates the use of numerical tools and models.

3.5.2. Inverse numerics

Interestingly, the assumption that the laser intensity is continuous, causes an interesting type of error. In reality, each laser pulse is a nearly instantaneous event that alters the linear and angular momentum in discrete steps. The area matrix approach, however, assumes a continuous illumination. This error is exactly opposite to the error encountered in usual numerical approaches, which occur when transforming a continuous system into a discrete system. Here a discrete system is approximated as continuous, which causes errors similar but opposite to the normal errors found in numerical integration. As in the case of discretization errors, the magnitude of the error depends

the size of the time steps, with the unique difference, that the discretized version is the correct depiction of reality. So, if the repetition rate is high this approach is valid, but lower repetition rates can cause noticeable errors when calculating the impulse transfer assuming a continuous irradiation.

4 Numerical Modeling: EXPEDIT

This chapter will give an overview over the numerical models and methods used to simulate laser ablation on a debris target within the program EXPEDIT [1] (**E**xamination **P**rogram for irr**e**gularly shape**d** Debr**i**s **T**argets), which was created by the author during this thesis. While this chapter follows the structure of the program, the descriptions focus on the physical attributes being modeled. The actual code will not be presented here, but can be found on the "Appendix-DVD" as well as an extensive documentation created with Doxygen [49]. If the reader wants to delve into the details of the code, referring to the Doxygen documentation is recommended, since it was generated with the explicit goal of explaining the actual code.

Requirements

The main goal of this thesis is the development of a numerical model capable of analyzing the reaction of debris objects of arbitrary geometry to laser ablation. In particular, the following tasks shall be undertaken by the tool:

- Loading the geometry from the specified input files.
- Flexibility of using various means to generate the geometry.
- Calculation of the irradiation parameters.
- Determination of the irradiated surface area.
- Consideration of shadow effects.
- Calculation of the local coupling coefficient.
- Calculation of the resulting linear and angular momenta.
- Calculation of the resulting linear and angular velocities.

Especially the geometry requirements lead to heightened complexity. On one hand, simple geometric shapes must be handily created and quickly calculated. On the other hand, complex shapes also have to be handled by the program. Furthermore, an important requirement was the creation of code that would be extendable without extensive effort. So extra care was taken to allow for quick modifications and addition of new functionalities.

[1] The patron saint invoked against procrastination

Time step

A major assumption is made to simplify the following deliberations and calculations: The momentum transfer of a single laser pulse is considered to be an instantaneous event. In reality, the momentum transfer is distributed throughout the pulse duration and beyond. The pulse duration can be in the femtosecond regime but for CLEANSPACE a 1 to 10 ns pulse duration was chosen [16]. An exact calculation of the momentum transfer would necessitate, e.g., hydrodynamic calculations like those performed in the VLL software [38]. Since VLL needs multiple hours of runtime to calculate a single pulse, this would create long runtimes. But since these processes take place in the nanosecond regime, these events are many orders of magnitude quicker than the repetition period. As the repetition rate is in the 10 Hz regime, this results in 5-6 orders of magnitude difference between these two time frames.

Since no external forces affect the debris between two pulses, neglecting orbital forces, the linear and angular momenta stay constant. But since the position at the next pulse depends on the angular velocity, the behavior still is nonlinear. The modelling of the kinetics between two pulses is described in section 4.4.6.

4.1. Coordinate systems and geometric parameters

The core module of EXPEDIT only contains two objects: The laser source and the debris object. In order to describe their position, a 'global' coordinate system with the coordinates x_{ECI}, y_{ECI} and z_{ECI} was used. This coordinate system shall be inertial and is constructed similar to the ECI [48] coordinate system so that the implementation of an orbital simulation is possible.

The elements that form the geometry of the debris object are described by a set of vectors in a coordinate system that, while parallel to the global system, has its origin in the center of mass of the debris object. This is not a body-fixed coordinate system, the coordinates of all points, except the center of mass, are changed according to the orientation of the debris object. Each part of the geometry has a position vector $\boldsymbol{l}$ that corresponds to the straight line between the center of mass and the base point of each element. In addition, each element contains a number of vectors that denote the position of the other corners of the element relative to the base corner.

4.2. Input

4.2.1. Control parameters

Since a complete discussion of all control parameters would be excessive, the following list will only contain fairly superficial commentary. For more detailed information, refer to the aforementioned Doxygen documentation. If not mentioned otherwise, SI units are used.

MethodSwitch: Controls which method is used: area, net or beam. For descriptions see section 4.4.2.

BeamResolution: Resolution used in beam method described in section 4.4.2.

NetResolution: Resolution used in net method described in section 4.4.2.

FilterL: Sets the minimum accepted change in angular momentum. Used to filter discretization errors caused by the beam method.

AllowMovement: Controls in which axis translational motion of the debris object is allowed.

Runtime: Runtime of simulation.

4.2.2. Input parameters

These parameters control which input files are used, and tell the input methods which data format to expect.

NameOfGeometryFile: Name of the file that contains the geometric input data.

TypeOfGeometryFile: Either XML or STL.

stlThickness: STL files only contain surface data. This allows calculation of volume and mass.

stlDensity: Needed to calculate the mass of objects from STL files.

Psi: Used to rotate the initial configuration around x-axis.

Theta: Used to rotate the initial configuration around y-axis.

Phi: Used to rotate the initial configuration around z-axis.

SwitchSolid: Controls if the density and thickness given above are used to calculate the mass and the inertia tensor or the data of the next section is used.

4.2.3. Solid body parameters

As mentioned above, STL files only contain information regarding the surface of an object. For thin objects the density and thickness above can be used to model a volume, but for 'thick' shapes it is advised to provide EXPEDIT with the mass and the inertia tensor. The user should take care that the orientation used to calculate the inertia tensor in CAD programs is the same orientation that is saved in the STL file.

Mass: Mass m of total debris object.

CenterOfMass: Center of mass of debris object.

InertiaTensor: Inertia tensor $\boldsymbol{I}$ of debris object.

4.2.4. Laser parameters

These are the parameters that control what kind of laser beam is going to be simulated.

Fluence: Fluence of the laser beam to be simulated: Φ_L.

Frequency: Repetition rate ν.

Diameter: Diameter of laser ray used for beam method. Controls how large the cross-section being scanned by the beam method is.

FluenceDistribution: Controls if top hat or Gaussian distribution is assumed for the spatial profile of the laser beam.

FWHM: Used to alter Gaussian distribution.

DiameterForComparison: The parameters of the Gaussian distribution are calculated on the basis, that the total energy is equal to the energy of a beam with the constant fluence given above and this diameter.

ECI: Position of laser system in global coordinates.

FollowTarget: Controls whether the laser follows the target or lets it slide out of beam.

CenterOfHit: Sets offset between middle of beam and center of mass of debris object.

4.2.5. Laser-matter interaction parameters

These parameters define how the laser-matter interaction is modelled and thus mainly affects the coupling coefficient.

ConstCM: Controls how the coupling coefficient is modelled.

CM: If coupling coefficient is assumed to be constant, this value is used.

a0-a5 : Coefficients used to model the coupling coefficient. Further explanation in section 4.4.3.

t1-t4 : Coefficients used to model the coupling coefficient. Further explanation in section 4.4.3.

4.2.6. Debris parameters

Most information regarding the debris object is given in the geometry files, so these parameters are limited to the initial position and the initial angular velocity. EXPEDIT uses the equations given in section 4.4.6 to calculate the initial angular momentum from the initial rotational velocity. While this is not as intuitive as the angular velocity, this step is necessary in order to correctly model the rotation.

InitialPosition: The initial position of the debris object in the global coordinate system.

InitialAngularVelocity: The initial angular velocity of the debris object.

4.2.7. Modes parameters

Only listed here for completeness, these parameters change for every mode. For information regarding the mode operations refer to section 5.5. While critical to the analysis of certain cases, from a programming point of view they are simply scripts in order to automatically repeat the calculation described in this chapter.

4.2.8. Simple shapes

In order to allow the quick generation of a selection of standard geometric shapes, XML files can be read by the program. The standard set of shapes consists of rectangles, triangles and spheres. The template for the XML file can be found in appendix B. Each piece of the shape can be assigned an individual value for density, so that a debris object made from different materials can be simulated.

It is noteworthy that all geometries described below are considered as a surface, since the internal volume does not affect the laser-matter interaction. Thus it is assumed for the simple geometric shapes that they are so thin they can be treated as two-dimensional entities. If they contain a thickness information, it is only used to calculate the mass, not for any other purpose.

Plates

Each plate is defined by the coordinates of the four corners as well as its thickness, material and density. The methods and functions demand that the plate is in fact a rectangle, other four-sided shapes are not supported.

Of the four corners of the rectangle, the first is designated as the base point and its position relative to the center of mass of the entire debris object becomes the position vector $\boldsymbol{r}_{base}$ of the rectangle. Of the three vectors connecting the base point to the other points, two are perpendicular to each other (since it is a rectangle) and they represent two edges. If these edges are defined as the direction vectors $\boldsymbol{r}_1$ and $\boldsymbol{r}_2$ then every point $\boldsymbol{r}_{rec}$ on the rectangle can be represented by equation 4.1. Locations at which equation 4.2 or 4.3 are not valid, lie within the plane of the rectangle element but not actually within the rectangle. These definitions are needed in section 4.4.2.

$$\boldsymbol{r}_{rec} = \boldsymbol{r}_{deb} + \boldsymbol{r}_{base} + s\boldsymbol{r}_1 + t\boldsymbol{r}_2 \tag{4.1}$$

$$0 <= s <= 1 \tag{4.2}$$

$$0 <= t <= 1 \tag{4.3}$$

Triangles

Similarly to rectangles, each triangle is defined by three points, thickness, material and density. As with rectangles, if the first point is defined as $\boldsymbol{r}_{base}$ and the vector, to the other vertices as $\boldsymbol{d}_1$ and $\boldsymbol{r}_2$ equation 4.4 describes all points within the triangle.

$$\boldsymbol{r}_{tri} = \boldsymbol{r}_{debris} + \boldsymbol{r}_{base} + s\boldsymbol{r}_1 + t\boldsymbol{r}_2 \tag{4.4}$$

$$0 <= s + t <= 1 \tag{4.5}$$

In addition to equations 4.2 and 4.3, equation 4.5 also has to be fulfilled. Otherwise equation 4.4 would define a parallelogram.

Triangles were implemented to allow the approximation of any other shape, if enough triangular elements are combined.

Spheres

Instead of the points given above to define a shape, spherical elements are determined by their center and radius, as well as density and material. Spheres are considered to be solid and the mass is calculated accordingly. For reasons that will be explained in section 4.4.2, spherical elements do not require the cumbersome geometrical definitions needed for triangles and rectangles.

4.2.9. Complex shapes

While the generation of simple shapes with the method above works well, complex shapes require a large number of elements so the manual generation of these files would be arduous. In order to allow the calculation of complex elements, input methods for STL files were written. STL files contain surface information in the form of triangular surface elements and are supported by a large

number of programs and tools. So external programs, such as **SolidEdge** or **MeshLab**, can be used to construct geometries and export the surfaces as STL files. The triangles are copied from the STL files and saved as instances of the internal triangle class and are then used in further calculations.

4.2.10. Solid Bodies

While complex surfaces can be imported as described above, they are treated as hollow bodies. If no rotational or translational motion occurs this is a valid simplification. However, if any type of motion occurs, the mass and the inertia tensor have to be given by the user. They can be calculated either using the same program that generated the shape or through other means. However if the debris object actually is thin and plate-like EXPEDIT can calculate the appropriate inertia tensor itself.

4.2.11. Inertia tensor

If any type of rotation shall be modelled, the inertia tensor is a crucial parameter, which has to be calculated or given by the user. The exact calculation is discussed in section 4.4.6.

4.2.12. Other information

Each element added to the debris object is evaluated by the code and the normals are calculated, which are needed later in order to calculate the angle of incidence and other parameters.

4.3. main()

In EXPEDIT the main function only reads the control and geometry file. The actual calculation defined there is undertaken in MainCore() and will be presented in section 4.4. Additionally, main() selects the appropriate mode. These are functions that call the MainCore()-calculation repeatedly and vary a specified number of parameters in order to examine the results over a broad spectrum of input parameters. The following functions only differentiates with respect to the number of parameters to be varied. For a list of the modes, refer to chapter 5.5.

MainMode1D()

If this mode is used, the calculation is done repeatedly and a single parameter is changed as specified.

MainMode2D()

In this mode two parameters are varied and the calculation repeated thereafter.

MainMode3D()

As one might expect, in this mode three parameters are varied. This includes, however, mostly variations using a position vector (three components) or the angular momentum.

RandomMode()

This mode merits special attention and the applicability but the explanations are closely tied to the results of the primary calculations, thus they will be discussed in section 5.5.7. Briefly summarized, this mode varies the input parameters randomly and thus allows sampling from a large pool of possibilities.

4.4. MainCore()

After the modes described above have altered the input parameters, these are used in the core function, MainCore(). Figure 4.1 shows the call graph for the basic calculation procedure. While the graph is not chronically correct, the following sections are in the call order and describe the significant components of the code. A rough sketch of the processes used to model the laser-debris interaction can be found in figure 4.2.

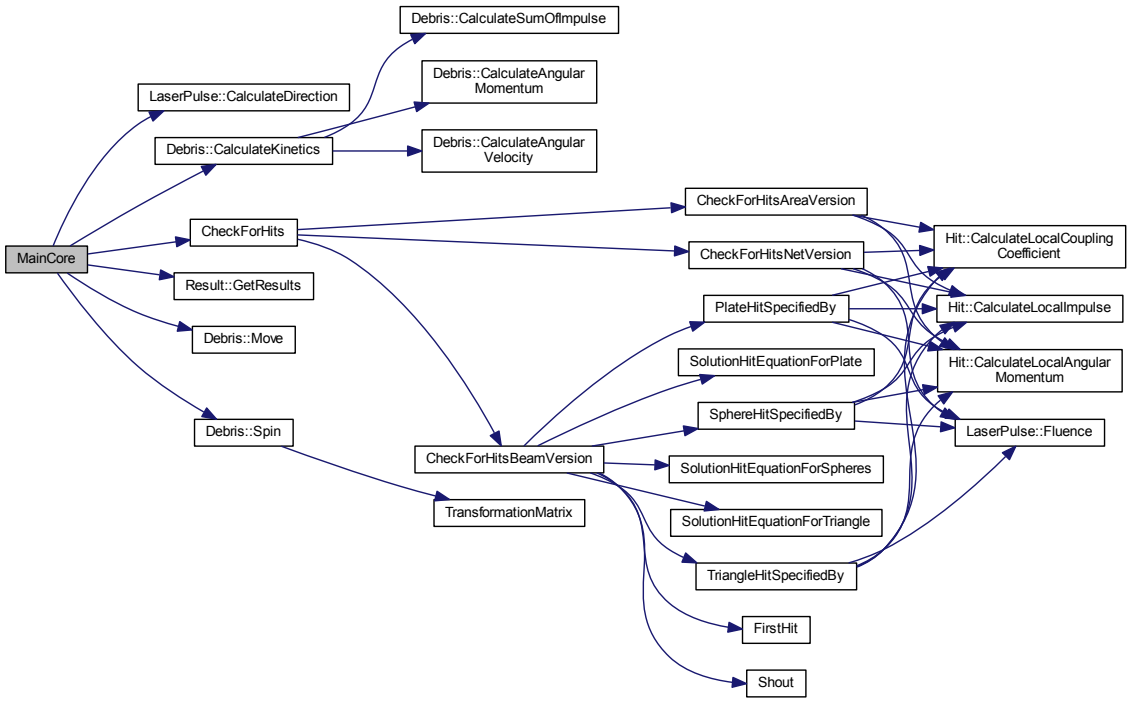

Figure 4.1.: Call graph of MainCore()

4.4.1. Hit

First a brief description of the Hit class is given, which is vital for modeling the laser-matter interaction. A Hit is a single point of interaction, with the appropriate values. The following list contains all members and methods of the Hit class.

polarization: Information regarding the polarization of the incoming laser beam.

angleOfIncidence: Angle of incidence of the incoming laser beam.

fluence: Fluence of the laser beam at this distance from the center: Φ_L.

localFluence: Fluence that actually reaches the surface, after considering the angle of incidence: Φ_T.

surfaceArea: Surface area associated with this Hit instance.

distanceFromLaser: Distance from the laser station, used to determine the first Hit of every beam.

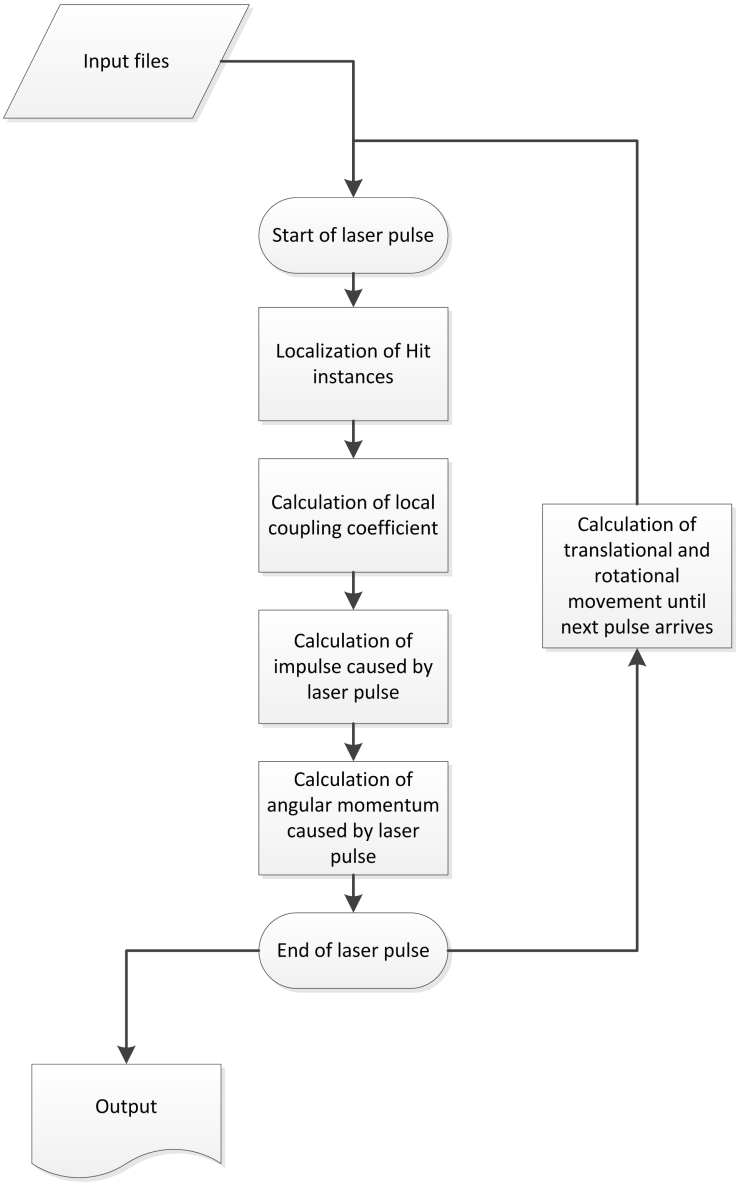

Figure 4.2.: Simplified flowchart for the simulation of the laser-debris interaction within EXPEDIT

localCouplingCoefficient: Coupling coefficient at this point of interaction.

positionECI: Position of this Hit in the global coordinate system.

positionSatCS: Position of this Hit in the debris coordinate system.

impulse: Impulse caused by this Hit instance.

angularMomentum: Angular momentum caused by this Hit instance.

CalculateLocalCouplingCoefficient: Method for calculating the local coupling coefficient, see section 4.4.3.

CalculateLocalImpulse: Method for calculating the impulse caused by this Hit, see section 4.4.4.

CalculateAngularMomentum: Method for calculating angular momentum caused by this Hit, see section 4.4.5.

4.4.2. CheckForHits()

The first step in calculating all parameters in regard to an instance of the Hit class, is the localization of the individual Hits. Since the localization plays a major role in simulating self-shadowing and other effects, different methods were developed and implemented and will be discussed at length in the following sections.

In addition to the geometric position, each Hit needs additional information: Fluence, angle of incidence and irradiated surface area are needed for the following calculations.

CheckForHitsAreaVersion()

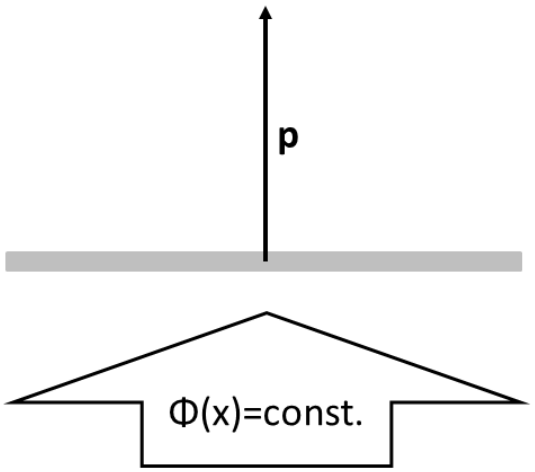

Figure 4.3.: Area approach: The impulse generated on a surface is calculated by assuming constant fluence Φ_T and a constant coupling coefficient c_m for the entire surface.

This method is the simplest and quickest in regard to computation time, but is not able to account for many effects that will be discussed later in this chapter. Analog to the method described in chapter 3.5, each surface is treated individually and the impulse $\boldsymbol{p}$ is calculated for every surface. In

terms of the Hit class presented above this means each surface is assigned a single instance of the Hit class at the center of mass of the element, as shown in figure 4.3. Since each element has two sides and associated normals, the irradiated side is selected using the requirement in equation 4.6.

$$\boldsymbol{k} \cdot \boldsymbol{n} < 0 \tag{4.6}$$

Similarly, the angle of incidence θ can be found with equation 4.7.

$$\theta = \arccos(-\boldsymbol{k} \cdot \boldsymbol{n}) \tag{4.7}$$

With a rising angle of incidence, the fluence that irradiates the surface decreases, as a smaller part of the laser beam irradiates the same surface. In order to account for this geometrical effect, the local fluence has to be calculated according to equation 4.8.

$$\Phi_T = \cos\theta \, \Phi_L \tag{4.8}$$

The last variable remaining is the surface area which, in this case, simply is the surface area of the element in question. Now all values needed to calculate the impulse and the following parameters are known. This step is described in section 4.4.4.

It should be noted that this method, though handy, is only valid if all parameters stay constant over the entire surface. Spatial variation of the laser beam cannot be accounted for, the same goes for shadow effects. When this method is selected it is assumed that every element has an illuminated surface and thus complex geometries are not calculated correctly. Spatial variation of the fluence causes additional errors, since the coupling coefficient is dependent on the fluence as described in chapter 3.4.

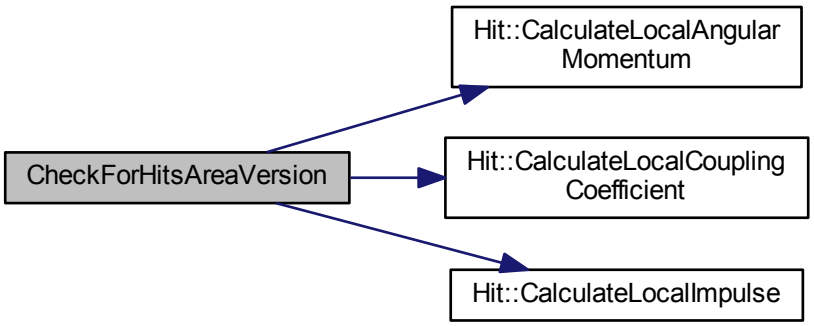

Figure 4.4.: Call graph for CheckForHitsAreaVersion()

Figure 4.4 shows the call graph of the function CheckForHitsAreaVersion() which handles the calculations presented above. Since this is the simplest method of placing Hits, it only requires few other functions, which are discussed in the section 4.4.3 to 4.4.5.

CheckForHitsNetVersion()

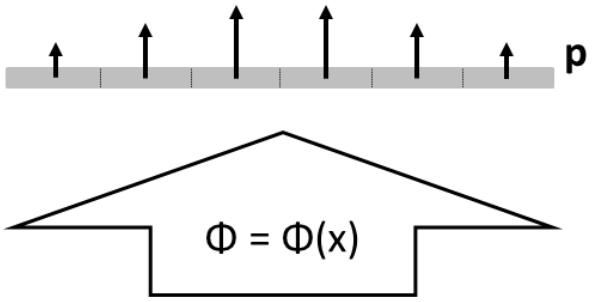

Figure 4.5.: Net method - Discretization of the debris object: Each surface is divided into smaller surfaces which each can have individual values for the fluence Φ_T and the coupling coefficient c_m.

This variant of the area approach allows the investigation of additional phenomena, with the price of additional computation time. Each surface is divided into multiple individual areas, each with their own center of mass and surface area. Each piece is issued their own instance of the Hit class and thus can have an individual fluence and coupling coefficient. In regard to the calculation of local fluence, angle of incidence and surface area, the parts are treated exactly as described in the previous section, with the difference that the surface area is the appropriate fraction of the total surface area of the element.

Figure 4.6 shows the call graph, which in comparison to figure 4.4 has only the additional function Fluence(), which returns the fluence depending on the distance from the center of the beam, thus modelling spatial distributions, specifically the Gaussian type.

CheckForHitsBeamVersion()

Another option lies in scanning the surface of the debris geometry from point of view of the laser beam. The original beam is separated into a multitude of smaller rays, depending on the designated resolution. Each ray has a different point of origin $\boldsymbol{r}_{station}$ but they all share the propagation vector $\boldsymbol{k}_{laser}$. All points on the one-dimensional laser beam can be defined by these vectors as shown in 4.9:

$$\boldsymbol{r}_{laser} = \boldsymbol{r}_{station} + j\boldsymbol{k}_{laser} \tag{4.9}$$

In order to calculate if and where the laser beam intersects in $\boldsymbol{r}_e le$, equation 4.10 has to be solved.

$$\boldsymbol{r}_{laser} = \boldsymbol{r}_{ele} \tag{4.10}$$

For triangular and rectangular elements this can be achieved by substituting $\boldsymbol{r}_{ele}$ with equation 4.1 or 4.4. In both cases this leads to equation 4.11

$$\boldsymbol{r}_{station} + j\boldsymbol{k} = \boldsymbol{r}_{deb} + \boldsymbol{r}_{base} + s\boldsymbol{r}_1 + t\boldsymbol{r}_2 \tag{4.11}$$

which leads to the systems of linear equations shown in equation 4.12:

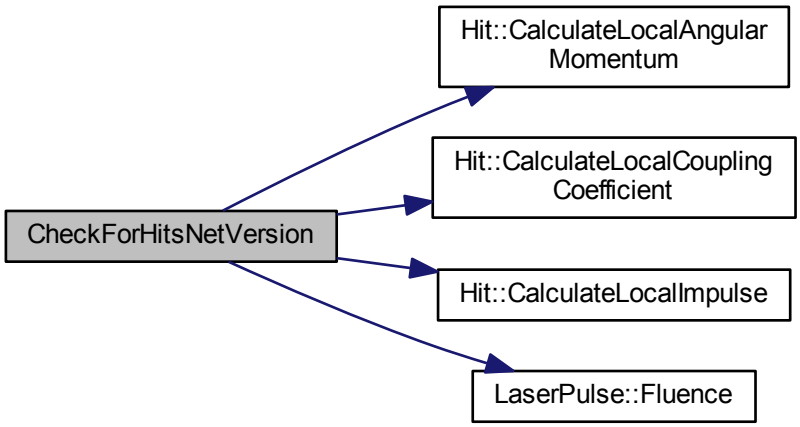

Figure 4.6.: Call graph for CheckForHitsNetVersion()

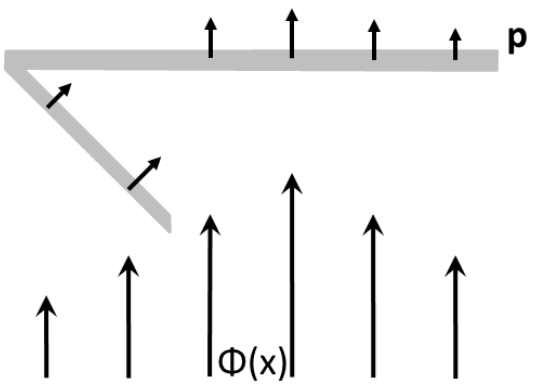

Figure 4.7.: Beam method - Discretization of the laser beam: The laser beam is divided into many individual beams, each with individual fluence Φ_F. The first intersection of each ray with the debris object is evaluated in order to calculate the local coupling coefficient c_m and the resulting impulse $\boldsymbol{p}$.

$$\boldsymbol{r}_{station} - (\boldsymbol{r}_{deb} + \boldsymbol{r}_{base}) = \begin{pmatrix} \boldsymbol{r}_1 & \boldsymbol{r}_2 & -\boldsymbol{k} \end{pmatrix} \begin{pmatrix} s \\ t \\ j \end{pmatrix} \tag{4.12}$$

which can be solved using equation 4.13:

$$\begin{pmatrix} \boldsymbol{r}_1 & \boldsymbol{r}_2 & -\boldsymbol{k} \end{pmatrix}^{-1} (\boldsymbol{r}_{station} - (\boldsymbol{r}_{deb} + \boldsymbol{r}_{base})) = \begin{pmatrix} s \\ t \\ j \end{pmatrix} \tag{4.13}$$

If the solution of this system of linear equations fulfills the requirements laid out in equation 4.2, 4.3 and, if applicable, 4.5, a valid intersection between this beam and the element in question has been found.

For spheres these equations are simpler. If $\boldsymbol{c}$ is the center point of the sphere, r the radius, then equation 4.14 gives us all points on the surface, $\boldsymbol{r}_{sphere}$:

$$||\boldsymbol{r}_{sphere} - \boldsymbol{c}||^2 = r^2 \tag{4.14}$$

If combined with equation 4.9 the solution of the resulting quadratic equation is given in equation 4.15 [8]:

$$k = \frac{-(\boldsymbol{k} \cdot (\boldsymbol{o} - \boldsymbol{c})) \pm \sqrt{(\boldsymbol{d}_{laser} \cdot (\boldsymbol{o} - \boldsymbol{c}))^2 - ||\boldsymbol{k}||^2(||\boldsymbol{o} - \boldsymbol{c}||^2 - r^2)}}{||\boldsymbol{k}||^2} \tag{4.15}$$

If the value below the square-root is negative, no intersections between the laser beam and the sphere exist. If it is positive two intersections exist and the intersection closest to the laser source is chosen. The only value missing at this point is the normal for the intersection point, which simply is the vector from the center of the sphere to the intersection point.

In order to find every intersection, the equations above have to be solved for each beam and geometry element, resulting in high runtimes. While the quadratic equations used for spheres are quick, the systems of linear equations used for triangular and rectangular elements demand the inverse of a matrix, which is an computationally expensive operation. Thus, this method takes much more runtime then the method mentioned earlier.

Since a single beam can intersect multiple elements of the geometry, only the intersection with least distance to the laser station is actually used in the following calculations. Thus, self-shadowing can be simulated. Additionally, since each beam is assigned an individual fluence, spatial variations thereof can be taken into account.

Once the intersection is found, the illuminated surface and the local fluence are calculated using the angle of incidence.

The discretization of the beam introduces numerical errors into the calculation, which while controllable, offer interesting insights into the stability of the system and will be further discussed in section 5.5.2.

Figure 4.8 shows the call graph for the beam method, which is far more involved than the earlier methods due to specific functions for finding the first intersection for every beam (FirstHit()), the functions that solve the systems of linear equations discussed above (SolutionHitEquationForPlate(),

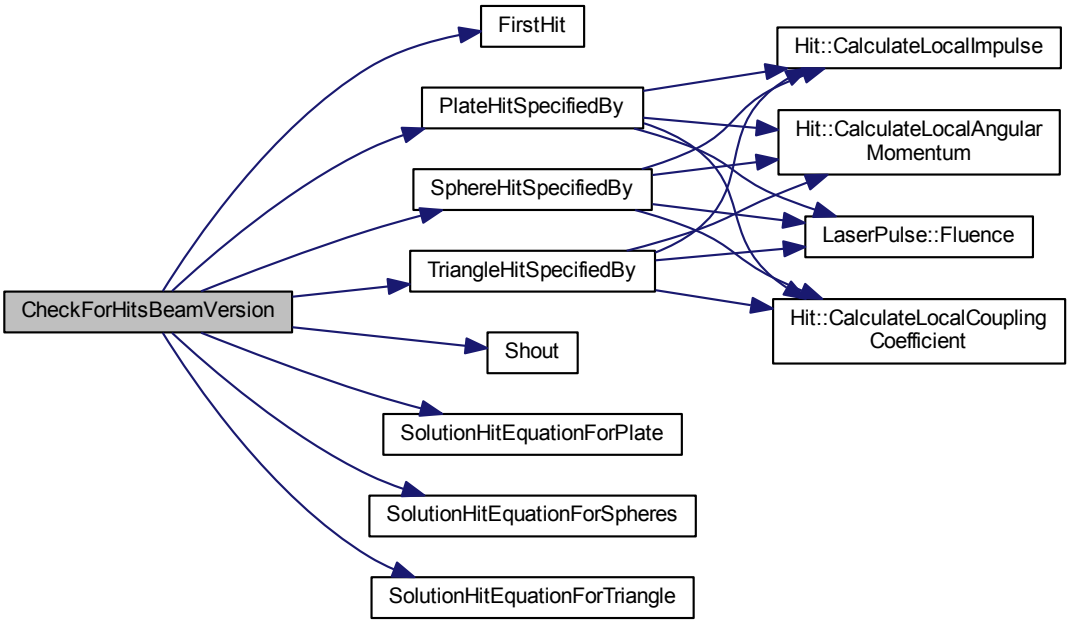

Figure 4.8.: Call graph for beam method

-Triangle() or -Sphere()) and the functions that calculate the exact location of the intersection based on the solution provided by the solver function (Plate-, Triangle- or SphereHitSpecifiedBy()).

4.4.3. CalculateLocalCouplingCoefficient()

As mentioned in chapter 3.4 c_m can be defined as

$$c_m = \frac{\Delta p}{E_p} = \frac{\Delta m_{jet} \cdot v_{jet}}{E_p} \tag{4.16}$$

Using the change in mass Δm and the velocity of the exhaust plume v_{jet}. If the specific impulse I_{sp}

$$I_{sp} = \frac{v_{jet}}{g} \tag{4.17}$$

is used to substitute v_{jet}, then c_m can be written as

$$c_m = \frac{\Delta m \cdot g \cdot I_{sp}}{E_p}. \tag{4.18}$$

If divided by the irradiated surface this results in equation 4.19:

$$c_m(\Phi_T) = \frac{m_a(\Phi_T) \cdot g \cdot I_{sp}(\Phi_T)}{\Phi_T} \tag{4.19}$$

With the mass loss per surface area m_a and the specific impulse I_{sp} can be modelled using the templates in equations 4.20 and 4.21.

$$m_a(\Phi_T) = a_0 + a_1\left(1 - Exp\left(\frac{-\Phi_T}{t_1}\right)\right) + a_2\left(1 - Exp\left(\frac{-\Phi_T}{t_2}\right)\right) \tag{4.20}$$

$$I_{sp}(\Phi_T) = a_3 + a_4\left(1 - Exp\left(\frac{-\Phi_T}{t_3}\right)\right) + a_5\left(1 - Exp\left(\frac{-\Phi_T}{t_4}\right)\right) \tag{4.21}$$

Using the simulations for a specific pulse length, polarization and material, a fitted curve for $c_m(\Phi)$ can be generated, which is then used by EXPEDIT to calculate the Impulse transferred. The parameters a_{0-5} and t_{1-4} can be entered into the XML-files and are then used to calculate the local coupling coefficient.

4.4.4. CalculateLocalImpulse()

After the coupling coefficient is determined, equation 4.22 is used to calculate the impulse caused by the Hit instance. It is noteworthy that all parameters in that equation refer to the local variables, which can differ significantly for different parts of the debris object.

$$\Delta \boldsymbol{p} = -\boldsymbol{n} c_m \Phi_T A \tag{4.22}$$

4.4.5. CalculateAngularMomentum()

If the impulse caused by a single instance of the Hit class is known, the accompanying angular momentum can simply be calculated with equation 4.23, with $\boldsymbol{r}$ as the position relative to the center of mass.

$$\Delta \boldsymbol{L} = \boldsymbol{r} \times \Delta \boldsymbol{p} \tag{4.23}$$

Kinematic torque

In addition to the torque caused by laser ablation, another type of torque is created if the debris object is spinning with an angular velocity $\boldsymbol{\omega}$ at the time of the impulse transfer: the direction of the exhaust plume is not entirely normal to the surface of the debris object but has a component in the $\boldsymbol{r} \times \boldsymbol{\omega}$ direction and thus causes a torque. The following brief summary is based on the findings in [25].

The ratio of standard torque to kinematic torque is given by equation 4.24

$$\frac{\text{kinematic torque}}{\text{static torque}} = \frac{\boldsymbol{\omega} \times \boldsymbol{r}}{\boldsymbol{v}_{jet}} \tag{4.24}$$

with v_{jet} being the velocity of the exhaust plume. This value is typically small [25]. Additionally, the kinematic torque is at its largest when the debris object is fairly round, since then the velocity parallel to the surface, $\boldsymbol{\omega} \times \boldsymbol{r}$, is largest. However, if a debris object is shaped somewhat spherical, the orientation does not matter as much as in the case of a plate-shaped debris object. Additionally, in [25] it is pointed out that in most cases the kinematic torque is counteracted by the mass loss of the debris object which decreases the inertia tensor, which would increase ω. For some shapes, such as a cylinder and a sphere, in [25] it is showed that these effects neutralize each other. After taking this information into account it was decided to neglect the kinematic torque. In order to correctly simulate it, the local mass loss would have to be simulated, which similar to c_m is dependent on

many variables. While possible, the work in order to simulate an effect that is small in the worst case and neutralizes itself in the best case, was not deemed worth the effort.

4.4.6. Kinetics

While the kinetics do not merit an entire chapter, they do form an important part of the simulation. Because of this the basics are presented here alongside the methods developed to approximate the actual system.

Debris::Move()

Calculation of the translational motion and velocities is fairly straightforward. In section 4.4.4 the derivation of the impulse $\boldsymbol{p}$ was discussed. As soon as the impulse is known, the velocity change can be calculated by equation 4.25:

$$\boldsymbol{v}_{i+1} = \boldsymbol{v}_i + \Delta\boldsymbol{v} = \boldsymbol{v}_i + \frac{\Delta\boldsymbol{p}_i}{m} \tag{4.25}$$

Since the velocity of the target is increased in discrete steps, the position can be calculated accurately using the left sided rectangle method without the errors usually associated with it.

$$\boldsymbol{x}_{i+1} = \boldsymbol{x}_i + \boldsymbol{v}_i \cdot \Delta t \tag{4.26}$$

Debris::Spin()

While the calculation of the angular momentum described in 4.4.5 is trivial, the calculation of the angular velocity is not. [5] describes the problem and possible solutions in detail. A brief summary is given below.

Given the explanations above, we can assume that for any given moment t_n the angular momentum $\boldsymbol{L}_n$ is known. In order to calculate the resulting angular velocity $\boldsymbol{\omega}_n$, the inertia tensor $\boldsymbol{I}$ has to be determined. If the body is given as a collection of mass points the inertia tensor is given by equation 4.27.

$$\boldsymbol{I} = \sum_i m_i \begin{pmatrix} y_i^2 + z_i^2 & -x_i y_i & -x_i z_i \\ -y_i x_i & x_i^2 + z_i^2 & -y_i z_i \\ -z_i x_i & -z_i y_i & x_i^2 + y_i^2 \end{pmatrix} \tag{4.27}$$

For the rectangle and triangle elements described in chapter 4.2.8, it is assumed that they are two-dimensional planes. In order to calculate their individual inertia tensor they are split into numerous parts, whose centers of mass form the point cloud used above. Spheres are the exception, since their inertia tensor does not depend on the orientation, equation 4.28 can be used without further effort.

$$\boldsymbol{I}_{sphere} = \frac{2mr^2}{5} \begin{pmatrix} 1 & 0 & 0 \\ 0 & 1 & 0 \\ 0 & 0 & 1 \end{pmatrix} \tag{4.28}$$

The equations above only give us the inertia tensor for the center of mass for the respective part of the geometry, hereafter denoted as $\boldsymbol{I}^{(S)}$. Before they can be added, $\boldsymbol{I}^{(S)}$ has to be transformed into the inertia tensor at the center of mass of the entire geometry. In equation 4.29, $\boldsymbol{a}$ denotes the vector between the center of mass of the individual shape and the center of mass of the entire debris

object. An important requirement for the following Huygens-Steiner theorem is the parallelism of the axes of the respective coordinate systems, which is given here by the definition of the different coordinate systems, see section 4.1.

$$\boldsymbol{I} = \boldsymbol{I}^{(S)} + m \begin{pmatrix} a_2^2 + a_3^2 & -a_1 a_2 & -a_1 a_3 \\ -a_1 a_2 & a_1^2 + a_3^2 & -a_2 a_3 \\ -a_1 a_3 & -a_2 a_3 & a_1^2 + a_2^2 \end{pmatrix} \tag{4.29}$$

After the inertia tensor for each element in regard to the common center of mass is known, simple addition of these results in the total inertia tensor of the entire object. The now known $\boldsymbol{I}$ is connected to $\boldsymbol{L}$ and $\boldsymbol{\omega}$ by the fundamental equation of angular motion for rigid bodies:

$$\boldsymbol{L} = \boldsymbol{I}\boldsymbol{\omega} \tag{4.30}$$

The transformation to equation 4.31 allows the determination of $\boldsymbol{\omega}$ from $\boldsymbol{L}$.

$$\boldsymbol{\omega} = \boldsymbol{I}^{-1}\boldsymbol{L} \tag{4.31}$$

As postulated above no external torques apply to the body between two pulses, and as the pulses result in an instantaneous change of the angular momentum, it can generally be assumed that $\boldsymbol{L}$ is constant in the time between two pulses. But, and this is critical, $\boldsymbol{\omega}$ can and does change, since I changes with the orientation of the body.

In order to calculate the orientation of the debris object at the next pulse, a mean angular velocity $\boldsymbol{\omega}_{mean}$ is needed. The simplest approach is to assume a constant $\boldsymbol{\omega} = \boldsymbol{\omega}_{mean}$ which is equivalent to a rectangle rule numerical integration and the errors caused by the same. In cases where $\boldsymbol{L}$ is truly constant this leads to a rise in rotational energy and to an unstable calculation.

In order minimize these errors multiple approaches can be chosen. A higher order approximation of $\boldsymbol{\omega}_{mean}$ can greatly reduce the errors. In [5],various methods are introduced and as a compromise between calculation time and accuracy the following third-order method was selected of them:

$$\boldsymbol{\omega}_i = \boldsymbol{I}_i^{-1}\boldsymbol{L}_i \tag{4.32}$$

$$\dot{\boldsymbol{\omega}}_i = \boldsymbol{I}_i^{-1}(\dot{\boldsymbol{L}}_i - \boldsymbol{\omega}_i \times \boldsymbol{L}_i) \tag{4.33}$$

$$\ddot{\boldsymbol{\omega}}_i = \boldsymbol{\omega}_i \times \dot{\boldsymbol{\omega}}_i + \boldsymbol{I}_i^{-1}(\ddot{\boldsymbol{L}}_i - \dot{\boldsymbol{\omega}}_i \times \boldsymbol{L}_i - 2\boldsymbol{\omega}_i \times \dot{\boldsymbol{L}}_i + \boldsymbol{\omega}_i \times (\boldsymbol{\omega}_i \times \boldsymbol{L}_i)) \tag{4.34}$$

$$\boldsymbol{\omega}_{mean} = \boldsymbol{\omega}_i + \frac{h}{2}\dot{\boldsymbol{\omega}}_i + \frac{h^2}{6}\ddot{\boldsymbol{\omega}}_i + \frac{h^2}{12}\left(\left(\dot{\boldsymbol{\omega}}_i + \frac{h}{3}\ddot{\boldsymbol{\omega}}_i\right) \times \boldsymbol{\omega}_i\right) \tag{4.35}$$

Even though this method delivers much better results than the first-order version, if the calculation runs for many cycles the energy of the rotating body steadily increases, since $\boldsymbol{\omega}_{mean}$ is slightly overestimated.

Once the mean angular velocity is known, equation 4.36 delivers the angles $\Delta\angle$ by which the debris object has turned.

$$\Delta\angle_i = \boldsymbol{\omega}_i t_{step} \tag{4.36}$$

Once the Δ of every angle is known, they can be applied to the rotation matrix discussed in 4.4.6, which is used to transform every part of the geometry to its new position and orientation.

TransformationMatrix()

The orientation of an individual geometry is described by the three angles well known from airplane conventions:

Ψ : Yaw. Describes rotation around the z-axis

Θ : Pitch. Describes roation around y-axis

Φ : Roll. Describes rotation around x-axis

If a rigid body shall be rotated, this rotation can be expressed as the three angles referenced above. The full matrix is defined as in [44]:

$$M = \begin{pmatrix} \cos\Theta\cos\Psi & \sin\Phi\sin\Theta\cos\Psi - \cos\Phi\sin\Psi & \cos\Phi\sin\Theta\cos\Psi + \sin\Phi\sin\Psi \\ \cos\Theta\sin\Psi & \sin\Phi\sin\Theta\sin\Psi + \cos\Phi\cos\Psi & \cos\Phi\sin\Theta\sin\Psi - \sin\Phi\cos\Psi \\ -\sin\Theta & \sin\Phi\cos\Theta & \cos\Phi\cos\Theta \end{pmatrix} \tag{4.37}$$

M can be applied to all points of a debris element, effectively spinning the object by the desired amount. All secondary characteristics of the geometry, such as the inertia tensor, can be rotated using the same transformation matrix M and do not have to be recalculated at every time step.

4.4.7. Comparison

If the fluence is spatially constant and the debris geometry does not shadow itself, e.g., a plate, the results of these methods should be identical. If any kind of variation of the spatial density of the incoming fluence is assumed,e.g. a Gaussian distribution or a grazing shot, the net approach yields accurate results with moderate runtimes. If the geometry is concave and thus subject to self-shadowing only the beam method yields accurate results. Thus, calculation time can be greatly reduced by using the net approach but care has to be taken to make sure the geometry is not subject to self-shadowing.

4.5. Output

The standard output files contain header information naming each column and giving the unit used, always the appropriate SI units without any prefixes. They contain, in this order, the following information. Vectors are given in subsequent columns for the x, y and z dimension.

- Step
- Time
- Impulse $\boldsymbol{p}$
- Velocity $\boldsymbol{v}$
- Position of debris object
- Change in angular momentum $\Delta\boldsymbol{L}$
- Angular Momentum $\boldsymbol{L}$

- Angular velocity ω
- Total rotation of debris object in
  - Yaw
  - Pitch
  - Roll

4.5.1. Output of mode-calculations

These output files do not contain standardized headers since the parameters being varied change from mode to mode. However, the data itself contains the following information. These are accumulated values over the entire runtime of a single calculation which is repeated as specified by the individual mode.

- Parameter 1
- Parameter 2 (if applicable)
- Parameter 3 (if applicable)
- Sum of absolute impulse $\sum |\boldsymbol{p}|$
- Sum of impulse $\sum \boldsymbol{p}$
- Sum of absolute angular momentum $\sum |\boldsymbol{L}|$
- Sum of angular Momentum$\sum \boldsymbol{L}$
- Sum of absolute path travelled by the debris object$\sum |\boldsymbol{s}|$
- Path travelled by the debris object $\sum \boldsymbol{s}$
- Time until debris object has moved one laser beam diameter radially. Used to approximate how quickly the debris object leaves the laser beam.

4.6. Verifcation and Validation

In order to avoid confusion the term validation and verification shall be defined here as by the IEEE in [IEEE-STD-610]:

Software Validation: The process of evaluating software during or at the end of the development process to determine whether it satisfies specified requirements.

Software Verification: The process of evaluating software to determine whether the products of a given development phase satisfy the conditions imposed at the start of that phase.

4.6.1. Validation

The requirements for the tool EXPEDIT are set in the task description of this master thesis. The parameter studies in the following chapter can be seen as a validation. They test if EXPEDIT can deliver the results demanded in the task description.

4.6.2. Verification

At the beginning of this chapter, the requirements of the simulation are postulated. One way of testing to see if the requirements are met, is by comparing the results from certain cases to the results obtained by analytical calculations. The analytical results used for comparison where calculated using the area matrix method from [25] which were discussed in chapter 3.5.

For verification, 10 test cases were compared. The results can be seen in table 4.1. The input values used for the individual cases are noted in appendix C. Some of these cases merit special mention:

Wedge oscillation

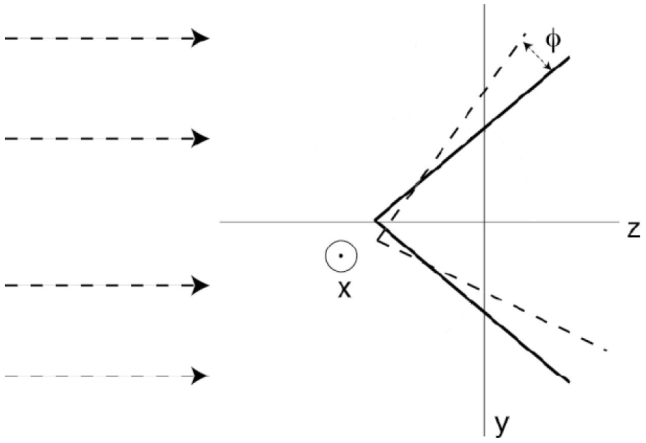

Figure 4.9.: Wedge irradiated by pulsed laser. Based on [25]. This shows the wedge in the stable position. If initial position is rotated around the x-axis, the wedge will begin oscillating. The equations below only remain valid, if no self-shadowing occurs: $|\Phi| \leq 45°$

As described in [25], a wedge that is irradiated as shown in figure 4.9 starts to oscillate. The author derives analytical formulas to calculate the period of the oscillation. For a wedge enclosing an angle of $\frac{\pi}{2}$ the angular frequency can be calculated with equation 4.38, which is based on [25][2]:

$$\omega = \sqrt{\frac{12\sqrt{2}c_m I v h}{10m}} \tag{4.38}$$

Equation 4.39 supplies the period T if only small angles are considered.

$$T = \frac{2\pi}{\omega} \tag{4.39}$$

If large oscillations are regarded, as done in table 4.1, the arithmetic-geometric mean can be used to arrive at the exact solution[6]:

[2]The actual equation in [25] is missing the factor $\sqrt{2}$. Refer to appendix D for the derivation of the equation.

$$T = \frac{2\pi}{M\left(1, \cos\left(\frac{\Phi_0}{2}\right)\right)\omega} \tag{4.40}$$

With the arithmetic-geometric mean $M(x, y)$ of two values and the intial angle of orientation, relative to stable case, Φ_0.

This test case is granted special attention, because it allows a test of the impulse transfer and of the methods modelling the rotation.

Cone oscillation

As above, a cone, if irradiated similarly as the wedge, begins to oscillate. Again this oscillation was simulated and compared in order to investigate the kinematics modules. Equation 4.41, from [25], gives the angular frequency and, as above, equation 4.39 is used to calculate the values given in table 4.1.

$$\omega = \sqrt{\frac{7\sqrt{2}}{3}\left(\frac{\pi^2}{9\rho m^2}\right)^{\frac{1}{3}} c_m I \nu} \tag{4.41}$$

This test is the only case that any discrepancy to the predicted results at all. But since this case combines the most complex method of geometry data and interaction models in addition to the fact that the cone used was constructed from triangular elements and thus only an approximation in itself, the error is within an acceptable margin.

Table 4.1.: Verification results. The columns involving $\boldsymbol{p}$ and $\boldsymbol{L}$ are vectors with the components in x, y and z direction. In the last two cases, the geometries are loaded from STL-files and consist of triangular polygons.

Test Case	Beam		Net		Plane		Liedahl [25]	
	$\boldsymbol{p}$	$\boldsymbol{L}$	$\boldsymbol{p}$	$\boldsymbol{L}$	$\boldsymbol{p}$	$\boldsymbol{L}$	$\boldsymbol{p}$	$\boldsymbol{L}$
Plate1	0	$3.125E-6$	0	$E-21$	0	0	0	0
	0	$3.125E-6$	0	$E-23$	0	0	0	0
	0.00625	0	0.00625	0	0.00625	0	0.00625	0
Plate2	0.00314	$E-6$	0.00313	$E-21$	0.00313	0	0.003125	0
	0	$E-18$	0	$E-18$	0	0	0	0
	0.00314	$E-6$	0.00313	$E-21$	0.00313	0	0.003125	0
Plate3	0	$E-18$	0	$E-18$	0	0	0	0
	-0.00314	$E-6$	-0.00313	$E-23$	-0.00313	0	-0.003125	0
	0.00314	$E-6$	0.00313	$E-20$	0.00313	0	0.003125	0
Sphere	$E-6$	$E-23$	-	-	0	0	0	0
	$E-6$	$E-22$			0	0	0	0
	0.01309	$E-22$			0.01309	0	0.1309	0
Sphere mesh	-	-	-	-	$E-7$	$E-7$	0	0
					$E-6$	$E-8$	0	0
					0.1303	$E-23$	0.1309	0
Wedge1	0	$1.59375E-4$	0	$1.5625E-4$	0	$1.5625E-4$	0	$1.5625E-4$
	0	$E-6$	0	$E-23$	0	0	0	0
	0.00625	0	0.00625	0	0.00625	0	0.00625	0
Wedge2	0	$E-6$	0	$E-10$	0	$E-10$	0	0
	$E-5$	$E-6$	$E-19$	$E-24$	0	0	0	0
	0.00625	$E-8$	0.00625	$E-20$	0.00625	0	0.00625	0
	Period of oscillation		Period of oscillation		Period of oscillation		Period of oscillation	
Wedge	148 steps $\widehat{=}$ 0.74 s		148 steps $\widehat{=}$ 0.74 s		148 steps $\widehat{=}$ 0.74 s		0.7376 s	
Wedge mesh	-	-	-	-	148 steps $\widehat{=}$ 0.74 s		0.7376 s	
Cone mesh	-	-	-	-	264 steps $\widehat{=}$ 1.32 s		1.29 s	

5 Parameter studies

In this chapter the parameter studies performed for this thesis are presented. This serves two purposes: On one hand it illustrates the capabilities of EXPEDIT and on the other hand the analysis of the generated data allows studies in regard to the laser-based deorbit concept.

5.1. Coupling coefficient

All of the following data was generated using the same coupling coefficient curve for its sensitivity in regard to the fluence. The curve in figure 5.1 is the result of simulations with the VLL code described in section 3.4 for a 500 ps pulse with a wavelength of 1064 nm for varying pulse energies [16]. This data is used in all subsequent calculations.

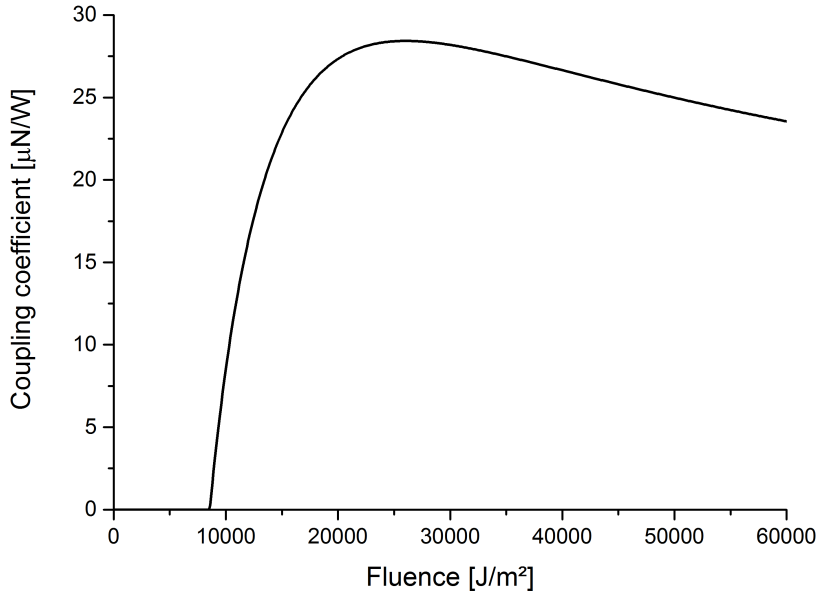

Figure 5.1.: Values for coupling coefficient gained from VLL simulations for a pulse length of 500 ps and a wavelength of 1064 nm. The parameters used for the fit presented in section 4.4.3 are $a_1 = -0.01314 \frac{\mu g}{cm^2}$, $a_2 = 0.01753 \frac{\mu g}{cm^2}$, $a_3 = 0.01904 \frac{\mu g}{cm^2}$, $a_4 = 449.81\,s$, $a_5 = 632.06\,s$, $a_6 = 913.51\,s$, $t_1 = 15.04 \frac{J}{cm^2}$, $t_2 = 1.19 \frac{J}{cm^2}$, $t_3 = 2.41 \frac{J}{cm^2}$ and $t_4 = 23.38 \frac{J}{cm^2}$.

As mentioned in chapter 3.4 the coupling coefficient and its dependency on the fluence are dependent on various variables. In order to offer a complete overview over this topic the following calculations would have to be repeated for various different materials, pulse lengths and wavelengths in order to examine the effects of changing coupling coefficient. At this moment, the only material for which the coupling coefficient can be simulated quickly is aluminum. However, at longer

pulse lengths (1-10 ns were evaluated during the CLEANSPACE-program) the coupling coefficient curve does not change its shape, the general behavior compromised of ablation threshold, optimum and plasma-zone stays similar. Thus, the following results should be comparable for other pulse durations if the fluence is regarded as a multiple of Φ_{opt}.

5.2. Figures of merit

A figure of merit is needed to compare different cases that will be examined in this chapter. η_c, as defined in equation 5.1, was used in this fashion in [34] to account for impulse loss due to "effects of improper thrust direction on the target, target shape effects, tumbling, etc."[34]. By this definition η_c is supposed to account for all effects this thesis investigates, and thus this thesis could be interpreted as the effort to gain an estimate of η_c. The author himself cites $\eta_c \approx 0.3$ for plate-shaped debris, using the geometrical discussions in [26].

$$\eta_c = \frac{p_{eff}}{p_{ref}} \tag{5.1}$$

While for plates the calculation of p_{ref} is clear, the plate is perpendicular to laser beam, for complex shapes, the calculation is not as straightforward. For a sphere the reference case is a plate with the same area as the sphere's cross-section. But for irregular geometries, a comparable value for the cross-section is difficult to define.

In order to gain clarification for the following parameter studies, η_j , as defined in equation 5.2, was introduced for this thesis and will be used for their evaluation. In section 4.3 the values for both figures of merit are compared in figure 5.15. There it can be seen that η_c and η_j exhibit the same behavior, the only difference is the factor $\frac{p_{ref}}{p_{opt}}$.

$$\eta_j = \frac{p_{eff}}{p_{opt}} \tag{5.2}$$

However, η_j and η_c only incorporate the loss of impulse parallel to the direction of the laser beam, hereafter referred to as axial impulse $\boldsymbol{p}_{axial}$, whereas it neglects the additional, unwanted impulse created perpendicular to the laser beam, hereafter referred to as radial impulse $\boldsymbol{p}_{radial}$. For this thesis ξ was introduced, which will be used forthwith to describe the ratio of radial to axial impulse components as shown in equation 5.3:

$$\xi = \frac{p_{radial}}{p_{axial}} \tag{5.3}$$

In light of the separation into axial and radial components it is sensible to redefine η_j according to equation 5.4:

$$\eta_j = \frac{p_{axial,eff}}{p_{axial,opt}} \tag{5.4}$$

In the following sections, especially in section 5.5.7, both ξ and η_j will be used to compare different cases and to assess their viability. Configurations with a high η_j are desirable since they minimize the energy need in order to affect the desired orbit changes.

A high value for ξ is not inherently bad, but problematic nonetheless. Since it is not specified, the possible directions for the radial component form a surface, whose normal shares the direction

of the axial impulse and the laser beam. The orientation of the debris object cannot be defined exactly which means that the direction of the radial components cannot be foreseen and thus could be beneficent or hindering. The variations of the resulting orbit will be discussed in section 5.3.

But independent from the question if the radial impulse is helpful or not, it makes the orbit determination difficult: If $\xi = 0$, the only impulse generated would be directly in line with the laser beam, whose direction is known. Thus if η_j is known, the orbit change could be calculated exactly. Then, before the next pulse is sent, the laser could be readjusted accordingly. However, even if the exact value of the radial impulse is known, there is currently no method to determine in which direction it is actually going. Thus, if no additional tracking is undertaken, the debris object could exit the laser beam and render the majority of the engagement useless. If the debris object is tracked during the engagement, referred to as hyperfine tracking [16], then ξ can be used to determine the minimum time between two measurements in order to keep the debris object in the laser beam diameter. Generally speaking a high value of ξ makes the entire engagement and its results far less projectable and lets the results be especially fickle.

While comparing different values for η_j and ξ the questions arises if a higher η_j is worth a slight increase in ξ and thus a relatively high perpendicular thrust. In order to answer this question the influence of a specific thrust vector on the orbit has to be evaluated.

5.2.1. Orbital effects

Accurately estimating the lifetime of a single debris object can be done using the DRAMA 2.0 software of the ESA [12] and involves complex calculations using a variety of parameters. In the following calculations, as done in the CLEANSPACE project, it is assumed that the perigee height h_p is the only orbit parameter of interest. The goal of the impulse transfer is lowering the perigee so far into the atmosphere, that the debris object either reenters directly or within a few orbits. This is a drastic simplification, if the apogee is raised while lowering the perigee the lifetime might actually increase. Yet in the following section only the lowering of the perigee is considered, since if the goal of lowering the debris object into dense area of the atmosphere succeeds the debris object will quickly reenter the atmosphere.

5.3. Axial vs. radial impulse

In order to analyze if a certain thrust vector is beneficent or not, the impulse vector is split into axial and radial components. The terms are defined relative to the direction vector of the incoming laser beam. The parts of the thrust vector that are parallel to the laser beam are considered axial, while any thrust in an orthogonal direction is considered radial.

For clarification: In the following examples the laser beam is always parallel to the z-axis, thus the z-components of $\boldsymbol{p}$ are the axial part. The x and y components are combined so that the radial component is their total length. The relationships are also described in equations 5.5 and 5.6.

$$\boldsymbol{p}_{axial} = p_z \tag{5.5}$$

$$\boldsymbol{p}_{radial} = \sqrt{p_x^2 + p_y^2} \tag{5.6}$$

The lack of distinction between the impulse components in the x and y direction comes from considerations regarding which components are controllable. While the z-axis is defined by the di-

rection of the laser and thus is dependent on the engagement constellation, the radial components are heavily influenced by the orientation of the debris object, a parameter that cannot be completely ascertained or influenced. So, even though in some cases the radial components could help the deorbit process, in others they could undo the entire process and are thus considered unwelcome.

The following parameter studies will focus on minimizing the radial component and will only consider the axial component as valid contribution to the deorbit process. But since it will not be possible to completely eradicate radial elements, at this point it will be investigated up to what ratio the maneuver will stay beneficent. This depends on the exact configuration regarding orbit and laser station and their position relative to each other. Since presenting every possible configuration would not be helpful, at this point only two exemplary cases shall be presented.

For this analysis a single pulse will be considered. The question posed is: Assuming the worst case, up until what thrust ratio does the impulse generated by the laser pulse still lower the perigee. The following simplifications/assumptions are made:

- $m_{Debris} = 0.135\,kg$.
- Reduction of orbit to 2-D.
- Impulse is transferred when the debris object is directly above station.
- No effects on orbit except gravity and laser pulse.
- For gravitational purposes earth is assumed to be a point mass with $\mu = 398600\frac{km^3}{s^2}$.
- A single pulse transfers a total of $0.0065Ns$, which is approximately the value calculated during the verification cases in section 4.6.
- The pulse is transferred when the debris object is exactly above the laser station.

The Δv created by the impulse is simply calculated using mass and impulse as shown in equation 5.7.

$$\Delta \boldsymbol{v} = \frac{\Delta \boldsymbol{p}}{m_{debris}} \tag{5.7}$$

The previous velocity is simply the velocity of the circular orbit with $r = 7270km$, or the appropriate apogee or perigee velocities, if an elliptical orbit is being considered. If the position and the velocity of the object are known, the Keplerian elements can be calculated using the equations 5.8 through 5.11 taken from [48].

First the eccentricity e is calculated:

$$e = |\boldsymbol{e}| = |\frac{(v^2 - \frac{\mu}{r})\boldsymbol{r} - (\boldsymbol{r} \cdot \boldsymbol{v})\boldsymbol{v}}{\mu}| \tag{5.8}$$

Before the semi-major axis a can be calculated, the vis-viva energy E has to be determined:

$$E = \frac{v^2}{2} - \frac{\mu}{r} \tag{5.9}$$

Using the vis-viva energy the new semi-major axis can be calculated.

$$a = -\frac{\mu}{2E} \tag{5.10}$$

And finally the new perigee can be determined.

$$r_p = (1 - e)a \tag{5.11}$$

5.3.1. Circular orbit

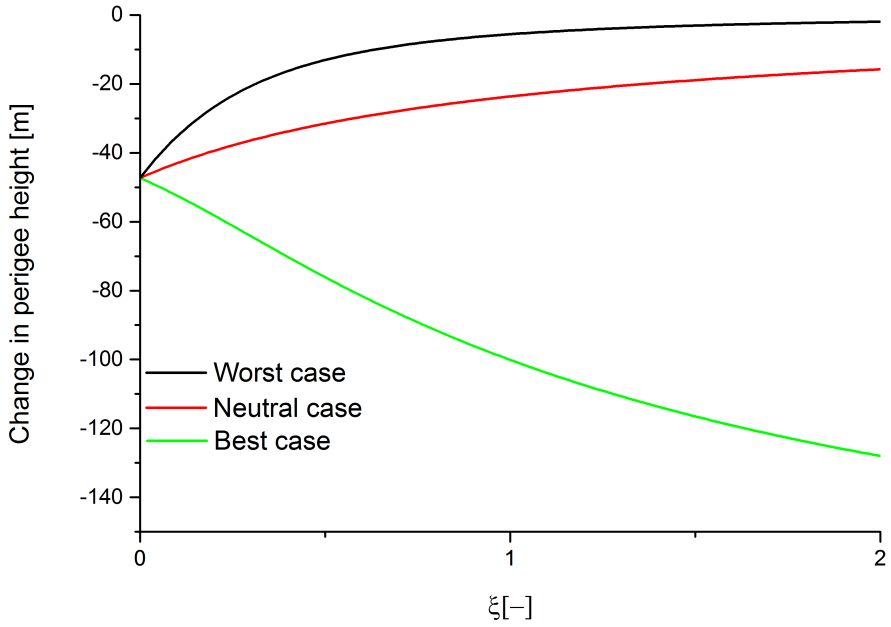

Figure 5.2.: Relationship between the lowering of the perigee h_p and ξ assuming best, neutral and worst directions for radial impulse for a circular orbit and a single pulse.

Worst case

Assuming, in addition to the requirements made above, that the radial component of the impulse shares a direction with the current velocity, figure 5.2 shows the amount by which the perigee is lowered with a single pulse. Since a large amount of significant assumptions are made in the creation of this data, the results have to be used with care. The data presented in figure 5.2 seems inefficient, however, this is caused from the choice of a relatively heavy target, a high orbit and the fact, that irradiation directly above the station is far from the most efficient constellation. The largest perigee alteration Δh_p can be achieved while the object rises in elevation.

Best Case

In this case it was assumed that the radial impulse is directed opposite to the orbital velocity and thus helps in lowering the perigee. As can be seen in figure 5.2, this leads to far better results, as expected.

Neutral Case

While simulating engagements with multiple pulses in EXPEDIT it has become apparent that the radial impulses average out close to 0. The Δh_p shown in figure 5.2 are calculated under this assumption, which means the axial impulse was decreased according to the growing ζ but the radial component was not considered in the Δv. As can be expected this yields lower Δh_p for higher ζ, but far better than in section 5.3.1. It should be noted, that the results in the neutral case are not the mean of the best and worst case. This is the result of only showing the change in perigee height. Thus, it is not shown that the worst case also lifts the apogee and thus additionally prolongs the debris objects lifetime.

5.3.2. Elliptical orbit

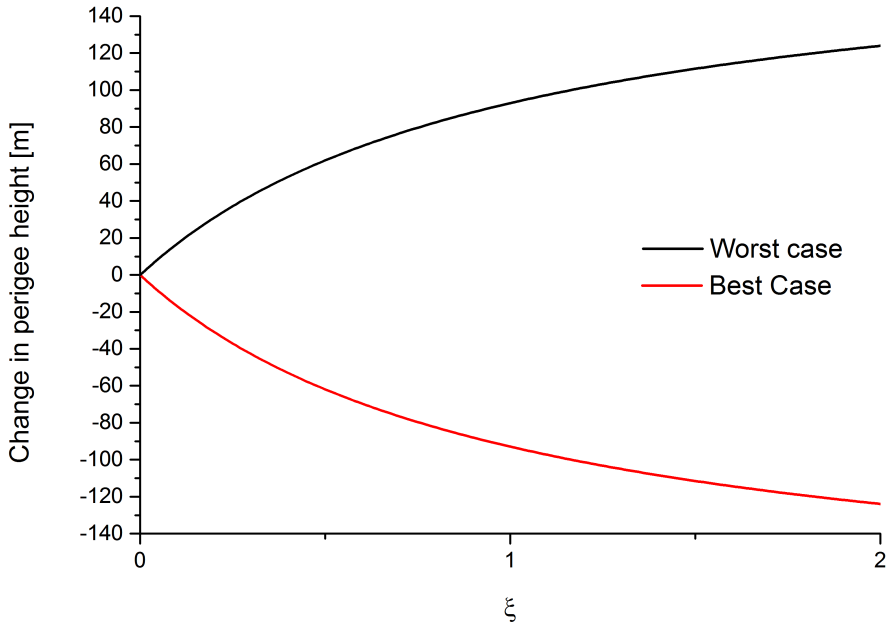

Figure 5.3.: Relationship between the change of the perigee Δh_p and ζ for a single pulse, assuming optimal and worst directions for the radial impulse component. The impulse is transferred at the apogee of a elliptical orbit with $h_p = 800km$ and $h_a = 900km$.

The observations made above are only valid for a circular orbit. Figure 5.3 shows the best and worst case results for an elliptical orbit with $h_p = 800km$ and $h_a = 900km$, assuming the impulse transfer takes place at the apogee. Here, the difference between these cases is much larger, with the worst cases lifting the perigee substantially and thus increasing the debris lifetime. This illustrates the problem with a high ζ: It makes the prediction of the outcome of a pulse in regard to the change in debris lifetime very difficult.

5.4. Shape considerations

While specific shapes and cases will be presented later, for general considerations one has to decide which shapes to consider. In the following parameter studies two shapes are inspected: A thin plate

and a sphere. Hereby the sphere represents a benign case: Rotation effects do not affect the results and as long as the laser irradiance is symmetrical the thrust vector is exactly parallel to the incoming laser beam.

The plate stands as an opposite: The orientation of the plate, and thus rotation effects, have a massive effect on the impulse direction. While it is expected that small variations in key parameters have little effect on spheres, the plates are expected to be far fickler and have worse values for ξ and η_j.

5.5. The modes

EXPEDIT offers the possibility to calculate certain modes in which specified parameters are varied in order to inspect their influence. While each mode has a section in the following pages not every mode is discussed in detail. Every mode is functional within EXPEDIT and can be used but not every one of them yields relevant results for this particular thesis. During the implementation, care was taken to allow for the simple addition of other modes in order to facilitate future additions to the code.

Mode 1: Calculation of one specified case

Mode 2: Variation of repetition rate ν and fluence Φ

Mode 3: As mode 2 but with $P_{laser} = \nu \cdot \Phi = const.$

Mode 4: Variation of initial angular velocity

Mode 5: Variation of the center of hit

Mode 6: Random variation of center of hit and orientation

Mode 7: Variation of orientation

Special focus lies on the modes 1 and 6 which yield the results that are especially interesting in the evaluation in section 5.6.

5.5.1. Default Parameters

If the following sections mention a plate, that plate is always presumed to be made of aluminum. Its dimensions are $0.1m \times 0.1m \times 0.005m$. The spheres used have a radius of 0.05 m and are solid. All debris objects simulated are modelled with a density of $\rho = 2700\frac{kg}{m^3}$. The laser parameters are noted in the captions of the relevant figures. If the laser is modelled by a Gaussian distribution, the Full Width at Half Maximum (FWHM) and the total energy of the pulse are given. If applicable the repetition rate ν will also be provided. All following calculations were performed with the beam method described in section 4.4.2.

5.5.2. Mode 1

This standard mode allows the computation of singular cases, without any automatic variation of parameters. The following cases are of an exemplary nature and were chosen to highlight some results.

Wedge

The Wedge first mentioned in chapter 4.6 shall be discussed in detail here. As mentioned before the expected result is an oscillation, which can be seen in the first part of figure 5.4

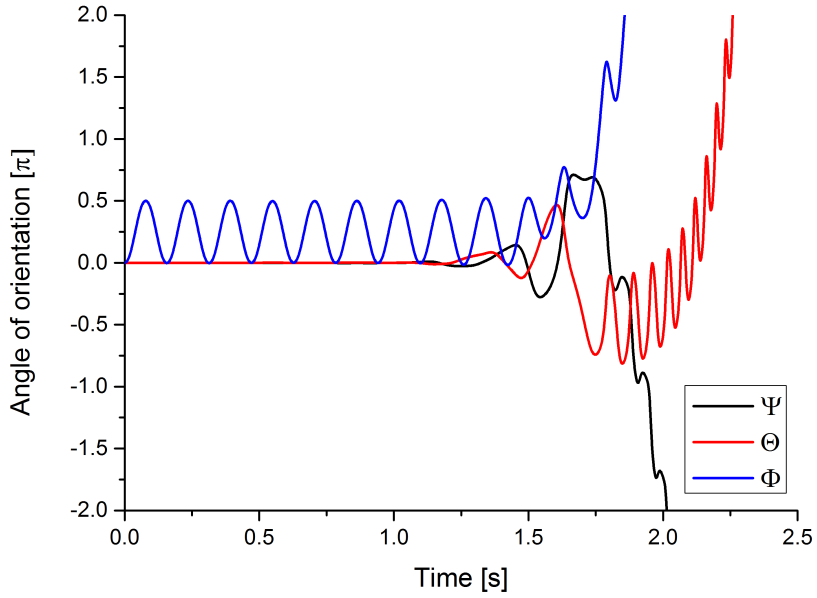

Figure 5.4.: Oscillation of wedge shaped debris. Simulated with a constant fluence $\Phi_L = 25000\frac{J}{m^2}$ and coupling coefficient $c_m = 25\frac{\mu N}{W}$ and the repetition rate $\nu = 200Hz$.

However, in the second half the oscillation is undone and the wedge spins randomly. This behavior is caused by very small angular momenta, which build up on the other axes over time. These disturbances grow slowly at first, but since they tilt the wedge out of the initially symmetrical constellation, they quickly increase. Seen from an analytical point of view, these disturbances should not exist, since the wedge is symmetrical. The answer lies within the method used to calculate the laser matter interaction: The beam method, see section 4.4.2, was used and the discretization causes small errors. These accumulate over time and cause new errors. This escalates quickly into the chaotic behavior seen in figure 5.4. This chaotic behavior occurred during many simulations and will be discussed in-depth in chapter 5.6.

Pliers

Another case study undertaken in order to investigate the behavior of a single debris object was done using a 3-D model of a set of pliers. Astronauts have been known to loose their EVA equipment on various occasions, in one case losing an entire toolbox [47]. The exact shape of the pliers is not as important as the general information, which can be gleamed from the results. Figure 5.5 shows a high-definition version of the model used [14]. All simulations involving the plier were done with the following laser parameters:

- Gaussian profile for the fluence

Figure 5.5.: HD-Model of a set of pliers taken from [14]

- FWHM = 0.1 m
- $E_p \approx 1.1kJ$

- Repetition rate $\nu = 200Hz$
- The $c_m(\Phi_T)$ curve given in figure 5.1

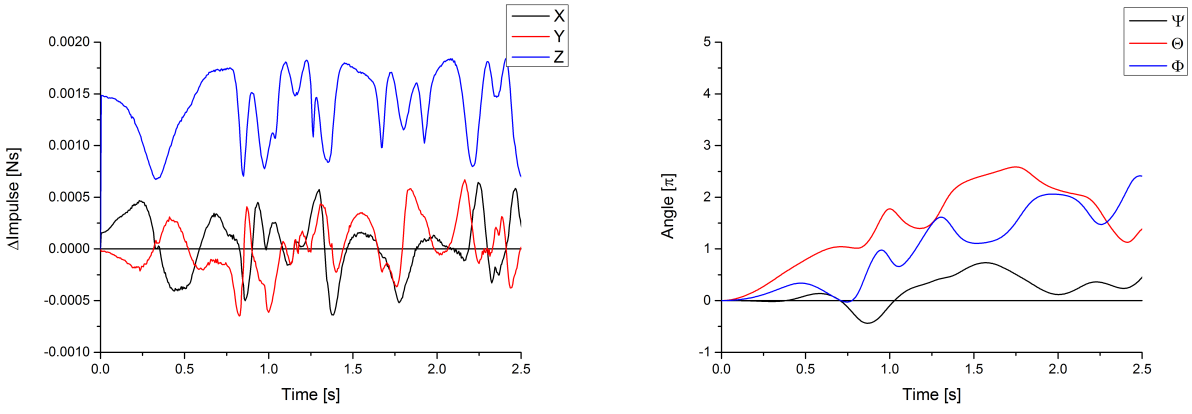

(a) Impulse transfer over time

(b) Orientation over time

Figure 5.6.: Progression of impulse transfer and orientation from default initial orientation

Figure 5.6 shows the impulse transfer and the evolution of the orientation as shown by the three angles already mentioned in chapter 4.4.6. As expected the impulse in z-direction is consistently larger than the impulses in the other directions. The case presented above assumed that the laser beam follows the target. If the target is allowed to move on the basis of the radial impulse components, the results can be seen in figure 5.7. The pliers leave the laser beam quickly and after a

very short time, the laser beam only hits empty space. The amount of time the debris object takes to leave the laser beam is of high interest for hyperfine tracking, which will be discussed in later sections. After the debris leaves the beam no impulse is generated, it would continue spinning but in this case the simulation was cut of after 1.3 s, so the rotation is not shown thereafter.

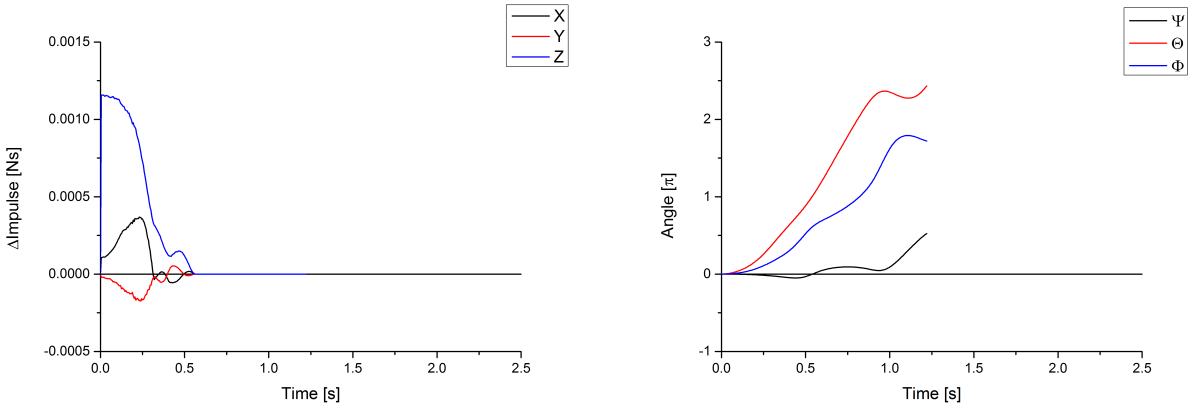

(a) Impulse transfer vs. time

(b) Orientation vs. time

Figure 5.7.: Progression of impulse transfer and orientation from default initial orientation allowing free movement of pliers

The truly interesting results however are the result of slightly tilting the pliers and comparing the results. Figures 5.8 and 5.9 shows the same results if the initial orientation of the pliers is shifted by $\Delta\Theta = \Delta\Phi = 1°$ or $5°$. This results in a total rotation of $1.41°$ and $7.07°$.

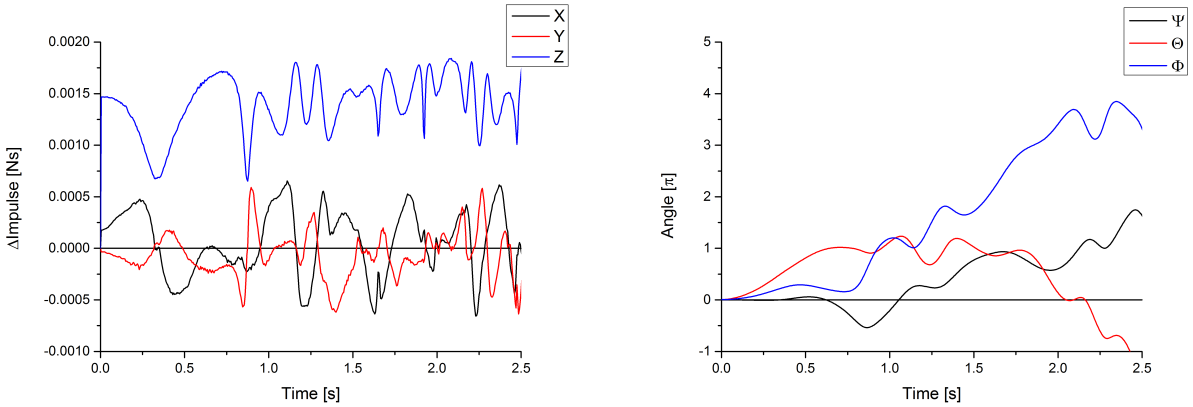

(a) Impulse transfer vs. time

(b) Orientation vs. time

Figure 5.8.: Progression of impulse transfer and orientation. Initial orientation tilted $1.41°$ from default

The results show surprisingly large differences, even if the initial position is changed only slightly. While the results from figure 5.8 are, in some regards, similar to the original results, the curves from figure 5.9 show a completely different behavior. This behavior was found in other calculations as well, small changes to the initial configurations cause massive changes to the behavior over time. So

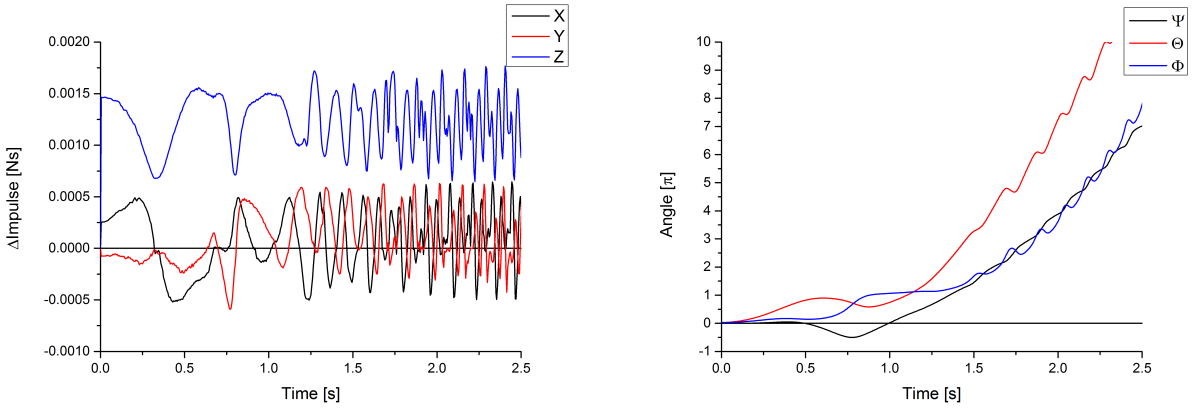

(a) Impulse transfer vs. time

(b) Orientation vs. time

Figure 5.9.: Progression of impulse transfer and orientation. Initial orientation tilted 7.07° from default

while the standard calculations presented here is able to calculate a single case the initial conditions have to be known with great precision in order to produce comparable results.

5.5.3. Mode 2

This mode varies the repetition rate ν and the laser fluence Φ. However, this leads to a large variety of results in a 2D parameter space. The variation of the repetition rate seems to only linearly increase the transferred impulse without any effects connected to the coupling coefficient or other laser ablation effects. The relevant results appear clearer if the total power of the laser system is kept constant, allowing for observations regarding the efficiency of the laser ablation process. This is done in mode 3, see following section, which in some ways is just a reduction of this mode. In favor of those results no results from mode 2 will be presented here.

5.5.4. Mode 3

If this mode is used the repetition rate ν and the fluence Φ are each varied, while keeping the product, and thus the total power constant. Figure 5.10 shows the results of an exemplary calculation. For that calculation the wedge presented in section 4.6.2 was irradiated with a spatially constant laser beam with a constant power of $P_{laser} = 25000J \cdot 200Hz = 5MW$ for 60 seconds. As seen in the calculations made with mode 1 in section 5.5.2, the wedge quickly starts tumbling erratically, allowing for a somewhat random sampling of possible orientations. Figure 5.10(a) shows the total axial impulse achieved over the entire 60 seconds. Since the coupling coefficient is calculated based on the results mentioned at the beginning of this chapter it is no surprise that, at low fluences and high repetition rates, no impulse is achieved, simply because the ablation threshold is not passed. Interestingly, the maximum axial impulse does not seem to coincide with the optimum fluence of at $26000\frac{J}{m^2}$ but at higher fluences, implicating that most of the axial impulses come from surfaces with higher angles of incidence, thus reducing the fluence actually irradiating a surface. Figure 5.10(b) shows the progression of ξ for two cases: First adding the absolutes of the radial impulses and secondly the normal sum, allowing impulses in opposite directions to counteract each other. The radial impulse does seem to counteract itself mostly, yet a small amount of radial impulse is

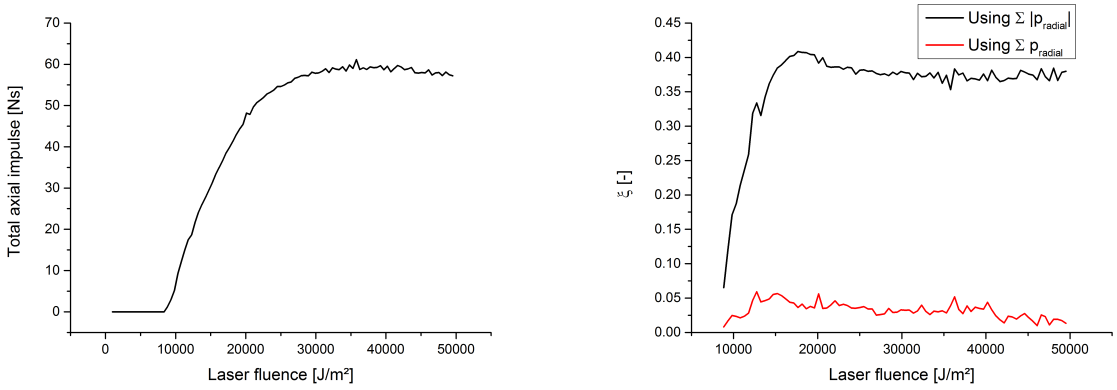

(a) Total axial impulse vs laser fluence

(b) ξ vs. laser fluence 2

Figure 5.10.: Results of parameter study for constant power $P = const = E_p \cdot \nu$ with varying fluence. $c_m(\Phi)$ as given in 5.1.

present even in the second case. The values for ξ, calculated using the absolute sum, reach a maximum far before the fluences reaches Φ_{opt}. It should be noted, that for wedge shaped debris $\xi \approx 0.4$

The results of this parameter study is only valid for the wedge shape used, as seen in section 4.3 the values of ξ for plates and sphere behave differently.

5.5.5. Mode 4

This mode allows the examination of the behavior depending on the initial angular velocity. While some cases were simulated with this mode, they only confirmed that an initial rotation may not be stabilized but can actually be amplified by the ablation. As above the prediction of the final impulse vector is highly sensitive to the exact direction and amount of the angular impulse, an observation, which highlights the need of different methods to investigate the impulse transfer, which are provided by mode 6.

5.5.6. Mode 5

This mode varies the center of hit, which means that it varies the amount by which the center of the laser beam misses the center of mass of the debris object. Since uncertainties in the orbit propagation and atmospheric turbulences will create errors in that regard, the effects have to be analyzed. It appears unlikely, that these errors can be eliminated completely; especially the atmospheric turbulences cannot be completely compensated. Assuming a Gaussian spatial distribution for the fluence of the laser beam, this will lead to asymmetrical forces on the debris object, even if it is an optimally aligned plate. Since the plate is aligned so that its normal is parallel to the beam, the first impulse will be along laser beam direction. However, the asymmetry of the forces introduces a torque, which leads to the plate tilting. This introduces radial impulses in the following pulses and thus movement in the radial direction, i.e., not along the laser beam but out of it. Mode 5 allows the estimation of the time the debris objects takes to leave the laser beam and thus allows the user to estimate the minimum frequency of the hyperfine tracking. For almost any shapes except specific cases the debris objects will eventually be pushed completely out of the laser beam.

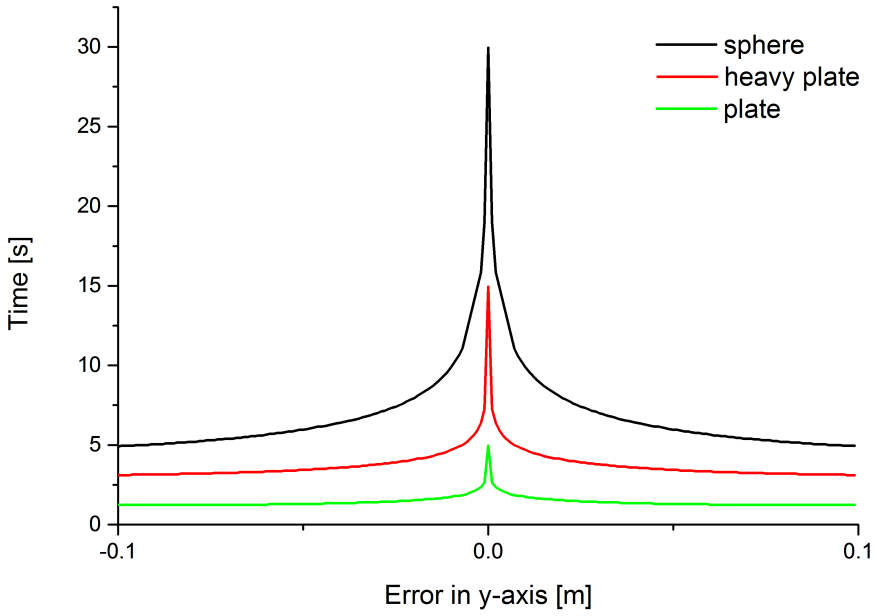

Figure 5.11.: Relationship of time until the debris object moves one beam diameter radially and the distance of the laser beam from the center of mass of the debris object, calculated using mode 5

In figure 5.11, a sphere and a plate are compared in regard to the time they take to move one beam diameter, given a certain displacement between the actual center of hit of the laser beam and the center of mass of the debris object. For this simulation only an error in the y-axis was considered, while 2D simulations were made as well, they do not offer new insights. These results were calculated using a 20 Hz repetition rate and a Gaussian distribution with FWHM=0.5m and $E_p \approx 7.1kJ$. In order to compare the shape effects, the plate was simulated twice, once with the mass of the sphere, otherwise the lower mass of the plate would cause it move far quicker. The two cases show different behavior: While initially the plate only experiences axial impulse the asymmetry causes the plate to spin and thus radial impulse is created by the subsequent laser pulses. If the sphere is irradiated asymmetrically radial impulses are created instantly.

In both cases it was expected, that if the beam hits the center of the shape directly, no radial movement should occur. However, as mentioned before, the discretization of the laser beam causes small errors which build up exponentially and finally cause the debris to move radially even if irradiated perfectly. While this error does not occur in analytical approaches, it underlines the difficulty of prediction, mentioned in section 5.5.2 and will be further explored in section 5.6. Generally the sphere is far more resistant to this type of error. While the higher mass in comparison to a plate is a factor it does not cause all the difference.

5.5.7. Mode 6 | Random

As noted in the previous sections, especially section 5.5.2, individual calculations appear to be highly dependent on the starting conditions. The ramifications of this shall be discussed in chapter 5.6 but motivated by prelimary analysis of the Mode 1 calculations, this mode was implemented in

order to allow a randomized calculation of many individual pulses. The value,being subjected to random variations were chosen based on the effects expected in realistic conditions. The two most important parameters that cannot be completely controlled are the orientation of the debris object and the error by which the center of the laser beam misses the center of mass of the debris object. This results in a calculation, which randomly samples 6 DOF: 3 angles describing the orientation and the three-dimensional position of the actual center of hit of the laser beam.

In order to sample as large variety of possible configurations each of the following results were generated by calculating the effects of 500,000 single pulses. The results of various configurations are presented in the following paragraphs.

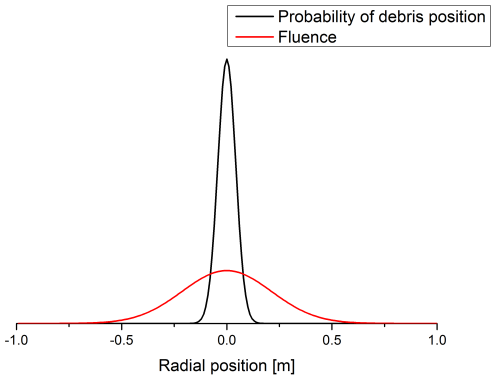

Figure 5.12.: Spatial distribution of laser fluence and probability of debris position. FWHM for Φ is 0.5 m, for debris position probability the FWHM is 0.1 m

The laser beam was simulated using a Gaussian distribution with a full width half maximum (FWHM) of 0.5 m. The distribution of the fluence from the laser beam and the probability function of the debris object position are shown in figure 5.12. As can be seen there, the debris object will mostly stay close to the center of the beam, but still be subject to variation of the fluence.

Three shapes were selected for primary studies: A quadratic plate with a side length of 10 cm, a sphere with 10 cm diameter and finally the pliers presented in section 5.5.2, whose longest dimension is about 12 cm. The sphere was selected as the best possible target. Variations of orientation do not matter in that case and it was expected that the variations caused by the asymmetric variation of the fluence would be small as well. The plate is considered the opposite: It is highly susceptible to variation of orientation and thus very unstable results were expected. In lieu of a 3D scan of a true space debris object, the pliers were selected as a random element. Regarding random elements, the possible future use of 3D scans of collision fragments will be discussed in chapter 7.

For these three shapes the average and maximum axial impulses are shown in figure 5.13. The average impulse transfer was largest, when a sphere was irradiated, but if the optimal constellation (the result with the highest impulse transfer) is examined, the plate yields significantly higher results. The comparison is somewhat inadequate for the set of pliers, since even though its main dimension shares the size of the plate and sphere, it has far less surface area, so less impulse was generated.

In figure 5.14 ξ and η_j for plate and the set of pliers are shown, calculated on the same basis as the

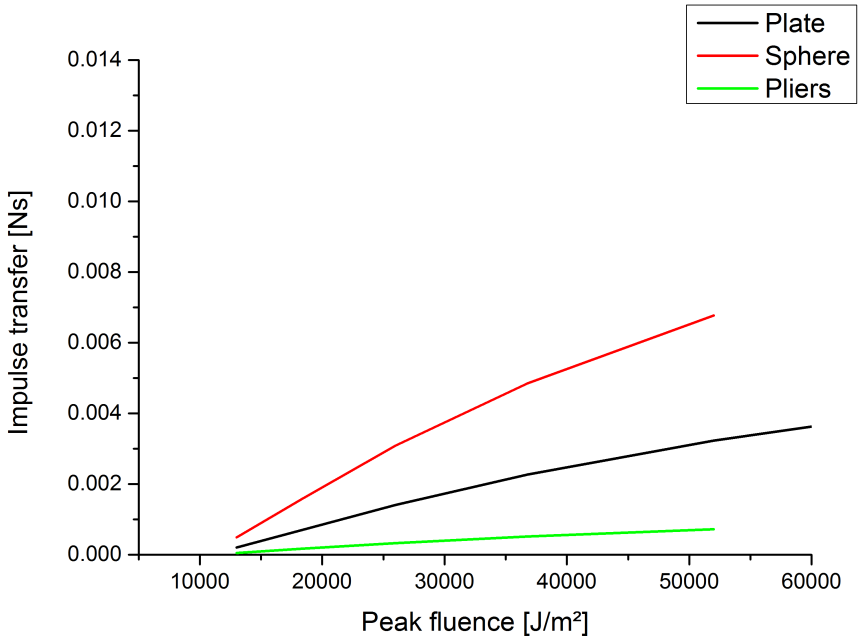

(a) Average axial impulse transfer

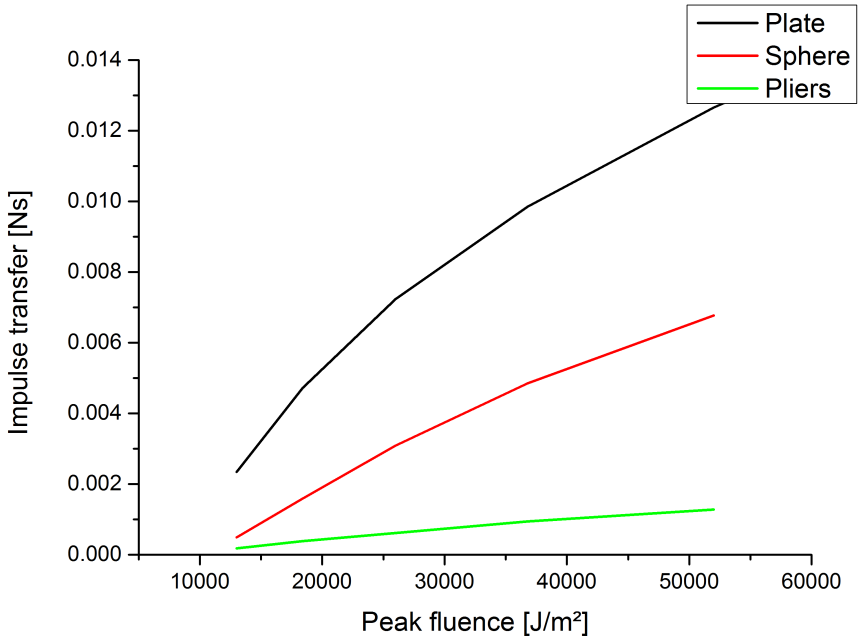

(b) Maximum axial impulse transfer

Figure 5.13.: Axial impulse transfer for different target shapes - calculated using mode 6

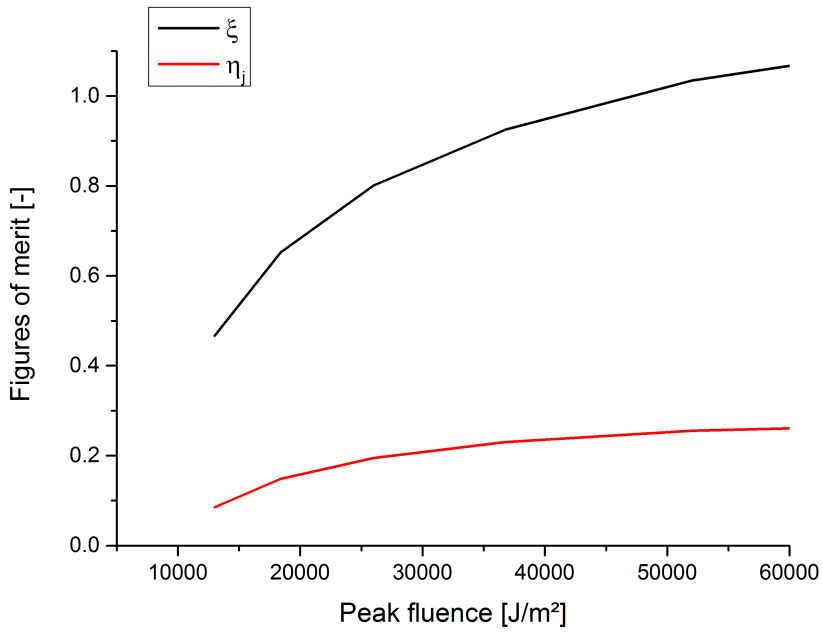

(a) Plate

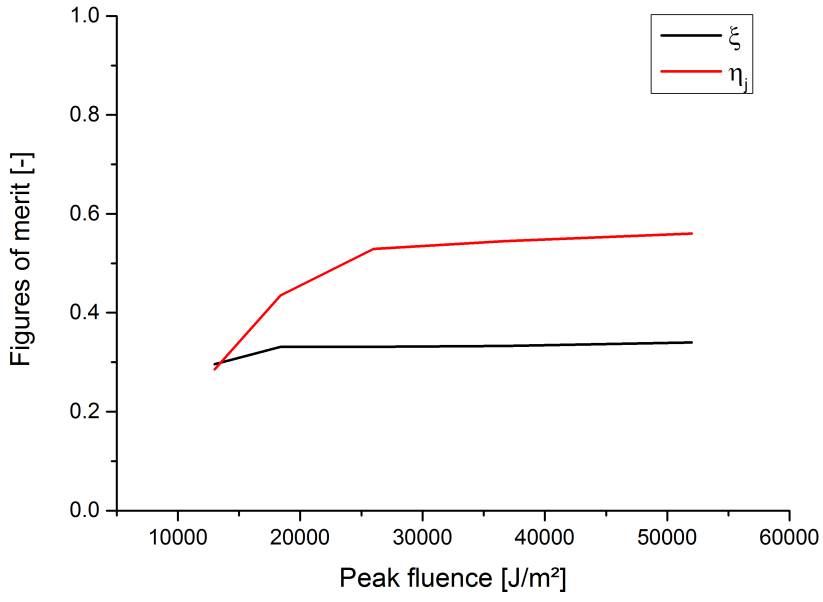

(b) Pliers

Figure 5.14.: ξ and η_j for different shapes

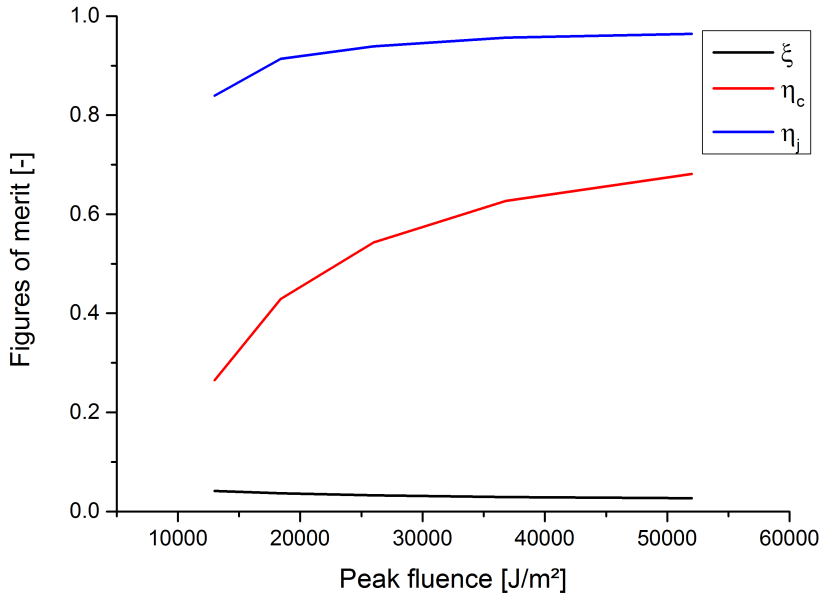

Figure 5.15.: ξ, η_j and η_c for a sphere

results shown in figure 5.13. Figure 5.15 shows the same for a sphere with the addition of η_c. As a reference case for η_c a plate with the surface area of the spheres' cross section was used. This leads to much lower value for η_c than for η_j. Overall, the sphere offers the most benign results. Even at low fluences the axial impulse does not differ significantly from its optimal value at the given fluence, and at higher fluences the average axial impulse is virtually identical to the optimum value. Additionally, the radial impulse generated is negligible and ξ sinks even further at higher fluences. There is no reason to suspect an abundance of spherical debris, apart from the NaK-spheres mentioned in 2. Most seem to be somewhat plate shaped which is problematic, since the results for plates are precarious. At low fluences the radial impulse averages at $\approx 45\%$ of the axial components and at higher fluences it is even larger than the axial part. These high radial components are created by the variation of the coupling coefficent discussed in chapter 3.

In order to illustrate the differences to the analytical results available using Liedahls method, described in section 3.5, the same calculations as above were undertaken with EXPEDIT under the restraints associated with the analytical method: A spatially constant fluence distribution within the laser beam and a constant coupling coefficient of 25 $\frac{\mu N}{W}$, regardless of incidence fluence. In figure 5.16 the results for the plate described above, for both methods are compared in order to highlight the differences that result from the different methods. While all following results were calculated with Expedit, the cases using the assumptions discussed above will be described as the "analytic" results.

As can be seen, any variation of ξ or η_j was solely caused by the varying coupling coefficient, underlining the importance of finding accurate models and methods to predict the coupling coefficient. However, these results offer an interesting possibility. ξ seems to stay constant for a shape, so that different possible shapes could be classified using ξ. For a sphere, in this case ξ would vanish since,

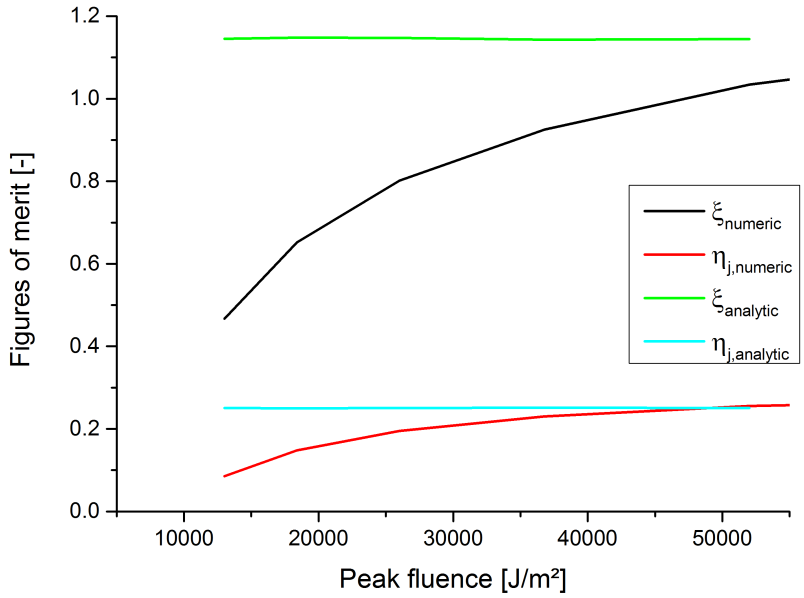

Figure 5.16.: Comparison of η_j and ξ for a plate with a constant c_m (analytic) and a spatially variable $c_m(\Phi_T)$ (numeric)

if the fluence is spatially constant, the radial impulses counteract each other, thus only the axial impulses remains.

Simply assuming the optimal coupling coefficient, however, still does not offer a fair comparison, so in figure 5.17 the same calculation is shown, in this case, the coupling coefficient, while still spatially constant, was assumed to be the value usually associated with the relevant peak fluence.

In this case very high fluences have been included into the calculation in order to examine the behavior in those regimes. It can be seen, that the analytical method leads to overestimation of η_j and ξ in the lower fluence cases. For fluences higher than $2 \cdot \Phi_{opt}$ ($\Phi_{opt} \approx 26000 \frac{J}{m^2}$ in this case) the analytical method underestimates η_j, but not critically so.

For ξ the behavior is initially similar: First massively overestimated, at ca. $3 \cdot \Phi_{opt}$ the sides swap and the analytical method underestimates it and thus the radial components caused by the laser ablation.

This behavior is caused by the curve of the coupling coefficient. At low Φ_L, only cases with a low angle of incidence have a Φ_T above the threshold, and thus if any impulse is generated, it is mostly axial impulse. At high fluences, even orientations with a high angle of incidence can achieve ablation and thus caused a high amount of radial impulse. This is reinforced by the fact, that if Φ_F is high above the optimum fluence, then the local fluence at certain incidence angles, can be very close to the optimum fluence and thus create additional radial impulse. This leads to the underestimation of ξ by the analytical method that can be seen in figure 5.17.

While the cases presented here could be calculated analytically using a given function for the coupling coefficient, the observations on the impact of the coupling coefficient made in the last pages remain valid for complex geometries even though no direct comparison can be made.

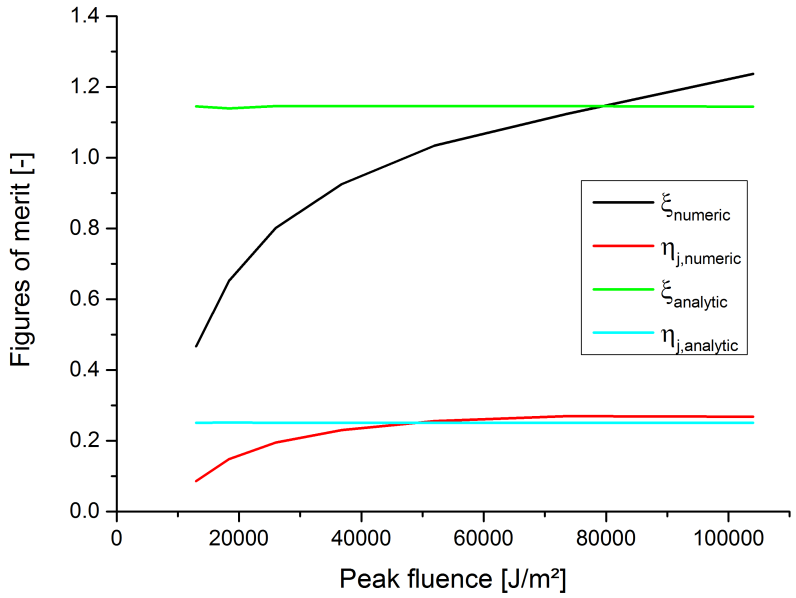

Figure 5.17.: Comparison of η_j and ξ for a plate with spatially constant $c_m(\Phi_L)$ (analytic) and a spatially variable $c_m(\Phi_T)$ (numeric)

5.5.8. Mode 7

As mentioned above, this mode varies the orientation of the object and thus allows the user to examine similar effects as in mode 6 but without the interference of errors in aiming. Since these results offer no new insights not discussed in the paragraph above, they will not be discussed in detail here.

5.6. Conclusion

Many of the simulations presented in chapter 5 appear to be very sensitive in regard to the initial conditions. Especially in section 5.5.2 it was apparent that small changes in the initial orientation cause very different future progressions. This leads us to chaos theory, a field of study which was started by the famous question: "Does the Flap of a Butterfly's wings in Brazil Set Off a Tornado in Texas?" posed in the article of the same name by [29].

While Lorenz' observations were made in regard to weather systems, they hold true for many other fields as well: Usually, if a system is deterministic it can be simulated and its future behavior predicted. But some systems have an extremely high sensitivity to initial conditions: A small change in initial conditions, i.e., a flap of a butterfly, can lead to monumental changes, i.e., a tornado, in the behavior of the system.

Thus, it becomes imperative to measure the initial state as exact as possible, which comes with the problems described in chapter 2. But the list of factors that influence the impulse transfer is long:

- Orbit parameters

- Debris parameters
  - Shape
  - Mass
  - Inertia tensor
  - Angular velocity
  - Material
- Laser parameters
  - Spatial distribution of fluence
  - Temporal distribution of fluence within the pulse
  - Aiming error
  - Wavelength

Many of these influences could be considered fractal: While correcting one error, other, smaller, errors appear, which have to be eliminated as well. For example, in order to model the error caused in the laser beam aiming, an accurate model of the atmosphere would be needed, which comes with a new list of dependencies, including the aforementioned butterflies. Additionally, many of the parameters in the list above are connected: Knowledge of shape, mass, inertia tensor, angular velocity and angular momentum all depend on knowledge on the others, so any error in one measurement exerts influence on others, causing more errors. While it might be possible to measure some parameters with great precision, others ,e.g., the exact shape, can not be measured without great effort.

It quickly becomes apparent that the case studies presented in section 5.5.2 are not of much use and should not be used for any but the most generic of observations.

As one way of dealing with this chaos was implemented and discussed in section 5.5.7: By changing the initial conditions randomly and averaging the results, data can be obtained that can be used to actually learn something about the system in question. This method does not allow the exact prediction of every engagement by a laser system, but over large sample sizes it can predict the overall efficiency. In this mode, EXPEDIT is using Monte Carlo methods. Luckily, from a statistical point of view, the space debris population is quite large and thus the use of average values can be seen as valid. Some methods that could possibly improve the effectiveness of the laser engagement will be presented in chapter 7.

6 Summary

In order to deorbit non-cooperative space debris, laser ablation is being investigated as a possible propulsion source, which offers the unique advantage of being able to interact with space debris over long distances, i.e., from the surface of the earth. Very short, very powerful pulses heat up a thin surface layer to extremely high temperatures and cause the surface layer of the target to be expelled from the original debris object, which creates thrust by the same principle as classic rocket engines. Ideally the orbit of the debris object is lowered sufficiently for the debris object to directly reenter the atmosphere. However, the direction of the local thrust vector is independent from the angle of incidence of the laser beam but instead perpendicular to the local surface. This results in large uncertainties for the final impulse vector caused by the laser engagement.

An examination of possible shapes for space debris was undertaken in order to have an overview of shapes that have to be simulated. Most debris fragments originated from on-orbit explosions or collisions. Thus, the results of ground based HVI-tests are valuable resources. However, the only experiment using a full sized satellite with modern materials is the DebriSat series of experiments, whose data is not available yet. Fragments from older tests or recent tests using microsatellites suggest that plates or flat ellipsoids are common shapes for debris.

The efficiency of the laser-matter interaction is measured by the coupling coefficient c_m, which is defined as the ratio from imparted impulse to pulse energy. The exact value of c_m is dependent on many parameters, including the fluence of the laser beam. This makes it difficult to calculate the the exact impulse analytically without assuming very simple shapes and making many other simplifications.

The primary goal of this thesis was the development and implementation of a tool capable of simulating laser matter-interaction for complex geometries, especially regarding the impulse caused. Special consideration was given to effects caused by shape and orientation of the debris object. The tool EXPEDIT was written in C++ and used to conduct a series of parameter studies. Depending on the complexity of the case being simulated, different methods were used to calculate the impact of a laser pulse. For simple shapes with spatially constant laser irradiation, simple methods similar to the analytical methods were implemented, while more complex shapes require the discretization of the laser beam or the target geometry, in order to correctly simulate varying fluence and coupling coefficients and other effects such as self-shadowing.

Two methods for reading geometric shapes were implemented: an XML-file allows the quick creation of simple geometries from predetermined shapes. For complex shapes, a method for reading the STL-file format was created, which can describe complex geometries. In order to simulate entire engagements, methods for simulating the motion between two pulses were implemented, special

care was taken to calculate the rotational motion, since the orientation of the debris object has a major influence on the resulting impulse.

While the first scenarios were simulated, it became apparent that the progression of the parameters of the laser-space debris interaction were extremely dependent from the initial conditions and often produced chaotic results: even small changes in the initial conditions could cause completely different progressions over time. Thus, if the initial conditions are not known with great precision, a single simulation is only valid to a limited extent, i.e., only for a very short span of time which is far too short to accurately simulate engagements that can take several minutes. In order to still gain information that can be used to generally assess possible outcomes, EXPEDIT is able to automatically vary certain input parameters with a series of modes. Six of these modes were implemented and used to examine the laser-debris interaction.

Two figures of merit, ξ and η_j, were introduced in order to describe the efficiency of laser-debris interaction:

η_j: Represents the ratio of the axial impulse in an optimal constellation vs. the expected average.

ξ: Represents the ratio of radial to axial impulse.

The separation into radial and axial impulse, as seen relative to the incoming laser beam, was done in order to separate the impulse into the predictable axial component and the unpredictable radial component. Since the axial component shares a direction with the laser beam, its direction is known, however, even if the amount of the radial component can be estimated, the exact direction cannot be ascertained. While radial impulse can produce positive effects, i.e., further lowering the orbit, the opposite holds true as well. In the ideal case $\xi \approx 0$, so that the direction of the generated impulse is controllable. If, as in all but some special cases, radial thrust occurs, no methods exist to control or predict if the radial impulse occurring will be beneficial or not. EXPEDIT can be used to calculate average values for ξ and η_j for a given shape and initial conditions by randomly varying the exact center of the laser beam and the orientation of the space debris for a large number of samples. These variations are also to be expected for the actual application, since both parameters are not entirely controllable.

ξ and η_j were calculated for sample shapes. Additional 3D data of collision fragments is expected from NASA hyper-velocity impact tests [28] and can be used to calculate ξ and η_j for all typical fragment shapes thus allowing predictions for the average values of the space debris population. It should be noted that the simulations yielded values for ξ and η_j that were worse than expected. For a plate-shaped debris object η_j ranged from 0.1 to 0.3 and ξ from 0.4 to values slightly above 1.

A recalculation of the parameter studies conducted in chapter 5 with different curves for $c_m(\Phi)$ on the basis of different laser parameters, would allow the comparison of the laser parameters in regard to ξ and η. The addition of a variable coupling coefficient to the calculations shown in [25] was useful, since it uncovered a strong dependence of the abovementioned figures of merit to the local fluence Φ_T. Methods for improving the values of ξ and η_j will be discussed in the following chapter 7.

Without optimization the high values of ξ pose difficulties for the laser-debris-removal concept. The higher ξ, the higher the uncertainty with regard to the actual effects of the laser engagement. In comparison, the problems posed by low values for η_j can be overcome by multiple engagements or simply raising the laser power.

7 Future prospects

This chapter will evaluate possible future work in this field of study.

7.1. Use of DebriSat data

The DebrisSat experiments described in section 2.2.2 will, in the course of time, yield 3D scans of representative debris fragments. This offers the possibility to actually simulate fragments within EXPEDIT and thus, to be able to predict the range of values to be expected for ξ and η_j. Depending on the exact results, this could underline the need to optimize the laser-based deorbit-process, see section 7.3.

7.2. Experimental verification

There has been no experimental verification for the results presented in this thesis. This stems from the fact the pulse energies used in the calculation are of considerable magnitude and that laser systems, with that type of pulse energy are rare. In order to irradiate a debris object with a 10cm diameter with a fluence of 3 $\frac{J}{cm^2}$ a pulse energy of $\approx 236J$ is needed, with only few laser systems able to provide that type of energy.

However, during the course of this thesis, a possibility for cooperation with the GSI Helmholtzzentrum für Schwerionenforschung in Darmstadt has appeared, including the use of their laser systems NHELIX and PHELIX. NHELIX offers pulse energies up to 100J for smaller targets while the 1kJ pulse energy of the PHELIX is sufficient to irradiate full-sized targets.

An interesting possibility would be the combination of DebriSat data with this experimental possibility. Using the 3D scans and 3D printers, copies of actual debris fragments could be created and irradiated. Since most of the simulation of the coupling coefficient is done using 1D simulation the simple irradiation of a plate could be used in order to examine the validity of those simulations.

7.3. Optimization

While a low η_j can be overcome by simply "turning up the power", the effect of high ξ is more problematic and methods for optimization should be examined. One promising method would be the use of light curves. As mentioned in chapter 2, light curves show the magnitude of the reflected light of an object over time, be it reflected sunlight or the reflected laser signal if laser ranging is used.

If the debris object is continuously tracked using laser ranging it could be possible to only trigger the pulsed removal laser at the moments at which the reflection from the ranging laser is over a certain threshold. This could increase η_j while decreasing ξ because more impulse is directed axially and less radially. If the debris object is spinning quickly the delay between the two systems could become critical but for debris not spinning exceptionally fast it should be able to eliminate the worst cases and increases η_j as well as decrease ξ.

If passive optical tracking is used, the reflection cannot be used to increase the axial component, but instead be used to direct the radial component. If the debris is moving towards, as seen from the ground, the setting or rising sun and the light curve is at a high value, it would reasonable to expect the radial components to point towards the sun and thus directly decrease the orbital velocity and energy. If the constellation is reversed and the debris is moving away from the sun, a pulse at the darkest point of the light curve would have similar effects. This would increase the efficiency of the operation, even if only applicable in certain cases. Even if the constellation is not as perfect as assumed, the information gained from further analysis of the light curve could be very valuable even if only used to eliminate the worst constellations.

However, these ideas would have to be examined in order to appraise them. A simulation combining parts of this thesis with an orbit simulation and methods to approximate the light curves, could shed light onto the efficiency of the proposed methods and if further effort should be made to investigate these possibilities.

Bibliography

[1] Anisimov, S., Kapeliovich, B., Perel'Man, T., 1974. Electron emission from metal surfaces exposed to ultrashort laser pulses. Zh. Eksp. Teor. Fiz 66 (776), 375–7.

[2] Bai, X., et al., 2009. High-resolution three-dimensional imaging of spinning space debris. IEEE Transactions on Geoscience and Remote Sensing 47 (7), 2352–2362.

[3] Bäuerle, D., 2000. Laser processing and chemistry, 3rd Edition. Vol. 3. Springer, Berlin.

[4] Bekey, I., 1997. Project ORION: orbital debris removal using ground-based sensors and lasers. In: Second European Conference on Space Debris. Vol. 393. p. 699.

[5] Buss, S. R., 2000. Accurate and Efficient Simulation of Rigid-Body Rotations. Journal of Computational Physics 164 (2), 377–406.

[6] Carvalhaes, C., Suppes, P., 2008. Approximations for the period of the simple pendulum based on the arithmetic-geometric mean. American Journal of Physics 76 (12), 1150–1154.

[7] Crabtree, C., et al., 2013. Formation and dynamics of an artificial ring of dust for active orbital debris removal. In: Aerospace Conference, 2013 IEEE. IEEE, pp. 1–12.

[8] Eberly, D. H., 2001. 3D Game Engine Design. A Practical Approach to Real Time Computer Graphics. San Francisco: Morgan Kaufmann Publishers, Inc.

[9] Eckel, H.-A., et al., 2014. Overview of Laser Ablation Micropropulsion Research Activities at DLR Stuttgart. In: Presentation at the International Symposium on High Power Laser Ablation and Beamed Energy Propulsion, Santa Fe, NM.

[10] Einstein, A., 1917. Zur Quantentheorie der Strahlung. Physikalische Zeitschrift 18, 121–128.

[11] ESA, 2012. MASTER (Meteoroid and Space Debris Terrestrial Environment Reference) website. `http://www.master-model.de/index.html`, accessed: 09.01.2015.

[12] ESA, n.d. space debris user portal. `https://sdup.esoc.esa.int/web/csdtf/home`, accessed: 09.01.2015.

[13] Esmiller, B., et al., 2014. Space debris removal by ground-based lasers: main conclusions of the European project CLEANSPACE. Applied optics 53 (31), I45–I54.

[14] GrabCAD, 2014. Database of cad models. `http://www.grabcad.com`, accessed: 15.10.2014.

[15] Graf, T., 2009. Laser Grundlagen der Laserstrahlquellen, 1st Edition. Vieweg-Teubner Verlag, Wiesbaden.

[16] Haag, H., Karg, S., Scharring, S., 2013. Report on Laser/matter interaction. Tech. rep., CLEANSPACE.

[17] Hanada, T., et al., 2009. Outcome of recent satellite impact experiments. Advances in Space Research 44 (5), 558–567.

[18] Hoerz, F., et al., 1995. Natural and orbital debris particles on LDEF's trailing and forward-facing surfaces. In: LDEF: 69 Months in Space. Third Post-Retrieval Symposium. Vol. 1. pp. 415–429.

[19] Johnson, N. L., et al., 2008. The characteristics and consequences of the break-up of the Fengyun-1C spacecraft. Acta Astronautica 63 (1), 128–135.

[20] Kessler, D. J., Cour-Palais, B. G., 1978. Collision frequency of artificial satellites: The creation of a debris belt. Journal of Geophysical Research: Space Physics (1978–2012) 83 (A6), 2637–2646.

[21] Kessler, D. J., Johnson, N. L., Liou, J., Matney, M., 2010. The Kessler Syndrome: Implications to Future Space operations. Advances in the Astronautical Sciences 137 (8).

[22] Klinkrad, H., 2006. Space Debris: Models and Risk Analysis. Springer Praxis Books.

[23] Krisko, P., 2014. The New NASA Orbital Debris Engineering Model ORDEM 3.0. Tech. Rep. JSC-CN-31453, NASA.

[24] Krisko, P., Horstman, M., Fudge, M., 2008. SOCIT4 collisional-breakup test data analysis: With shape and materials characterization. Advances in Space Research 41 (7), 1138–1146.

[25] Liedahl, D., et al., 2013. Pulsed Laser Interactions with Space Debris: Target Shape Effects. Advances in Space Research 52 (5), 895–915.

[26] Liedahl, D. A., Libby, S. B., Rubenchik, A., 2010. Momentum Transfer by Laser Ablation of Irregularly Shaped Space Debris. In: INTERNATIONAL SYMPOSIUM ON HIGH POWER LASER ABLATION 2010. AIP Publishing, pp. 772–779.

[27] Liou, J.-C., September 2014. personal communication.

[28] Liou, J.-C., et al., 2013. DebriSat-A Planned Laboratory-Based Satellite Impact Experiment. Tech. Rep. JSC-CN-27655, NASA.

[29] Lorenz, E. N. (Ed.), 1972. Predictability: does the flap of a butterfly's wing in Brazil set off a tornado in Texas? American Association for the Advancement of Science.

[30] Lu, Y.-F., Tao, Z.-B., Hong, M.-H., 1999. Characteristics of excimer laser induced plasma from an aluminum target by spectroscopic study. Japanese Journal of Applied Physics 38 (5R), 2958.

[31] Nishida, S.-I., et al., 2009. Space debris removal system using a small satellite. Acta Astronautica 65 (1), 95–102.

[32] Nishimoto, D. L., et al., 2001. Spectroscopic observations of space objects and phenomena using Spica and Kala at AMOS. In: International Symposium on Optical Science and Technology. Proc. SPIE 4490, pp. 212–220.

[33] Opiela, J. N., 2009. A study of the material density distribution of space debris. Advances in Space Research 43 (7), 1058–1064.

[34] Phipps, C. R., 2014. A laser-optical system to re-enter or lower low Earth orbit space debris. Acta Astronautica 93, 418–429.

[35] Phipps, C. R., et al., 2010. Review: Laser-Ablation Propulsion. Journal of Propulsion and Power 26 (4), 609–637.

[36] Phipps, C. R., et al., 2012. Removing orbital debris with lasers. Advances in Space Research 49 (9), 1283–1300.

[37] Phipps, C. R. e. a., 1996. ORION: Clearing near-Earth space debris using a 20-kW, 530-nm, Earth-based, repetitively pulsed laser. Laser and Particle Beams 14 (01), 1–44.

[38] Povarnitsyn, M., et al., 2012. Dynamics of thin metal foils irradiated by moderate-contrast high-intensity laser beams. Physics of Plasmas 19, 023110.

[39] Praly, N., et al., 2012. Study on the eddy current damping of the spin dynamics of space debris from the Ariane launcher upper stages. Acta Astronautica 76, 145–153.

[40] Sato, T., 1999. Shape estimation of space debris using single-range Doppler interferometry. IEEE Transactions on Geoscience and Remote Sensing 37 (2), 1000–1005.

[41] Sato, T., et al., 1994. Shape of Space Debris as Estimated from Radar Cross Section Variations. Journal of Spacecraft and Rockets 31 (4), 665–670.

[42] Scharring, S., 2013. Impulsanalyse beim luftatmenden gepulsten laser-thermischen Antrieb mit parabolischer Reflektordüse für Raumfahrtanwendungen. Ph.D. thesis, University of Stuttgart.

[43] Schawlow, A. L., Townes, C. H., 1958. Infrared and Optical Masers. Physical Review 112 (6), 1940.

[44] Schulz, W., Ludwig, R., 1990. Begriffe, Größen und Formelzeichen der Flugmechanik–Bewegung des Luftfahrzeugs gegenüber der Luft. DIN 9300 Teil 1.

[45] Sean, T., 2014. CelesTrak. `http://www.celestrak.com`, accessed: 05.01.2015.

[46] Shuangyan, S., Xing, J., Hao, C., 2014. Cleaning space debris with a space-based laser system. Chinese Journal of Aeronautics 27 (4), 805–811.

[47] Tobin, K., 2008. Astronaut loses tool bag during spacewalk. `http://edition.cnn.com/2008/TECH/space/11/18/endeavour.spacewalk/index.html?eref=time_us`, accessed: 05.01.2015.

[48] Vallado, D. A., 2001. Fundamentals of astrodynamics and applications, 12th Edition. Springer.

[49] van Heesch, D., 2015. Doxygen. `http://www.doxygen.org`, accessed: 15.01.2015.

[50] Voelker, U., et al., 2011. Laser-Based Space Debris Monitoring. In: BEAMED ENERGY PROPULSION: Seventh International Symposium. Vol. 1402. AIP Conf. Proc., pp. 354–363.

[51] Wiedemann, C., 2006. Die Modellierung der Natrium-Kaliumtropfen als Beitrag zur orbitalen Objektpopulation. Shaker.

[52] Yanagisawa, T., Kurosaki, H., 2012. Shape and motion estimate of LEO debris using light curves. Advances in Space Research 50 (1), 136–145.

List of Figures

1.1. Historical growth of catalogued objects, from [45] 9

2.1. Sketch of NASA orthogonal 'projection dimensions', from [24]. 15
2.2. Overview of fragments of HVI tests from [17]. The original satellite was a cube with an edge length of 20 cm, part of which can be seen in the top left corner of the middle picture. 15
2.3. Aspect ratio versus thinness distributions from two different HVI tests [17]. The aspect ratio is the x and y dimension of a fragment as defined in figure 2.1. Thinness is the ratio of y to z. 16

3.1. Experimental results for coupling coefficient from [16] for aluminium, solar cells and a polyimide. The first scan of the polyimide was used to clean the surface of the target. 21
3.2. Simulation results for the coupling coefficient and total thrust for gold and aluminium vs. fluence Φ_T [16] 22
3.3. Typical behavior of the coupling coefficient vs. fluence for aluminium 23
3.4. Behavior of coupling coefficient and reflectivity vs. incidence angle from [16]. Any geometrical effects were corrected for, in order to keep the fluence Φ_T on the target constant. 24

4.1. Call graph of MainCore() 33
4.2. Simplified flowchart for the simulation of the laser-debris interaction within EXPEDIT 34
4.3. Area approach: The impulse generated on a surface is calculated by assuming constant fluence Φ_T and a constant coupling coefficient c_m for the entire surface. 35
4.4. Call graph for CheckForHitsAreaVersion() 36
4.5. Net method - Discretization of the debris object: Each surface is divided into smaller surfaces which each can have individual values for the fluence Φ_T and the coupling coefficient c_m. 37
4.6. Call graph for CheckForHitsNetVersion() 38
4.7. Beam method - Discretization of the laser beam: The laser beam is divided into many individual beams, each with individual fluence Φ_F. The first intersection of each ray with the debris object is evaluated in order to calculate the local coupling coefficient c_m and the resulting impulse $\boldsymbol{p}$. 38
4.8. Call graph for beam method 40
4.9. Wedge irradiated by pulsed laser. Based on [25]. This shows the wedge in the stable position. If initial position is rotated around the x-axis, the wedge will begin oscillating. The equations below only remain valid, if no self-shadowing occurs: $|\Phi| \leq 45°$ 46

5.1. Values for coupling coefficient gained from VLL simulations for a pulse length of 500 ps and a wavelength of 1064 nm. 49
5.2. Relationship between the lowering of the perigee h_p and ξ assuming best, neutral and worst directions for radial impulse for a circular orbit and a single pulse. 53
5.3. Relationship between the change of the perigee Δh_p and ξ for a single pulse, assuming optimal and worst directions for the radial impulse component. The impulse is transferred at the apogee of a elliptical orbit with $h_p = 800km$ and $h_a = 900km$. . . . 54
5.4. Oscillation of wedge shaped debris. Simulated with a constant fluence $\Phi_L = 25000\frac{J}{m^2}$ and coupling coefficient $c_m = 25\frac{\mu N}{W}$ and the repetition rate $\nu = 200Hz$. 56
5.5. HD-Model of a set of pliers taken from [14] 57
5.6. Progression of impulse transfer and orientation from default initial orientation . . . 57
5.7. Progression of impulse transfer and orientation from default initial orientation allowing free movement of pliers 58
5.8. Progression of impulse transfer and orientation. Initial orientation tilted 1.41° from default 58
5.9. Progression of impulse transfer and orientation. Initial orientation tilted 7.07° from default 59
5.10. Results of parameter study for constant power $P = const = E_p \cdot \nu$ with varying fluence. $c_m(\Phi)$ as given in 5.1. 60
5.11. Relationship of time until the debris object moves one beam diameter radially and the distance of the laser beam from the center of mass of the debris object, calculated using mode 5 61
5.12. Spatial distribution of laser fluence and probability of debris position. FWHM for Φ is 0.5 m, for debris position probability the FWHM is 0.1 m 62
5.13. Axial impulse transfer for different target shapes - calculated using mode 6 63
5.14. ξ and η_j for different shapes 64
5.15. ξ, η_j and η_c for a sphere 65
5.16. Comparison of η_j and ξ for a plate with a constant c_m (analytic) and a spatially variable $c_m(\Phi_T)$ (numeric) 66
5.17. Comparison of η_j and ξ for a plate with spatially constant $c_m(\Phi_L)$ (analytic) and a spatially variable $c_m(\Phi_T)$ (numeric) 67

D.1. Wedge with relevant parameters: Forces F_1 and F_2, the corresponding lever arms r_1 and r_2, the length of an edge h and the position of the center of mass. The laser beam irradiates the wedge from the bottom. The figure shows the neutral and stable position ($\Phi = 0$). If the wedge is rotated out of this stable state, it will begin oscillating around its center of mass. The equations below only remain valid if no self-shadowing occurs. 97

E.1. Work breakdown structure 110

List of Tables

4.1. Verification results 48

Nomenclature

Within this thesis vectors are represented by bold lower case letters. Matrices are represented by bold upper case letters.

Latin letters

A	Surface area	m^2
c_m	Coupling coefficient	$\frac{N}{W}$
d	Diameter	m
E	Energy	J
$\boldsymbol{G}$	Area matrix	$-$
g	Accelaration due to gravity	$\frac{m}{s^2}$
Δh_p	Perigee alteration	m
I	Intensity	$\frac{W}{m^2}$
I_{sp}	Specific impulse	s
$\boldsymbol{k}$	Propagation direction of laser beam	
$\boldsymbol{L}$	Angular Momentum	Nms
m	Mass	kg
$\boldsymbol{n}$	Normal vector of a surface	$-$
P	Power	W
$\boldsymbol{p}$	Impulse	Ns
r	Radius	m
$\boldsymbol{r}$	Position	m
T	Temperature	K
t	Time	s
v	Velocity	$\frac{m}{s}$
$\angle$	Angles of orientation	

Greek letters

η_c	Effective axial impulse to reference axial impulse	$-$
η_j	Effective axial impulse to maximum axial impulse	$-$
λ	Wavelength	m
μ	Standard gravitational parameter	$\frac{m^3}{s^2}$
ν	Repetition rate	$\frac{1}{s}$
$\boldsymbol{\omega}$	Angular velocity	$\frac{rad}{s}$
Φ	Roll	rad

Φ_L	Fluence of laser beam	$\frac{J}{m^2}$
Φ_T	Fluence on target	$\frac{J}{m^2}$
Ψ	Yaw	rad
ρ	Density	kg/m^3
Θ	Pitch	rad
θ	Angle of incidence	rad
ξ	Ratio of radial to axial impulse components	$-$

Indices

axial	Axial component
base	Base point of an element of the debris object
deb	Debris
debris	Debris
ECI	Global Coordinates, similiar to ECI
eff	effective
ele	element
FWHM	Full width at half maximum
inc	incoming
jet	exhaust jet
laser	Laser
max	Maximum
min	Minimum
opt	optimum
p	Pulse
radial	Radial component
rec	rectangle
ref	reference
T	Target
tri	triangle

Acronyms

SSN	Space Surveillance Network
CFRP	Carbon fiber reinforced plastic
DLR	German Aerospace Center (Deutsches Zentrum für Luft- und Raumfahrt e.V.)
EXPEDIT	Tool created for this thesis. Examination Program for irregularly shaped Debris targets

FWHM	Full width half maximum
GFRP	Glass fiber reinforced plastic
HVI	High velocity impact
ILR	Institute of Aerospace Systems (Institut für Luft- und Raumfahrtsysteme)
LASER	Light amplification by stimulated emission of radiation
LDEF	Long Duration Exposure Facility

A German summary

Um unkooperative Weltraummüllobjekte aus ihrer Umlaufbahn zu entfernen, wird am Institut für Technische Physik des DLR in Stuttgart die Möglichkeit untersucht, diese Objekte per Laserablation aus dem Erdorbit zu entfernen. Diese Methode hat den einzigartigen Vorteil, dass die Interaktion mit dem Weltraumschrott auch über weite Distanzen stattfinden kann, zum Beispiel von der Erdoberfläche aus. Kurze, hochenergetische Laserpulse heizen die oberste Schicht des Weltraummüllobjektes auf, bis diese in den gasförmigen Zustand übergeht und durch den dabei entstehenden Druck vom Weltraummüll weg beschleunigt wird. Der dadurch entstehende Schub nutzt dasselbe Prinzip, wie klassische chemische Raketentriebwerke. Idealerweise wird die Umlaufbahn des Weltraumschrotts durch diesen Impulsübertrag so weit abgesenkt, dass er direkt in die Atmosphäre eintritt oder nur noch eine kurze Lebensdauer hat. Die Richtung des durch den Laserpuls entstehenden Schubes wird allerdings nicht durch die Richtung des Laserpulses bestimmt, sondern ist immer normal zur Oberfläche. Dadurch kommt der Form und Ausrichtung des Weltraumschrotts große Bedeutung, zu um die tatsächliche Richtung des Impulses zu bestimmen. Dies bedingt auch große Unsicherheiten in der Berechnung des Impulses, da sowohl Form als auch Orientierung bei einem kleinen (1 cm -10 cm) Weltraumschrottteilchen nur sehr schwer und ungenau messbar sind.

Es wurde untersucht, welche Formen für Weltraumschrottobjekte zu erwarten sind. Die meisten Objekte sind durch Kollisionen oder Explosionen auf der Umlaufbahn entstanden. Daher sind Hyper Velocity Impact Tests eine wichtige Informationsquelle für diese Fragestellung. Die einzigen Tests für einen modernen Satelliten in entsprechender Größe sind die DebriSat-Experimente, die 2014 stattgefunden haben. Leider sind die Ergebnisse dieser Studien noch nicht verfügbar. Ältere Experimente oder jüngere Experimente mit Mikrosatelliten legen nahe, dass Platten und Ellipsoiden brauchbare Annäherungen für einen Großteil der Weltraummüllpopulation sind.

Die Effizienz der Laserablation wird über den sogenannten Kopplungskoeffizenten c_m bestimmt, der das Verhältnis von Impulsübertrag zu Pulsenergie beschreibt. Der genaue Wert des Kopplungskoeffizienten ist von vielen Variablen abhängig, besonders von der lokalen Fluenz. Dies macht analytische Betrachtungen des Impulsvektors sehr aufwendig, wenn nicht viele Effekte vernachlässigt werden. Für die folgenden Betrachtungen wurde der Koppelkoeffizient als $c_m(\Phi)$ simuliert. Ein $c_m(\Phi)$-Verlauf ist aber nur für eine bestimmte Kombination von Material, Pulsdauer, Wellenlänge und Polarisation gültig. Sollen andere Laserparameter untersucht werden, muss der entsprechende Verlauf für $c_m(\Phi)$,z.B.durch aufwendige hydro- oder molekulardynamische Simulationen bestimmt werden.

Das primäre Ziel dieser Arbeit war die Erstellung eines Software-Tools, welches die Wechselwirkung zwischen Laser und Weltraumschrott simulieren kann. Besonderer Wert wurde auf die Möglichkeit gelegt, komplexe Geometrien in beliebiger Ausrichtung simulieren zu können. Das Programm EXPEDIT wurde in C++ geschrieben und im Anschluss genutzt, um Parameterstudien

durchzuführen. Je nachdem, wie komplex die Anfangsbedingungen sind, stehen innerhalb von EXPEDIT verschiedene Berechnungsmethoden zur Verfügung. Für Rechnungen mit konstanter Fluenz und konstantem Koppelkoeffizienten wurden quasi-analytische Methoden implementiert. Für komplexe Geometrien oder realistische Laserparameter, wie eine Gauß'sche Verteilung der Fluenz, wird die Geometrie oder der Laserstrahl diskretisiert, um Effekte wie Schatten und die Variation des Koppelkoeffizienten berücksichtigen zu können. Zum Einlesen der Oberflächengeometrie eines Weltraumschrottobjekts wurden zwei Möglichkeiten vorgesehen: In einer XML-Datei können einfache Formen mit einer Kombination von Rechtecken, Dreiecken und Kugeln erstellt werden. Komplexe Geometrien können durch STL-Dateien eingelesen werden, welche Oberflächen als Netz aus dreieckigen Elementen speichern. Um auch Pulsfolgen untersuchen zu können, wurden Methoden implementiert, welche die Bewegungen des Weltraumschrotts simulieren. Besonders wurde dabei auf die Simulation der Rotation geachtet, da die Ausrichtung des Weltraumschrotts einen maßgeblichen Einfluss auf den Impulsübertrag hat.

Bei der Simulation der ersten Szenarien ist die starke Abhängigkeit des Ergebnisses von den Anfangsbedingungen deutlich hervorgetreten: Kleine Änderungen in der Ausrichtung zu Beginn der Simulation führten zu komplett unterschiedlichen Verläufen und Ergebnissen. Um den Impulsübertrag korrekt simulieren zu können, sind exakte Informationen über die Anfangsbedingungen notwendig. Sind die Anfangsbedingungen nicht in der nötigen Genauigkeit bekannt, haben die Einzelfall-Simulationen nur begrenzte Aussagekraft. Um trotzdem allgemeingültige Aussagen bzgl. des Impulsübertrages zu ermöglichen, wurde in EXPEDIT die Möglichkeit implementiert, automatisiert Parameterstudien durchzuführen, indem bestimmte Anfangsbedingungen variiert werden. Sechs dieser "modes" wurden implementiert und im Rahmen der Parameterstudien genutzt.

Zwei Kenngrößen wurden eingeführt, um den Impulsübertrag für eine gewisse Geometrie zu charakterisieren, η_j und ξ:

η_j: Verhältnis von durchschnittlichen Axialimpuls zu dem Axialimpuls in optimaler Konstellation.

ξ: Verhältnis von Radialimpuls zu Axialimpuls.

Die Aufteilung in Radial- und Axialimpulskomponenten, im Bezug zur Propagationsrichtung des Laserstrahls, wurde durchgeführt, um die kontrollier- und vorhersagbaren axialen Anteile getrennt von den radialen Anteilen zu betrachten. Da der Axialimpuls immer parallel zum Laserstrahl läuft, ist dessen Richtung bekannt. Aber auch wenn der Betrag des Radialimpuls abgeschätzt werden kann, so kann die Richtung nicht vorhergesagt werden. So könnte der Radialimpuls entgegengesetzt der aktuellen Bewegungsrichtung des Weltraumschrotts auftreten und die Bahn weiter senken, aber ebenso kann das Gegenteil eintreten. So ist ein hoher Wert für ξ nicht direkt schlecht, aber er erschwert die Vorhersage der Bahnänderungen erheblich. EXPEDIT kann genutzt werden, um Werte für ξ und η_j für eine bestimmte Geometrie zu bestimmen, indem Ausrichtung und die Lage des Laserstrahls im Vergleich zum Weltraumschrott zufällig variiert werden. Aus den Mittelwerten einer entsprechend großen Menge an Stichproben können die Kennwerte und deren Abhängigkeiten abgeschätzt werden. Dies wurde für einige Beispielgeometrien durchgeführt. Im Rahmen der Auswertung der oben erwähnten DEBRISAT-Experimente sollen repräsentative Fragmente eingescannt werden. Sobald diese Scans verfügbar sind, können sie genutzt wer-

den, um ξ und η_j für typische Fragmentgeometrien zu bestimmen. Für Platten wurden im Rahmen der Parameterstudien für η_j Werte von 0,1 bis 0,3 und für ξ 0,4 bis über 1 berechnet, je nach Fluenz. Diese Werte sind problematischer als zu Beginn der Arbeit geschätzt, und Möglichkeiten zur Verbesserung sollten betrachtet werden.

Eine mögliche Methode zur Optimierung ist die Kopplung des Deorbit-Lasers mit den optischen Geräten für das Tracking. Bei der aktiven optischen Beobachtung von Weltraummüll wird die Laufzeit eines Laserpulses zur Entfernungsmessung genutzt. Die Stärke der zurückkehrenden Reflektion könnte verwendet werden, um die Momente zu erkennen, in denen das Weltraummüllobjekt seine "Breitseite" zum Beschuss anbietet. Die passive optische Beobachtung nutzt die Reflektion der Sonnenstrahlen um ein Objekt zu orten. Bei entsprechender Konstellation der Umlaufbahn zur Sonne könnte die Intensität der Reflektion verwendet werden, um doch die Richtung des Radialimpulses abzuschätzen.

Die Wiederholung der Parameterstudien aus Kapitel 5 mit anderen Laserparametern, insbesondere der Pulsdauer, und somit anderen Verläufen für $c_m(\Phi)$ könnte genutzt werden, um die Laserparameter im Bezug auf η_j und ξ zu optimieren.

Ohne zusätzliche Optimierung stellen die hohen Werte für ξ ein Problem für das Laser-Debris-Removal-Konzept dar. Obwohl im Durschnitt die Bahn durch die Bestrahlung abgesenkt wird, kann der Impulsübertrag in ungünstigen Einzelfällen die Bahn anheben und somit die Lebenszeit des Weltraumschrotts stark erhöhen. Um auszuschließen, dass die geänderte Bahn zu einer Kollision mit anderen Weltraumobjekten führt, müssten alle möglichen Bahnen nach dem Impulsübertrag entsprechend geprüft werden. Dieser Aufwand steigt mit ξ stark an. Im Vergleich dazu sind die durch ein niedriges η_j entstehenden Probleme, relativ simpel zu lösen: Mehr Leistung oder längere Bestrahlungskampagnen können diese Verluste ausgleichen.

B xml-files

B.1. Control file

```
<DebrisControl>If not mentioned otherwise. all entries in SI units!!!
  <Control>
    <MethodSwitch>1</MethodSwitch>0->beams, 1 ->Plate see documentation,2 net
    <BeamResolution>0.0001</BeamResolution>
    <NetResolution>100</NetResolution>
    <FilterL>0</FilterL>.00005->typical value
    <AllowMovement>2</AllowMovement>0:No 1: in XY 2 YES
    <Runtime>5</Runtime>in seconds
  </Control>
  <Input>
    <NameOfGeometryFile>DebrisGeometry.xml</NameOfGeometryFile>
    <TypeOfGeometryFile>0</TypeOfGeometryFile>0:xml, 1:stl
    <stlThickness>0.005</stlThickness>
    <stlDensity>2700</stlDensity>
    <Psi>0</Psi>um z
    <Theta>0</Theta>Einmalige Drehung des in der Geometrie Datei eingegeben Koerpers
    <Phi>0</Phi>Einheit [pi]!!!!!!
    <SwitchSolid>0</SwitchSolid>1: nutze unterer Werte
  </Input>
  <SolidBody>
      <Mass>1</Mass>
      <CenterOfMass>
        <X></X>
        <Y></Y>
        <Z></Z>
      </CenterOfMass>
      <InertiaTensor>
        <XX>1</XX>
        <XY>2</XY>
        <XZ>3</XZ>
        <YX>4</YX>
        <YY>5</YY>
        <YZ>6</YZ>
        <ZX>7</ZX>
        <ZY>8</ZY>
        <ZZ>9</ZZ>
      </InertiaTensor>
    </SolidBody>
  <Laser>
    <Fluence>25000</Fluence>J/m^2
    <Frequency>1</Frequency>
    <Diameter>0.5</Diameter>meter!
```

```
43      <FluenceDistribution>0</FluenceDistribution>0 constant, 1 Gauss
        <FWHM>0.5</FWHM>
45      <DiameterForComparison>0.5</DiameterForComparison>
        <ECI_X>0</ECI_X>position of station
47      <ECI_Y>0</ECI_Y>
        <ECI_Z>0</ECI_Z>
49      <FollowTarget>0</FollowTarget>
        <CenterOfHit>Im Schwerpunktkordiantensystem
51        <X>0</X>
          <Y>0</Y>
53        <Z>0</Z>
        </CenterOfHit>
55    </Laser>
      <LaserMatterInteraction>
57      <ConstCM>0</ConstCM>bei 0 wird analytische Formel verwendet, sonst der wert als
            konstante
        <CM>0.000025</CM>
59      <a0>-0.01314</a0> mikro N/cm^2
        <a1>0.01753</a1> mikro N/cm^2
61      <a2>0.01904</a2> mikro N/cm^2
        <a3>449.81</a3> s
63      <a4>632.06</a4> s
        <a5>913.51</a5> s
65      <t1>15.04</t1> J/cm^2
        <t2>1.19</t2> J/cm^2
67      <t3>2.41</t3> J/cm^2
        <t4>23.38</t4> J/cm^2
69    </LaserMatterInteraction>
      <Debris>Im ECI!
71      <InitialPosition>
          <X>0</X>
73        <Y>0</Y>
          <Z>100</Z>
75      </InitialPosition>
        <InitialAngularVelocity>in rad/s!!
77        <X>0</X>
          <Y>0</Y>
79        <Z>0</Z>
        </InitialAngularVelocity>
81    </Debris>
      <Modi>
83      <Modus>1</Modus>
        <OutputFileName>TestModus.dat</OutputFileName>
85      <Modus1></Modus1>
        <Modus2>
87        <Dimension>2</Dimension>
          <Fluence>
89          <Start>20000</Start>
            <End>30000</End>
91          <Steps>5</Steps>
          </Fluence>
93        <RepetitionRate>
```

```
        <Start>200</Start>
95      <End>400</End>
        <Steps>5</Steps>
97    </RepetitionRate>
    </Modus2>
99  <Modus3>
      <Dimension>1</Dimension>
101   <Fluence>
        <Start>1000</Start>
103     <End>50000</End>
        <Steps>10</Steps>
105   </Fluence>
    </Modus3>
107 <Modus4>
      <Dimension>3</Dimension>
109   <Wx>
        <Start>-1</Start>
111     <End>1</End>
        <Steps>20</Steps>
113   </Wx>
      <Wy>
115     <Start>-1</Start>
        <End>1</End>
117     <Steps>20</Steps>
      </Wy>
119   <Wz>
        <Start>-1</Start>
121     <End>1</End>
        <Steps>20</Steps>
123   </Wz>
  </Modus4>
125 <Modus5>
      <Dimension>2</Dimension>
127   <CenterOfHit_X>
        <Start>-1</Start>
129     <End>1</End>
        <Steps>20</Steps>
131   </CenterOfHit_X>
      <CenterOfHit_Y>
133     <Start>-1</Start>
        <End>1</End>
135     <Steps>20</Steps>
      </CenterOfHit_Y>
137 </Modus5>
    <Random>
139   <MaxAimError>0.23548</MaxAimError>
      <numberOfRuns>20</numberOfRuns>
141 </Random>
  <Modus7>Einheit rad, kein Pi!
143   <Dimension>3</Dimension>
      <Psi>
145     <Start>-1</Start>
```

```
        <End>1</End>
147     <Steps>20</Steps>
      </Psi>
149   <Theta>
        <Start>-1</Start>
151     <End>1</End>
        <Steps>20</Steps>
153   </Theta>
      <Phi>
155     <Start>-1</Start>
        <End>1</End>
157     <Steps>20</Steps>
      </Phi>
159 </Modus7>
  </Modi>
161 </DebrisControl>
```

B.2. Geometry file

```
1 <DebrisGeometry>All units in SI-units
  <Plates>
3   <NumberOfPlates>1</NumberOfPlates>
    <Plate1>
5     <PlateCorner1>
        <X>0</X>
7       <Y>0.1</Y>
        <Z>0</Z>
9     </PlateCorner1>
      <PlateCorner2>
11      <X>0</X>
        <Y>0</Y>
13      <Z>0</Z>
      </PlateCorner2>
15    <PlateCorner3>
        <X>0.1</X>
17      <Y>0.1</Y>
        <Z>0</Z>
19    </PlateCorner3>
      <PlateCorner4>
21      <X>0.1</X>
        <Y>0</Y>
23      <Z>0</Z>
      </PlateCorner4>
25    <PlateMaterial>1</PlateMaterial>1=Aluminium
      <PlateThickness>0.005</PlateThickness>
27    <PlateDensity>2700</PlateDensity>
    </Plate1>
29  <Plate2>
      <PlateCorner1>
31      <X>0</X>
        <Y>0</Y>
33      <Z>0.1</Z>
```

```
        </PlateCorner1>
35      <PlateCorner2>
          <X>0</X>
37        <Y>0</Y>
          <Z>0</Z>
39      </PlateCorner2>
        <PlateCorner3>
41        <X>0.1</X>
          <Y>0</Y>
43        <Z>0.1</Z>
        </PlateCorner3>
45      <PlateCorner4>
          <X>0.1</X>
47        <Y>0</Y>
          <Z>0</Z>
49      </PlateCorner4>
        <PlateMaterial>1</PlateMaterial>1=Aluminium
51      <PlateThickness>0.005</PlateThickness>
        <PlateDensity>2700</PlateDensity>
53    </Plate2>
      <Plate3>
55      <PlateCorner1>
          <X>0</X>
57        <Y>0</Y>
          <Z>0.1</Z>
59      </PlateCorner1>
        <PlateCorner2>
61        <X>0</X>
          <Y>0</Y>
63        <Z>0</Z>
        </PlateCorner2>
65      <PlateCorner3>
          <X>0</X>
67        <Y>0.1</Y>
          <Z>0.1</Z>
69      </PlateCorner3>
        <PlateCorner4>
71        <X>0</X>
          <Y>0.1</Y>
73        <Z>0</Z>
        </PlateCorner4>
75      <PlateMaterial>1</PlateMaterial>1=Aluminium
        <PlateThickness>0.005</PlateThickness>
77      <PlateDensity>2700</PlateDensity>
    </Plate3>
79  <Plate4>
      <PlateCorner1>
81      <X>0</X>
        <Y>0</Y>
83      <Z>0.1</Z>
      </PlateCorner1>
85    <PlateCorner2>
```

```
            <X>0.1</X>
87          <Y>0.1</Y>
            <Z>0.1</Z>
89        </PlateCorner2>
          <PlateCorner3>
91          <X>0</X>
            <Y>0.1</Y>
93          <Z>0.1</Z>
          </PlateCorner3>
95        <PlateCorner4>
            <X>0.1</X>
97          <Y>0</Y>
            <Z>0.1</Z>
99        </PlateCorner4>
          <PlateMaterial>1</PlateMaterial>1=Aluminium
101       <PlateThickness>0.005</PlateThickness>
          <PlateDensity>2700</PlateDensity>SI EINHEITEN!
103     </Plate4>
      <Plate5>
105       <PlateCorner1>
            <X>0</X>
107         <Y>0.1</Y>
            <Z>0.1</Z>
109       </PlateCorner1>
          <PlateCorner2>
111         <X>0</X>
            <Y>0.1</Y>
113         <Z>0</Z>
          </PlateCorner2>
115       <PlateCorner3>
            <X>0.1</X>
117         <Y>0.1</Y>
            <Z>0.1</Z>
119       </PlateCorner3>
          <PlateCorner4>
121         <X>0.1</X>
            <Y>0.1</Y>
123         <Z>0</Z>
          </PlateCorner4>
125       <PlateMaterial>1</PlateMaterial>1=Aluminium
          <PlateThickness>0.005</PlateThickness>
127       <PlateDensity>2700</PlateDensity>SI EINHEITEN!
        </Plate5>
129   <Plate6>
          <PlateCorner1>
131         <X>0.1</X>
            <Y>0</Y>
133         <Z>0.1</Z>
          </PlateCorner1>
135       <PlateCorner2>
            <X>0.1</X>
137         <Y>0</Y>
```

```
            <Z>0</Z>
139         </PlateCorner2>
            <PlateCorner3>
141           <X>0.1</X>
              <Y>0.1</Y>
143           <Z>0.1</Z>
            </PlateCorner3>
145         <PlateCorner4>
              <X>0.1</X>
147           <Y>0.1</Y>
              <Z>0</Z>
149         </PlateCorner4>
            <PlateMaterial>1</PlateMaterial>1=Aluminium
151         <PlateThickness>0.005</PlateThickness>
            <PlateDensity>2700</PlateDensity>SI EINHEITEN!
153       </Plate6>
        </Plates>
155     <Triangles>
          <NumberOfTriangles>0</NumberOfTriangles>
157       <Triangle1>
            <TriangleCorner1>
159           <X>0</X>
              <Y>0</Y>
161           <Z>0</Z>
            </TriangleCorner1>
163         <TriangleCorner2>
              <X>0</X>
165           <Y>0.1</Y>
              <Z>0</Z>
167         </TriangleCorner2>
            <TriangleCorner3>
169           <X>0.1</X>
              <Y>0</Y>
171           <Z>0</Z>
            </TriangleCorner3>
173         <TriangleThickness>0.005</TriangleThickness>
            <TriangleDensity>2700</TriangleDensity>SI EINHEITEN!
175       </Triangle1>
          <Triangle2>
177         <TriangleCorner1>
              <X>0.1</X>
179           <Y>0.1</Y>
              <Z>0</Z>
181         </TriangleCorner1>
            <TriangleCorner2>
183           <X>0</X>
              <Y>0.1</Y>
185           <Z>0</Z>
            </TriangleCorner2>
187         <TriangleCorner3>
              <X>0.1</X>
189           <Y>0</Y>
```

```
        <Z>0</Z>
      </TriangleCorner3>
      <TriangleThickness>0.005</TriangleThickness>
      <TriangleDensity>2700</TriangleDensity>SI EINHEITEN!
    </Triangle2>
    <Triangle3>
      <TriangleCorner1>
        <X>0</X>
        <Y>0</Y>
        <Z>0</Z>
      </TriangleCorner1>
      <TriangleCorner2>
        <X>0</X>
        <Y>0</Y>
        <Z>0.1</Z>
      </TriangleCorner2>
      <TriangleCorner3>
        <X>0.1</X>
        <Y>0</Y>
        <Z>0</Z>
      </TriangleCorner3>
      <TriangleThickness>0.005</TriangleThickness>
      <TriangleDensity>2700</TriangleDensity>SI EINHEITEN!
    </Triangle3>
    <Triangle4>
      <TriangleCorner1>
        <X>0.1</X>
        <Y>0</Y>
        <Z>0.1</Z>
      </TriangleCorner1>
      <TriangleCorner2>
        <X>0</X>
        <Y>0</Y>
        <Z>0.1</Z>
      </TriangleCorner2>
      <TriangleCorner3>
        <X>0.1</X>
        <Y>0</Y>
        <Z>0</Z>
      </TriangleCorner3>
      <TriangleThickness>0.005</TriangleThickness>
      <TriangleDensity>2700</TriangleDensity>SI EINHEITEN!
    </Triangle4>
  </Triangles>
  <Spheres>
    <NumberOfSpheres>0</NumberOfSpheres>
    <Sphere1>
      <Radius>0.1</Radius>
      <Position>
        <X>-0.1</X>
        <Y>0</Y>
        <Z>-1</Z>
```

```
        </Position>
243     <SphereMaterial>1</SphereMaterial>1=Aluminium
        <SphereDensity>2700</SphereDensity>SI EINHEITEN!
245    </Sphere1>
       <Sphere2>
247     <Radius>0.001</Radius>
        <Position>
249       <X>0.1</X>
          <Y>0</Y>
251       <Z>1</Z>
        </Position>
253     <SphereMaterial>1</SphereMaterial>1=Aluminium
        <SphereDensity>2700</SphereDensity>SI EINHEITEN!
255    </Sphere2>
  </Spheres>
257 </DebrisGeometry>
```

C The verification cases

Since the analytical models are based on a constant c_m, all of the following cases are calculated with $c_m = 25\frac{\mu N}{W}$. The fluence ϕ_L was also assumed to be spatially constant with $\Phi = 25000\frac{J}{m^2}$. For all cases with a laser pulse series, a repetition rate of $\nu = 200Hz$ was used. The density of all debris object is assumed to be $2700\frac{kg}{m^3}$.

C.1. The plate

For all three plate cases the same plate $(0.1m \times 0.1m \times 0.005m)$ was used. The default orientation of the plate was in the x-y plane and thus perpendicular to the laser irradiation.

C.1.1. Plate1

This case contains simply the plate in the original position.

C.1.2. Plate2

In this case the initial orientation of the plate is tilted by $\Delta\Theta = \frac{\pi}{4}$.

C.1.3. Plate3

In this case the initial orientation of the plate is tilted by $\Delta\Phi = \frac{\pi}{4}$.

C.2. Sphere

A solid sphere with a radius of 0.1 m was used. The net method cannot be used for spherical shapes, thus no results are in that column.

C.2.1. Sphere mesh

The exact same sphere was modelled using triangular polygons in a STL-file. The results differ a little since a sphere cannot perfectly be represented by a practical number of triangular elements.

C.3. Wedge

The wedge is formed of two plates with the same dimensions as the plates above, connected in a 90° angle.

C.3.1. Wedge1

In this case one side of the wedge war perpendicular to the laser beam, while the other was exactly parallel to the laser beam. The imparted impulse should be the same as in Plate1 but since the center of mass is shifted, in this case an angular momentum is generated.

C.3.2. Wedge2

The wedge is oriented as shown in figure 4.9.

C.3.3. Wedge Oscillation

The oscillation described in 4.6.2 was simulated here in order to compare the frequency of the oscillation. Thus impulse and angular momentum are not noted here. Since the simulation of the oscillation only works if the calculation of the impulse the angular momentum and the rotation are done correctly this is a comprehensive test of most utilities provided in EXPEDIT.

C.3.4. Wedge mesh

The same oscillation as above modelled, with the addition of the wedge being represented by a mesh of triangular polygons, provided by an STL-file.

C.4. Cone

In order to simulate the oscillation described in 4.6.2, a cone was constructed as a mesh of triangular polygons. The height of the cone was 0.1 m and the radius of the base surface was 0.1 m.

D Derivation of oscillation frequency for irradiated wedge

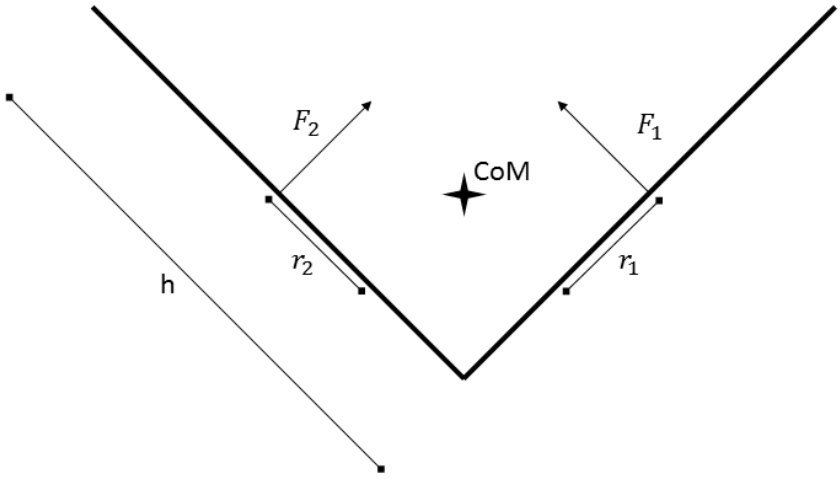

Figure D.1.: Wedge with relevant parameters: Forces F_1 and F_2, the corresponding lever arms r_1 and r_2, the length of an edge h and the position of the center of mass. The laser beam irradiates the wedge from the bottom. The figure shows the neutral and stable position ($\Phi = 0$). If the wedge is rotated out of this stable state, it will begin oscillating around its center of mass. The equations below only remain valid if no self-shadowing occurs.

Here the oscillation period of an irradiated wedge will be derived. The problem will be reduced to a 2D case and only rotation around the x-axis will be evaluated. The initial orientation of the plane is shown in 4.9. For Φ clockwise will be used as positive direction. The purpose of this appendix is the justification of the change on the erroneous equation given in [25]. For the following equations it is assumed that the wedge is made of two quadratic plates with an edge length of 0.1 m, which enclose an angle of 90° between then.

If $\Delta\Phi$ is defined as the counter-clockwise rotation, then the sum of angular momentum is

$$I_x \ddot{\Phi} = r_1 F_1 - r_2 F_2, \tag{D.1}$$

where I_x ist the moment of inertia in regard to the x-axis. r_1 and r_2 are the lever arms of the forces F_1 and F_2. These can be defined as

$$F_1 = c_m \cdot I \cdot A_1 \cdot \cos\left(\Phi + \frac{\pi}{4}\right) \tag{D.2}$$

$$F_2 = c_m \cdot I \cdot A_2 \cdot \sin\left(\Phi + \frac{\pi}{4}\right) \tag{D.3}$$

with the intensity I and the surface area of each plate A. In these equations a continous ablation is presumed, which causes the errors discussed in section 3.5.2. Using these definitions for F_1 and F_2 equation D.1 becomes:

$$I_x\ddot{\Phi} = r_1 \cdot c_m \cdot I \cdot A_1 \cdot \cos\left(\Phi + \frac{\pi}{4}\right) - r_2 \cdot c_m \cdot I \cdot A_2 \cdot \sin\left(\Phi + \frac{\pi}{4}\right) \tag{D.4}$$

Since $r_1 = r_2 = \frac{h}{4}$ and $A_1 = A_2 = h^2$ this can be simplified to

$$I_x\ddot{\Phi} = c_m \cdot I \cdot \frac{h^3}{4}\left(\cos\left(\Phi + \frac{\pi}{4}\right) - \sin\left(\Phi + \frac{\pi}{4}\right)\right). \tag{D.5}$$

With the trigonometric sum-to-product identity [1]

$$\cos x + \cos y = 2\cos\frac{x+y}{2}\cos\frac{x-y}{2} \tag{D.6}$$

The following transformations can be made:

$$\begin{aligned}
\cos x - \sin x &= \cos x + \cos\left(x + \frac{\pi}{2}\right) && \text{(D.7)}\\
&= 2\cos\left(x + \frac{\pi}{4}\right)\cos\left(\frac{\pi}{4}\right) && \text{(D.8)}\\
&= \sqrt{2}\cos\left(x + \frac{\pi}{4}\right) && \text{(D.9)}\\
&= -\sqrt{2}\sin\left(x - \frac{\pi}{4}\right) && \text{(D.10)}
\end{aligned}$$

Thus, Equation D.5 can be written as

$$I_x\ddot{\Phi} = -\frac{\sqrt{2}}{4} \cdot c_m \cdot I \cdot h^3 \sin(\Phi). \tag{D.11}$$

With, as given in [25],

$$I_x = \frac{5}{24}mh^2 \tag{D.12}$$

and some sorting, the final result is:

$$\ddot{\Phi} = -\frac{\sqrt{2} \cdot 12}{10}\frac{c_m \cdot I \cdot h}{m}\sin(\Phi) \tag{D.13}$$

This is an equation very similar to the mathematical pendulum and the corresponding solutions apply here. However, the solution given in equation 4.38 is only valid for small oscillations, since it includes the linearization $\sin(\Phi) \approx \Phi$, which is only valid for small values of Φ. If larger oscillations are to be compared, additional correction factors have to be applied.

[1] Bronstein, Taschenbuch der Mathematik, Harry Deutsch, Thun, Frankfurt am Main, 2. Auflage 1995. 2.6.2.6.

E Projektmanagement

E.1. Work Package Description

		AP 1100
Titel	**Laserablation**	**Seite:** 1 von 11
Verantwortlicher	Jascha Wilken	**Version:** 1.0
		Datum: 27.07.2014
Beginn	T_0	
Ende	T_0+1 Woche	**Dauer**: 1 Woche
Bearbeiter	Jascha Wilken	

Ziele:
- Literaturrecherche zur Laserablation

Input:
- Literatur zur Laserablation

Schnittstellen zu anderen APs:
- **AP 1200:** Grundlage zur lasergestützten Entfernung von Weltraummüll
- **AP 2000:** Grundlage für die numerischen Modellierungen

Zweck:
- Gewinnung von Verständnis über grundlegende Funktionsweise der Laserablation

Ergebnisse:
- Erkenntnisse über grundlegende Funktionsweise der Laserablation

		AP 1200
Titel	**Entfernung von Weltraummüll**	**Seite:** 2 von 11
Verantwortlicher	Jascha Wilken	**Version:** 1.0
		Datum: 27.07.2014
Beginn	T_0+1 Woche	
Ende	T_0+2 Wochen	**Dauer**: 1 Woche
Bearbeiter	Jascha Wilken	

Ziele:
• Literaturrecherche zur aktiven Entfernung von Weltraummüll

Input:
• Literatur zur lasergestützen Entfernung von Weltraummüll

Schnittstellen zu anderen APs:
•**AP 2000:** Grundlage für die numerischen Modellierungen

Zweck:
• Erkenntisse über das Funktionsprinzip des Entfernens von Weltraummüll mit Hilfe der Laserablation

Ergebnisse:
• Erkenntisse über das Funktionsprinzip des Entfernens von Weltraummüll mit Hilfe der Laserablation

		AP 1300
Titel	**Weltraummüll**	**Seite:** 3 von 11
Verantwortlicher	Jascha Wilken	**Version:** 1.0
		Datum: 27.07.2014
Beginn	T_0+2 Wochen	
Ende	T_0+3 Wochen	**Dauer**: 1 Woche
Bearbeiter	Jascha Wilken	

Ziele:
- Literaturrecherche zur Weltraummüllsituation

Input:
- Literatur zur Weltraummüllsituation

Schnittstellen zu anderen APs:
- **AP 2200:** Grundlage für die Auswahl und Modellierung von Geometrien

Zweck:
- Gewinnung eines Überblicks über die Weltraummüllsituation

Ergebnisse:
- Mögliche Zielgeometrien und Zielorbits für folgende Modellierungen

		AP 1300
Titel	**Virtual Laser Lab**	**Seite:** 4 von 11
Verantwortlicher	Jascha Wilken	**Version:** 1.0
		Datum: 27.07.2014
Beginn	T_0+3 Wochen	
Ende	T_0+4 Wochen	**Dauer:** 1 Woche
Bearbeiter	Jascha Wilken	

Ziele:
- Einarbeitung in das Online-Simulationstool VLL

Input:
- Dokumentation zu VLL

Schnittstellen zu anderen APs:
- **AP 2200** VLL liefert Koeffizienten zur Berechnung der resultierenden Schübe

Zweck:
- Durchführung von Simulation zur Gewinnung von Daten bzgl. der Kopplungskoeffizienten

Ergebnisse:
- Daten bzgl. der Kopplungskoeffizienten

		AP 1300
Titel	**Modellierung der Geometrien**	**Seite:** 5 von 11
Verantwortlicher	Jascha Wilken	**Version:** 1.0
		Datum: 27.07.2014
Beginn	T_0+4 Wochen	
Ende	T_0+5 Wochen	**Dauer**: 1 Woche
Bearbeiter	Jascha Wilken	

Ziele:
- Erstellung von Modellen zur Eingabe und Berechung verschiedener Geometrien

Input:
- Erkenntnisse aus AP 1300

Schnittstellen zu anderen APs:
- **AP 1300:** Liefert die Geometrien, die modelliert werden

Zweck:
- Bereitstellung der Geometrien zur weiteren Berechnung der durch Laserablation erzeugten Impulse

Ergebnisse:
- Numerische Modelle der entsprechenden Weltraummüllgeometrien

		AP 1300
Titel	**Impulsübertragung**	**Seite:** 6 von 11
Verantwortlicher	Jascha Wilken	**Version:** 1.0
		Datum: 27.07.2014
Beginn	T_0+5 Wochen	
Ende	T_0+6 Wochen	**Dauer**: 1 Woche
Bearbeiter	Jascha Wilken	

Ziele:
- Numerische Modellierung der lasergestützten Impulsübertragung

Input:
- Erkenntnisse aus vorherigen APs

Schnittstellen zu anderen APs:
- **AP 1100:** Grundlagen der Laserablation
- **AP 1400:** Ergebnisse des VLL
- **AP 2100:** Numerische Modelle der Weltraummüllgeometrien

Zweck:
- Numerische Berechnung des durch Laserablation übertragenen Impulses auf Zielobjekt

Ergebnisse:
- Code zur Berechnung des durch Laserablation übertragenen Impulses auf Zielobjekt

		AP 1300
Titel	**Resultierende Bahnänderungen**	**Seite:** 7 von 11
Verantwortlicher	Jascha Wilken	**Version:** 1.0
		Datum: 27.07.2014
Beginn	T_0+6 Wochen	
Ende	T_0+7 Wochen	**Dauer:** 1 Woche
Bearbeiter	Jascha Wilken	

Ziele:
- Bestimmung der resultierenden Bahnänderungen

Input:
- Übertragener Impuls auf Grundlage von AP 2200

Schnittstellen zu anderen APs:
- **AP 2200:** Berechnung des übertragenen Impulses

Zweck:
- Numerische Berechnung der resultierenden Bahnänderungen und der Abschätzung der neuen Lebensdauer

Ergebnisse:
- Neue Bahnparameter und Lebenszeit

		AP 1300
Titel	**Modellierung in C++**	**Seite:** 8 von 11
Verantwortlicher	Jascha Wilken	**Version:** 1.0
		Datum: 27.07.2014
Beginn	T_0+7 Wochen	
Ende	T_0+13 Wochen	**Dauer**: 6 Wochen
Bearbeiter	Jascha Wilken	

Ziele:
• Erstellung und Prüfung eines Codes in dem alle vorherigen numerischen Modelle zusammengeführt werden

Input:
• Numerische Modelle aus vorherigen APs

Schnittstellen zu anderen APs:
• **AP 2000:** Liefern numerische Modelle zur zentralen Implementierung

Zweck:
• Erstellung eines Programms in dem schnell und einfach Berechnungen für variable Parameter durchgeführt werden können

Ergebnisse:
• Programm mit oben beschriebenen Eigenschaften

		AP 1300
Titel	**Vergleich mit Area-Matrix-Konzept**	**Seite:** 9 von 11
Verantwortlicher	Jascha Wilken	**Version:** 1.0
		Datum: 27.07.2014
Beginn	T_0+13 Wochen	
Ende	T_0+17 Wochen	**Dauer**: 4 Wochen
Bearbeiter	Jascha Wilken	

Ziele:
- Vergleich mit Area-Matrix-Konzept von Liedahl et al.

Input:
- Literatur von Liedahl et al.

Schnittstellen zu anderen APs:
- **AP 2000:** Nutzung des erstellten Programms

Zweck:
- Vergleich des numerischen Modells mit dem analytischen Area-Matrix-Konzepts

Ergebnisse:
- Erkenntnisse über das numerische Modell und den analytischen Ansatz

		AP 1300
Titel	**Vergleich mit experimentellen Daten**	**Seite:** 10 von 11
Verantwortlicher	Jascha Wilken	**Version:** 1.0
		Datum: 27.07.2014
Beginn	T_0+17 Wochen	
Ende	T_0+21 Wochen	**Dauer:** 4 Wochen
Bearbeiter	Jascha Wilken	

Ziele:
- Vergleich mit experimentellen Daten

Input:
- Experimentelle Daten

Schnittstellen zu anderen APs:
- **AP 2000:** Nutzung des erstellten Programms zum Erstellen von Vergleichswerten

Zweck:
- Überprüfung der numerischen Ergebnisse

Ergebnisse:
- Erkenntnisse über Gültigkeit der numerischen Ergebnisse

		AP 1300
Titel	**Dokumentation**	**Seite:** 11 von 11
Verantwortlicher	Jascha Wilken	**Version:** 1.0
		Datum: 27.07.2014
Beginn	T_0	
Ende	T_0+26 Wochen	**Dauer**: 26 Wochen
Bearbeiter	Jascha Wilken	

Ziele:
- Dokumentation der Masterarbeit

Input:
- Alle vorangegangenen APs

Zweck:
- Projektdokumentation

Ergebnisse:
- Schriftliche Dokumentation der Masterarbeit

E.2. Work breakdown structure

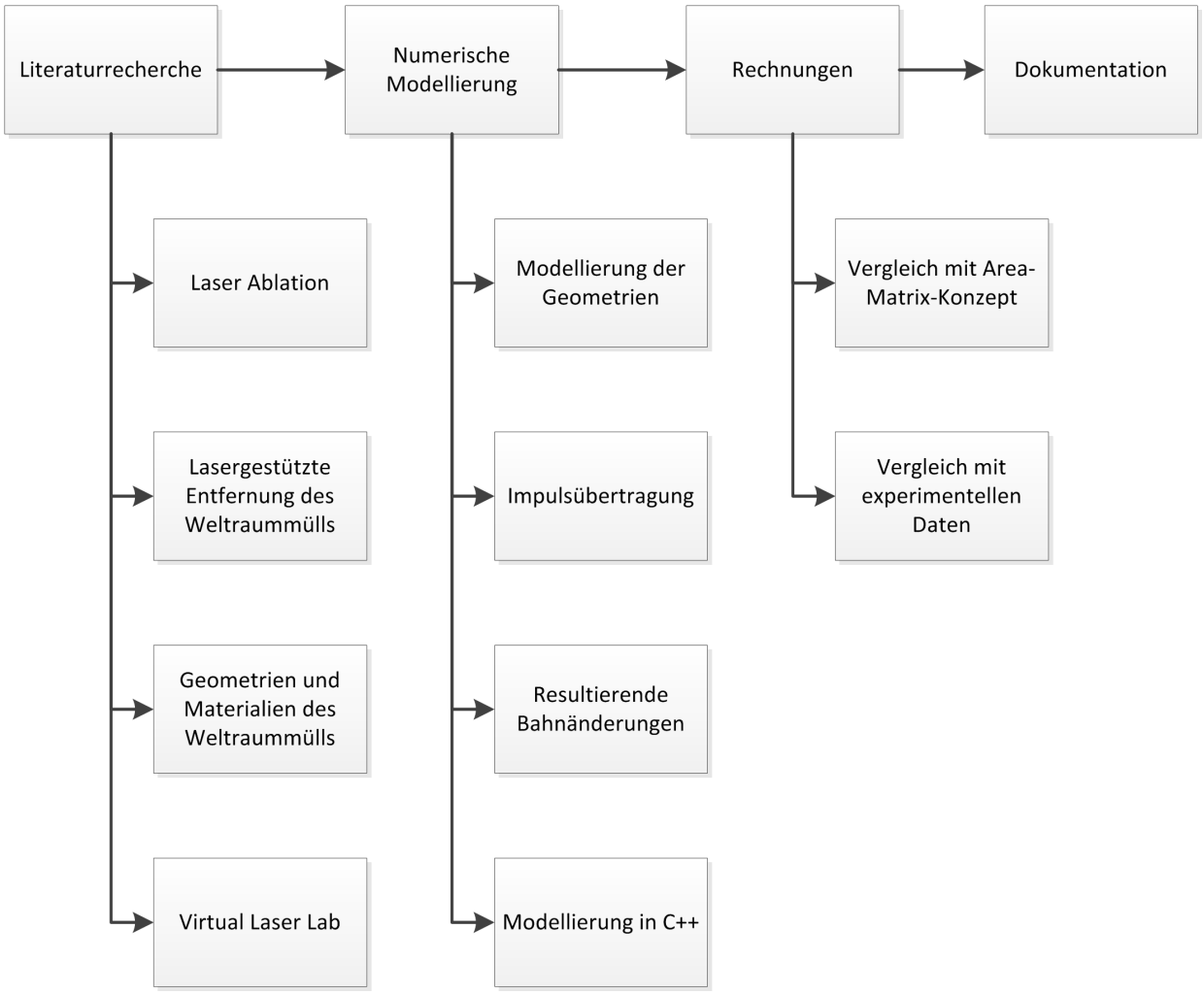

Figure E.1.: Work breakdown structure

E.3. Gantt-Diagramm

Nr.	Vorgangsname	Dauer	Anfang	Fertig stellen
1	**Masterarbeit**	**132 Tage**	**Fr 01.08.14**	**Sa 31.01.15**
2	**Literaturrecherche**	**21 Tage**	**Fr 01.08.14**	**Fr 29.08.14**
3	Laser Ablation	6 Tage	Fr 01.08.14	Fr 08.08.14
4	Lasergestützte Entfernung von Weltraummüll	5 Tage	Mo 11.08.14	Fr 15.08.14
5	Geometrien und Materialien des Weltraummülls	5 Tage	Mo 18.08.14	Fr 22.08.14
6	Virtual Laser Lab	5 Tage	Mo 25.08.14	Fr 29.08.14
7	**Numerische Modellierung**	**45 Tage**	**Mo 01.09.14**	**Fr 31.10.14**
8	Modellierung der Geometrien	5 Tage	Mo 01.09.14	Fr 05.09.14
9	Impulsübertragung	5 Tage	Mo 08.09.14	Fr 12.09.14
10	Resultierende Bahnänderungen	5 Tage	Mo 15.09.14	Fr 19.09.14
11	Modellierung in C++	30 Tage	Mo 22.09.14	Fr 31.10.14
12	**Rechnungen**	**40 Tage**	**Mo 03.11.14**	**Fr 26.12.14**
13	Vergleich mit Area-Matrix-Konzept	20 Tage	Mo 03.11.14	Fr 28.11.14
14	Vergleich mit experimentellen Daten	20 Tage	Mo 01.12.14	Fr 26.12.14
15	Dokumentation	131 Tage	Fr 01.08.14	Fr 30.01.15

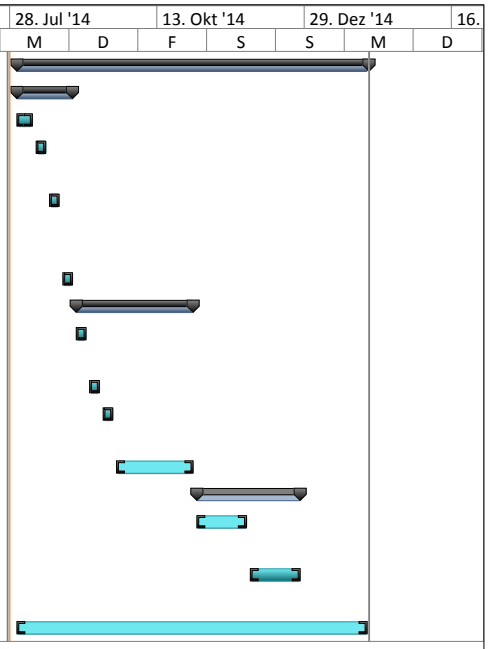

Projekt: Masterarbeit
Datum: Mo 28.07.14

Vorgang	Externer Meilenstein	Manueller Sammelrollup	
Unterbrechung	Inaktiver Vorgang	Manueller Sammelvorgang	
Meilenstein	Inaktiver Meilenstein	Nur Anfang	
Sammelvorgang	Inaktiver Sammelvorgang	Nur Ende	
Projektsammelvorgang	Manueller Vorgang	Stichtag	
Externe Vorgänge	Nur Dauer	In Arbeit	